Stony Brook University

Measurement of the Elliptic and Triangular Flow in Ultra-Relativistic Cu+Cu and Au+Au Collisions at $\sqrt{s_{NN}}$ = 200 GeV

A Dissertation presented

by

Damian Lee Reynolds

to

The Graduate School

in Partial Fulfillment of the

Requirements

for the Degree of

Doctor of Philosophy

in

Chemistry

(Chemical Physics)

Stony Brook University

December 2015

Stony Brook University

The Graduate School

Damian Lee Reynolds

We, the dissertation committe for the above candidate for the

Doctor of Philosophy degree, hereby recommend

acceptance of this dissertation

Roy Lacey - Dissertation Advisor
Professor, Department of Chemistry

Jiangyong Jia - Co-Advisor
Associate Professor, Department of Chemistry

Trevor Sears - Chairperson of Defense
Professor, Department of Chemistry

Joanna Kiryluk
Assistant Professor, Department of Physics

This dissertation is accepted by the Graduate School

Charles Taber
Dean of the Graduate School

Abstract of the Dissertation

Measurement of the Elliptic and Triangular Flow in Ultra-Relativistic Cu+Cu and Au+Au Collisions at $\sqrt{s_{NN}} = 200$ GeV

by

Damian Lee Reynolds

Doctor of Philosophy

in

Chemistry

(Chemical Physics)

Stony Brook University

2015

Differential measurements of the elliptic and triangular flow Fourier coefficients are reported for charged hadrons as a function of transverse momentum and collision centrality for Cu+Cu and Au+Au collisions at $\sqrt{s_{NN}} = 200$ GeV measured with the PHENIX detector located at the Relativistic Heavy-Ion Collider at Brookhaven National Laboratory. The flow coefficients, an important probe in the investigation of the quark-gluon plasma, are measured using a long-ranged two-particle correlation method where the azimuthal angles of particles about midrapidity in the central arm detectors are correlated with hits in detectors located at forward rapidity, ensuring a large pseudorapidity gap to prevent biasing due to non-flow effects. Results are also investigated in terms of the number of participants, and the geometry of the initial state nucleon configuration of the collision system such as eccentricty and transverse system size estimated using the Glauber model. Removing some of the geometric effects between the two collision systems, these results provide additional constraints for theoretical models.

Dedication Page

To Cobalt and Xenon for being so fuzzy and not excessively needy.

Contents

List of Figures **vi**

List of Tables **vii**

List of Abbreviations **viii**

List of Notation **ix**

1 Introduction **1**
1.1 The Standard Model and Quantum Chromodynamics 1
1.1.1 The Standard Model 1
1.1.2 QCD Phase Diagram and the Quark-Gluon Plasma . . 3
1.2 Ultra-Relativistic Heavy-Ion Collisions 6
1.3 Coordinate System 8
1.4 Collective Flow 9

2 RHIC and the PHENIX Detector **13**
2.1 The Relativisitic Heavy-Ion Collider 13
2.2 The PHENIX Detector 14
2.2.1 PHENIX Central Magnet 16
2.3 Forward Detectors 17
2.3.1 Beam-Beam Counter 17
2.3.2 Reaction Plane Detector 19
2.3.3 Zero Degree Calorimeter 19
2.4 Central Arm Detectors 20
2.4.1 Drift Chamber 20
2.4.2 Pad Chamber 22
2.4.3 Ring Imaging Cherenkov Detector 26

2.4.4 Electromagnetic Calorimeter 28
2.5 Data Acquisition 30

3 Calibration **33**
3.1 Track Reconstruction 33
3.2 The Glauber Model 35
3.2.1 Glauber Model Introduction 35
3.2.2 Impact Parameter, b 37
3.2.3 Number of Participants, N_{part} 38
3.2.4 Number of Binary Collisions, N_{coll} 40
3.2.5 Ellipticity ϵ_2 43
3.2.6 Triangularity, ϵ_3 45
3.3 Centrality Calibration 47

4 Analysis **50**
4.1 Event Plane Analysis 50
4.1.1 Event Plane Overview 50
4.1.2 Event Plane Determination 50
4.1.3 Event Plane Resolution 53
4.1.4 Event Plane Final Step 55
4.2 Long-Ranged, Two-Particle Method 56
4.2.1 Two-Particle Correlation Method 56
4.2.2 Run and Event Selection 58
4.2.3 EPD-EPD Correlations 61
4.2.4 EPD-CNT Correlations 68
4.2.5 Systematic Errors 71

5 Results **78**
5.1 Comparison to Established Results 78
5.2 Elliptic and Triangular Flow Results for Cu+Cu $\sqrt{s_{_{NN}}}$ = 200 GeV 81
5.3 Comparisons between Au+Au and Cu+Cu 82
5.3.1 Centrality Dependence 82
5.3.2 N_{part} Dependence 83
5.3.3 Eccentricity Dependence 84
5.3.4 $N_{\mathrm{Part}}^{1/3}$ Dependence 85

6 Conclusion **87**

7 Appendix **89**

List of Figures

1.1 A feynman diagram of Møller scattering where two electrons repel each other via exchange of a photon. 2
1.2 The meson and baryon octets proposed by Gell-Mann. 3
1.3 The QCD phase diagram. 4
1.4 The R_{AA} of π^0 and direct photons in Au+Au $\sqrt{s_{_{NN}}}$ = 200 GeV collisions. 5
1.5 A more realistic heavy-ion collision showing Lorentz-contracted nuclei colliding. 6
1.6 An over-simplified depiction of a heavy-ion collision. 7
1.7 The shape of the collision region while varying the impact parameter. 7
1.8 The single particle η distribution of particles emitted from an event measured in the PHOBOS detector. 9
1.9 The elliptic flow of various identified charged hadrons at PHENIX and STAR from minimum-bias Au+Au collisions. 10
1.10 The elliptic flow of various identifed charged hadrons scaled by their number of constituent quarks n_q at PHENIX and STAR from minimum-bias Au+Au collisions. 11
1.11 The PHOBOS event plane measurement of v_2 as a function of pseudorapidity. 11
1.12 An extreme example of a geometrically triangular distribution of participating nucleons in heavy-ion collision in the Glauber model. 12

2.1 An arial view of the RHIC Accelerator Complex. 13
2.2 PHENIX detector configurations 15
2.3 The PHENIX magnet in the ++ field configuration. 16
2.4 Photos of the BBC detector. 18

2.5 A rendering of one of the RXN detector showing how it is mounted on the central magnet. 19
2.6 Top-down view of the ZDC in relation to the beam intersection point. 20
2.7 A schematic of the anode and cathode wires of the drift chambers. 21
2.8 The drift of ionized electors through the DC from the passing of a charged particle. 22
2.9 The pad chambers 23
2.10 The pad layout 24
2.11 The pad chamber exploded view. 25
2.12 A top-down schematic of a single pad chamber showing the data acquisition components 25
2.13 An electron passing through the RICH showing the Cherenkov photon ring. 26
2.14 An arm of the RICH detector. 27
2.15 A more detailed schematic of charged particle passage through the RICH. 28
2.16 The EMCal PbGl. 29
2.17 A single tower of the PbSc. 30
2.18 A top-level view of the PHENIX data acquisition system. . . . 31
2.19 Schematic of the Event Builder. 32

3.1 A charged particle being tracked to the collision vertex. 33
3.2 Hits in the DC and the 2D combinatorial Hough transform plot. 34
3.3 Sample Glauber model outputs for Cu+Cu and Au+Au. . . . 35
3.4 The charge distribution used for Cu nuclei. 36
3.5 The impact parameter distributions in 10% centrality bins. . . 38
3.6 The $N_{\rm part}$ distributions for Au+Au $\sqrt{s_{_{NN}}}$ = 39 GeV in 10% centrality bins. 39
3.7 (a) $N_{\rm part}$ as a function of centtrality and (b) its systematic error contributors. 40
3.8 The $N_{\rm part}$-$N_{\rm coll}$ correlation for Cu+Cu $\sqrt{s_{_{NN}}}$ = 200 GeV . . . 41
3.9 The $N_{\rm coll}$ distributions for Au+Au $\sqrt{s_{_{NN}}}$ = 39 GeV in 10% centrality bins. 42
3.10 (a) $N_{\rm coll}$ as a function of centtrality and (b) its systematic error contributors. 42

3.11 The transverse projection of the participant plane may not be colinear with the reaction plane depending on the fluctuations in the participant distribution. 43
3.12 The eccentricity ϵ_2 distributions for 0-60% in centrality in 10% centrality bins. 44
3.13 (a) The eccentricity ϵ_2 as a function of centtrality and (b) its systematic error contributors. 45
3.14 The eccentricity ϵ_3 distributions for 0-60% in centrality in 10% centrality bins. 46
3.15 (a) The eccentricity ϵ_3 as a function of centtrality and (b) its systematic error contributors. 46
3.16 Estimated BBC charge deposition from the Glauber N_{part} distribution of Cu+Cu $\sqrt{s_{_{NN}}}$ = 200 GeV 48
3.17 Dividing the Glauber/NBD result by the data shows losses due to the BBCLL1 Trigger. 49
3.18 The BBC Distribution for Run10 Au+Au $\sqrt{s_{_{NN}}}$ = 39 GeV chopped into 10% centrality bins. 49

4.1 A simple figure showing hits in both sides of the BBC largely in the v_2 event plane. From [18]. 51
4.2 The event plane distribution at different stages in the calibration process. 52
4.3 Correlation between the North and South RXN v_2 event plane measurements. 53
4.4 Centrality flatness of runs for the Cu+Cu $\sqrt{s_{_{NN}}}$ = 200 GeV . Anything above the red line at $\chi^2/(NDF\sqrt{N_{\text{events}}}) = 0.03$ is not used. 58
4.5 Three different z-vertex distributions for three different runs. . 59
4.6 A two-dimensional plot showing the means and the standard deviations of the z-vertex distributions for all of the runs in the Cu+Cu $\sqrt{s_{_{NN}}}$ = 200 GeV dataset. 60
4.7 The RICH n_0 for electrons. 61
4.8 Schematics of the (a) BBC (b) RXN channels. 62
4.9 Foreground and background distributions of the EPD-EPD correlations. 64
4.10 The BBC-BBC Correlation function for Cu+Cu $\sqrt{s_{_{NN}}}$ = 200 GeV 65

4.11 The BBC-BBC Correlation function for Au+Au $\sqrt{s_{_{NN}}}$ = 200 GeV 65
4.12 The BBC-BBC Correlation function for Au+Au $\sqrt{s_{_{NN}}}$ = 200 GeV 66
4.13 A RXN^{N}- RXN^{S}_{OUT} correlation function. 66
4.14 The BBC-BBC Correlation function after smearing by a Gaussian function. 67
4.15 The BBC-CNT Correlation function for Cu+Cu $\sqrt{s_{_{NN}}}$ = 200 GeV for $1.5 \leq p_T < 2.0$ GeV/c. 68
4.16 The BBC-CNT Correlation function for Cu+Cu $\sqrt{s_{_{NN}}}$ = 200 GeV for the 30-40% centrality bin. 69
4.17 The BBC-CNT Correlation function for Au+Au $\sqrt{s_{_{NN}}}$ = 200 GeV for $1.5 \leq p_T < 2.0$ GeV/c. 69
4.18 The BBC-CNT Correlation function for Au+Au $\sqrt{s_{_{NN}}}$ = 200 GeV for the 30-40% centrailty bin. 70
4.19 A systematic error check of the trigger efficiency on the Cu+Cu v_2. 71
4.20 A systematic error check of the trigger efficiency on the Cu+Cu v_3. 72
4.21 A systematic error check of the z-vertex binning on the Cu+Cu v_2. 73
4.22 A systematic error check of the z-vertex binning on the Cu+Cu v_3. 74
4.23 A systematic error check of the σ_{PC3} cut on the Cu+Cu v_2. . . 75
4.24 A systematic error check of the σ_{PC3} cut on the Cu+Cu v_3. . . 75
4.25 A systematic error check of the East and West central arms on the Cu+Cu v_2. 76
4.26 A systematic error check of the East and West central arms on the Cu+Cu v_3. 77

5.1 Au+Au v_n event plane vs. two-particle correlation results. . . 78
5.2 Cu+Cu v_n event plane vs. two-particle correlation results. . . 79
5.3 Cu+Cu v_n results compared to STAR. 80
5.4 Final Cu+Cu $\sqrt{s_{_{NN}}}$ = 200 GeV v_n results as a function of p_T in 10% centrality bins. 81
5.5 Final Cu+Cu $\sqrt{s_{_{NN}}}$ = 200 GeV v_n results as a function of p_T in 5% centrality bins. 82
5.6 Elliptic and triangular flow as a function of centrality. 83

5.7 Elliptic and triangular flow as a function of $N_{\rm part}$. 84
5.8 Elliptic and triangular flow scaled by ϵ_n as a function of $N_{\rm part}$. 85
5.9 The elliptic flow scaled by ϵ_2 and $N_{\rm Part}^{1/3}$ as a function of $N_{\rm part}$ for Cu+Cu and Au+Au collisions at $\sqrt{s_{_{NN}}}$ = 62.4 and 200 GeV. 85
5.10 Elliptic and triangular flow scaled by ϵ_n and $N_{\rm Part}^{1/3}$ as a function of $N_{\rm part}$. 86

6.1 A comparison of different models across v_2 and v_3 for Au+Au $\sqrt{s_{_{NN}}}$ = 200 GeV 88

List of Tables

1.1 Quarks (Spin 1/2) from ref. [1] 2

7.1 Cu+Cu $\sqrt{s_{NN}}$ = 200 GeV v_3 data points for centralities 0-30% in 10% centrality bins. 89
7.2 Cu+Cu $\sqrt{s_{NN}}$ = 200 GeV v_3 data points for centralities 30-60% in 10% centrality bins. 90
7.3 Cu+Cu $\sqrt{s_{NN}}$ = 200 GeV v_3 data points for centralities 0-40% in 10% centrality bins. 91
7.4 Cu+Cu $\sqrt{s_{NN}}$ = 200 GeV v_3 data points for centralities 0-20% in 5% centrality bins. 92
7.5 Cu+Cu $\sqrt{s_{NN}}$ = 200 GeV v_3 data points for centralities 20-40% in 5% centrality bins. 93
7.6 Cu+Cu $\sqrt{s_{NN}}$ = 200 GeV v_3 data points for centralities 40-60% in 5% centrality bins. 94
7.7 Cu+Cu $\sqrt{s_{NN}}$ = 200 GeV v_3 data points for centralities 0-20% in 5% centrality bins. 95
7.8 Cu+Cu $\sqrt{s_{NN}}$ = 200 GeV v_3 data points for centralities 0-20% in 5% centrality bins. 96
7.9 The Glauber values used in sections **??** and **??**. 97

List of Abbreviations

2PC	Two-Particle Correlation
BBC	Beam-Beam Counter
DC	Drift Chamber
EP	Event Plane
GeV	Giga-Electronvolt ($10^9 eV$)
NBD	Negative Binomial Distribution
PC	Pad Chamber
PHENIX	Pioneering High-Energy Nuclear Interaction eXperiment
QCD	Quantum Chromodynamics
QGP	Quark-Gluon Plasma
RXN	Reaction Plane Detector

List of Notation

c	Speed of light in a vacuum
ϵ_n	n^{th} order eccentricity
Ψ_n	n^{th} order event plane
p_T	Transverse Momentum
$R_A A$	Yield of an A+A divided by a scaled $p+p$ yield
$\sqrt{s_{_{NN}}}$	Center of mass energy per nucleon in a collision
N_{coll}	Number of binary collisions
N_{part}	Number of participating nucleons
v_n	n^{th} order Fourier coefficient
ϕ	The azimuthal angle in the spherical coordinate system
θ	The polar angle in the spherical coordinate system
η	Pseudarapidity $-\ln[\tan(\theta/2)]$

Chapter 1
Introduction

1.1 The Standard Model and Quantum Chromodynamics

1.1.1 The Standard Model

Our everyday experiences are largely dominated by a small number of particles: protons, neutrons, electrons, and photons. During the later half of the 20^{th} century a slew of new particles were discovered and catalogued. Presently the standard model has several large groups: leptons, mediators, and hadrons.

Leptons carrying a spin of 1/2 have negatively charged electrons, muons, tauons, as well as their associated uncharged, massless neutrinos. All of these also have their anti-particles which have the oppositely signed charge. The positron, e^+ is easily the most famous being discovered quite early due to the β^+ radioactive decay where a proton becomes a neutron, emitting a positron and an electron neutrino.

$$p \rightarrow n + e^+ + \nu_e \tag{1.1}$$

The weak interaction in eq. 1.1 depicts the conservation of the Lepton number since p has a lepton number of $L_e = 0$, the positron $L_e = -1$ and the neutrino $L_e = 1$. The total lepton number is zero before and after the interaction.

Interactions between particles in the standard model are carried out by mediators also known as gauge bosons. These bosons have a spin of 1 and are comprised of photons (γ) (electromagnetic), gluons (strong), $W^{\pm}$, and Z^0 (weak). A good example from quantum electrodynamics (QED) is shown in figure 1.1 where, during Møller scattering, two electrons repel each other through the exchange of a photon. The electromagnetic force has been coupled with the weak force into a more unified electroweak theory by Glashow, Weinberg, and Salam earning them the 1979 Nobel Prize in Physics [1].

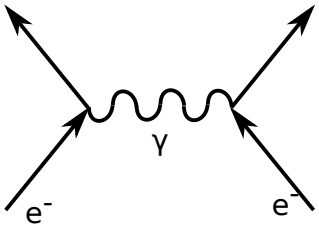

Figure 1.1: A feynman diagram of Møller scattering where two electrons repel each other via exchange of a photon.

Finally there are many particles known as hadrons which are made of very basic building blocks called quarks that are held together by the strong nuclear force. Table 1.1 shows the 6 different "flavors" of quarks, their charges, and masses. Like with leptons, there is also a conservation of quark number and by extension baryon number. Each of these quarks has its own antiquark. Hadrons cannot be made from arbitrary combinations of quarks, thankfully, or there would be significantly more particles to add to the already crowded lists of known hadrons.

Flavor	Charge /e	Mass (speculative) /MeV c^{-2}		
		Bare	Effective	
			In baryons	In mesons
d	-1/3	7.5	} 363	} 310
u	+2/3	4.2		
s	-1/3	150	538	483
c	+2/3	1100	4700	
b	-1/3	4200	1500	
t	+2/3	> 23000		

Table 1.1: Quarks (Spin 1/2) from ref. [1]

While quantum electrodynamics has a concept of electric charge which takes two values: positive and negative, quarks and gluons quantum chromodynamics (QCD) has color charge that have 6 values: red, green, blue, antired, antigreen, antiblue. The only valid, and thus, observed bound states are colorless (e.g. rgb, $\bar{r}\bar{g}\bar{b}$, $r\bar{r}$). With these in mind, diagrams like figure 1.2 were created in order to help organize these particles much like the periodic table was created for chemical elements.

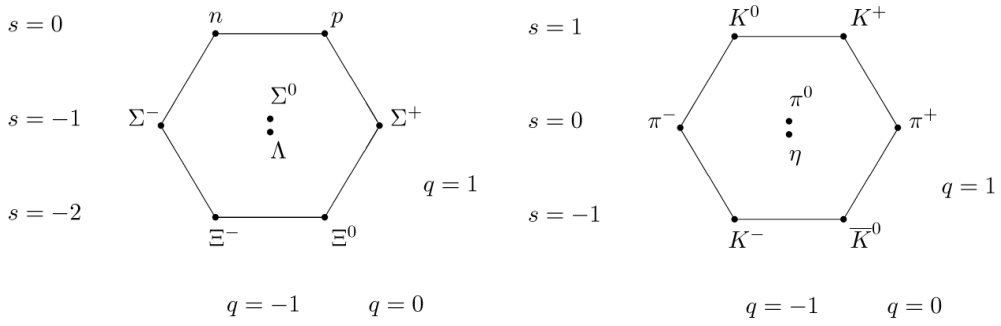

(a) The baryon octet.

(b) The meson octet.

Figure 1.2: The meson and baryon octets proposed by Gell-Mann. The axes here are strangeness and electric charge from ref. [2]

Normal hadrons are further divided into two groups: baryons and mesons. Baryons have three quarks where each quark has a different color charge (rgb). The most well-known examples being the proton (uud) and the neutron (udd). The fractional charges of the individual quarks gives these baryons the proper integer electric charges. Mesons, on the otherhand, are a pair of quark and an antiquark with a color and anticolor charge. The lightest, and therefore the most easily produced mesons are the pions and kaons.

Another notable feature of the quark model is a phenomenon known as asymptotic freedom. If one were to pull two oppositely charged particles away from one another, the energy required to do so would decrease as a function of separation. With quarks, the energy requirement continues to increase until the point where a quark and antiquark pair can be produced like in equation 1.2.

$$\begin{aligned} udd &\rightarrow udu + \bar{u}d \\ n &\rightarrow p + \pi^- \end{aligned} \tag{1.2}$$

1.1.2 QCD Phase Diagram and the Quark-Gluon Plasma

The quantum chromodynamic (QCD) phase diagram, much like a phase diagram in chemistry, is used to to characterize the state of matter that is

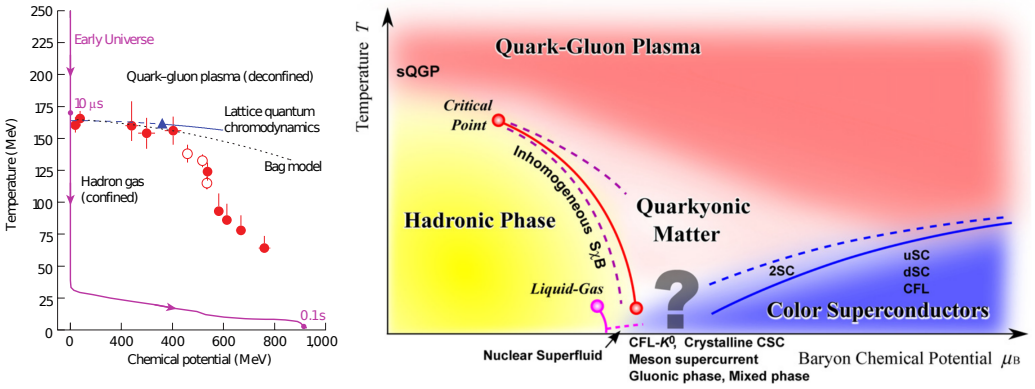

(a) (b)

Figure 1.3: (a) A detailed view of the areas of the QCD phase diagram probed by heavy-ion collisions from ref. [3] (b) A QCD phase diagram showing much higher hadronic densities from [4].

expected to be found given certain conditions. The baryon chemical potential is analogous to the more familiar chemical potential which is the energy associated with changing the amount of a substance. In this case it refers to the number of baryons as opposed to anti-baryons that can be found in the volume. Matter-antimatter pairs are produced during a high energy collision as per Einstein's famous equation

$$E = mc^2, \tag{1.3}$$

where E is energy, m is mass, and c is the speed of light. By increasing the collision energy, the number of particles (multipicity) increases, the ratio of baryons to antibaryons will tend toward zero while also increasing in temperature as shown in figure 1.3a.

In the vicinity normal nuclear density nuclei the hadronic gas phase behaving as the name suggests, a gas phase consisting of hadrons. Proceeding higher in temperature there is a first-order phase transition into the quark-gluon plasma phase [5]. At these high temperatures, asymptotic freedom suggests that the interaction strength between quarks diminishes leaving us a phase where the quarks and gluons are no longer confined within the hadron but are deconfined, allowed to move about. Despite the diminished interaction strength, there are still strong force interactions. Comparisons of yields

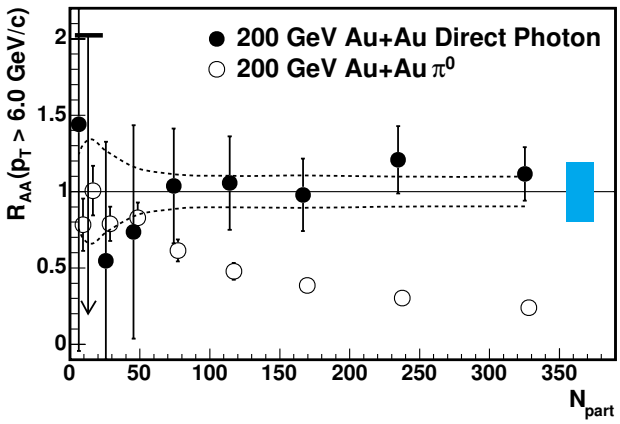

Figure 1.4: The R_{AA} of π^0 and direct photons in Au+Au $\sqrt{s_{_{NN}}} = 200$ GeV collisions.

in $p+p$ and $A+A$ collisions can show how the presence of this medium effects particle production. Take for example the comparisons of π^0 and direct photons yields measured in $p+p$ and Au+Au collisions in figure 1.4 from ref. [6]. The quantity R_{AA} is a measure of the yield of something in $A+A$ collisions divided by the yield in $p+p$ collisions scaled by the average number of binary collisions N_{coll} (sec. 3.2.4). Photons, being purely QED particles, do not feel the strong force and unaffected by the presence of the quark-gluon plasma which is why it remains more or less unaffected by the system size indicated by the number of participating nucleons, N_{part} (sec. 3.2.3). In contrast, π^0 production seems to be suppressed with the increase of the size of the QGP. High-energy jets show signs of path-length dependent energy loss [7].

This transition line extends to low baryon chemical potential ending at a not yet discovered critical point. There have been and will continue to be efforts at the Relativistic Heavy Ion Collider to find it, taking data at lower energies during the Beam Energy Scan. To the left of that critical point the hadronic gas goes through a crossover transition as it becomes a quark-gluon plasma at around 175 MeV $\sim$ 2 trillion Kelvin. This region is being studied by theorists using methods like lattice QCD.

While particle accelerators are able to probe the left-hand side of figure 1.3, matter on the right-hand side of the diagram is extremely high density matter like that found in exotic stars.

1.2 Ultra-Relativistic Heavy-Ion Collisions

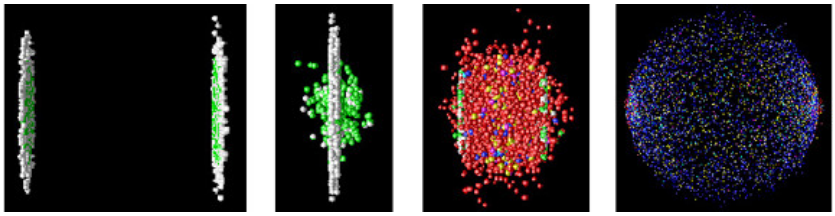

Figure 1.5: A more realistic heavy-ion collision showing Lorentz-contracted nuclei colliding. The ions largely pass through one another but participating nucleons will be create the QGP. Expansion and hadronic freeze-out occur later.

Figure 1.5 shows the collision of two ions. When two ions are brought to relativistic speeds, they undergo Lorentz contraction, flattening into pancakes. Some of the nucleons will interact as the pancakes fly throught each other. The result is a hot dense fireball that is the quark-gluon plasma. The QGP with some internal pressure greater than the vacuum, will expand and hadronize.

While it would be great if we could steer a beam accurately enough to have a single ion hit another, that is not the case in real life. Ther approach utilized here is better visualized as two shotguns, loaded with birdshot, shooting at each other. There is some very small (but non-zero) chance that that when two ion bunches cross that a collision will occur. With each RHIC ring loaded with upwards of a hundred bunches traveling at nearly the speed of light, collisions occur at rates well above our data-taking capacity. The low collision probability is also beneficial in that the chance of two collisions per bunch crossing is extremely low which makes the particle tracking much simpler.

Figure 1.6 shows a simple, first-order approximation of a heavy-ion collision. Two counter propagating nuclei approach each other with some impact parameter b in the transverse plane. With the vectors that make up the beam direction and b, a reaction plane can be defined. The magnitude of b is the single biggest contributor to the geometry of the QGP. With a head-on collision ($b = 0$), the interaction region looks more like the left of figure 1.7, azumuthally isotropic. As the impact parameter increases, the shape becomes smaller and more elliptical.

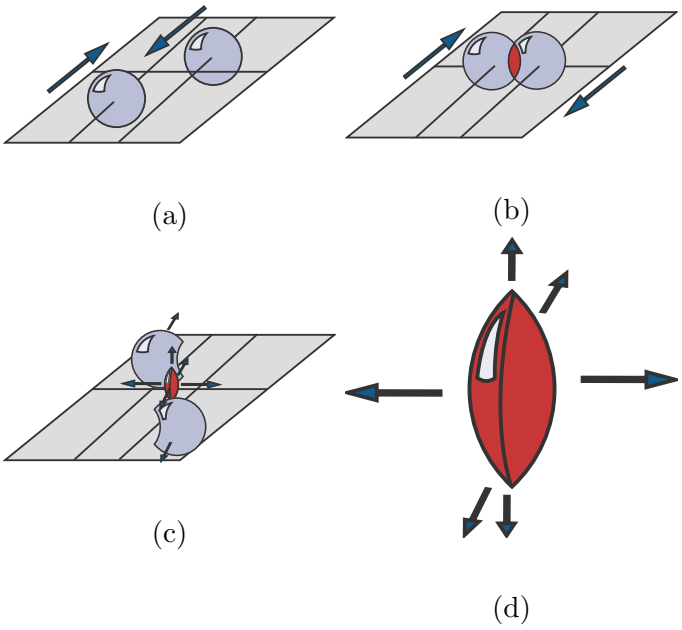

Figure 1.6: An over-simplified depiction of a heavy-ion collision. (a) Two ions approach each other and a reaction plane is defined by the beam direction and their impact parameter. (b) The nuclei hit each other creating a hot, dense matter. (c) Spectators continue flying straight. (d) Pressure gradients within the QGP start to cause expansion preferentially along the reaction plane.

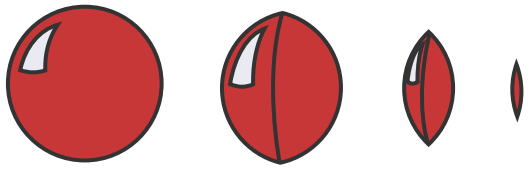

Figure 1.7: The shape of the collision region while varying the impact parameter.

1.3 Coordinate System

The PHENIX detector, shown in figure 2.2, naturally lends itself to being described by the cylindrical coordinate system with its origin at the nominal crossing point of the detector and its longitudinal axis located along the beamline. The azimuthal angle, ϕ, swings about this axis. We typically only use the z-coordinate when discussing where collisions had occured, the z-vertex, or when discussing position of hits in the various detector subsystems.

What is more relevant are values that describe the path of particles (tracks) originating from the collision. In the lab frame the angle in the z direction, θ, is rarely used rather we opt for the Lorentz invariant version, pseudorapidity,

$$\eta \equiv -\ln\left[\tan\left(\frac{\theta}{2}\right)\right] \tag{1.4}$$

The common lexicon is to refer to particles emitted nearly perpendicularly to the beamline ($\eta = 0$) as being at midrapidity and higher values as being at forward rapidity and negative values as being backward rapidity. Rapidity, y, which requires both knowledge of a particle's energy and momentum, is different than pseudorapidity but the term is often used interchangeably.

The PHOBOS detector has a large pseudorapidity coverage ($|\eta| < 5.4$) making it ideal for longitudinal studies. With it they have made detailed measurements of the single particle distribution as a function of pseudorapidity [8, 9] shown in figure 1.8. From this, it is clear that more particles are measured at midrapidity than in forward or backwards rapidity so more focus is put there in terms of detector placement.

Many analyses like this one will focus primarily on observables in the transverse plane, that is, the plane perpendicular to the beam direction. A term used throughout is transverse momentum p_T which can be calculated in cartesian coordinates as:

$$p_T = \sqrt{p_x^2 + p_y^2} \tag{1.5}$$

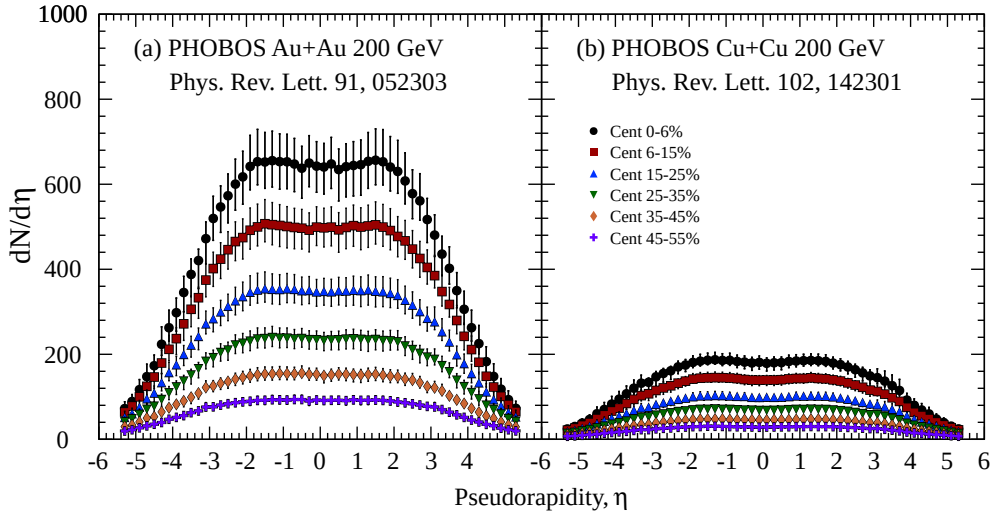

Figure 1.8: The single particle η distribution of particles emitted from an event measured in the PHOBOS detector.

1.4 Collective Flow

The motion of particles in the quark-gluon plasma are often studied separately in order to gain an understanding of the global picture. As far as flow is concerned there are some broad categories: longitudinal expansion, radial transverse flow, and anisotropic transverse flow [10]. Looking at transverse flow, the single particle angular distribution can be written as a Fourier series,

$$\frac{dN}{d\phi} = \frac{1}{2\pi}\left[1 + \sum_{n=1}^{\infty} 2v_n \cos n(\phi - \Psi_n)\right] \tag{1.6}$$

The Fourier component v_n of the anisotropic transverse flow are categorized as follows: directed (v_1), elliptic (v_2), triangular (v_3) flow, and higher order harmonics of v_n. At lower values of p_T, where hydrodynamics is believed to dominate, v_n tends to scale linearly with the eccentricity of the participating nucleons (ϵ_n). This suggests that it is the geometric anisotropy of the collision region which leads to the observed anisotropy in particle emission.

Elliptic flow has always been popular because of the presumed symmetry of the collision. A large elliptic flow means that there are more particles being emitted in the event plane than perpedicular to the plane.

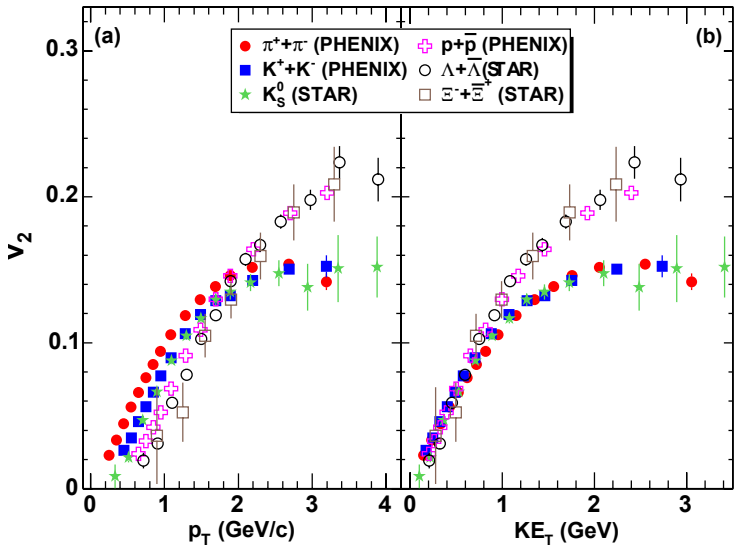

Figure 1.9: The elliptic flow of various identified charged hadrons at PHENIX and STAR from minimum-bias Au+Au collisions. (a) v_2 as a function of p_T. (b) v_2 as a function of KE_T.

Looking at the elliptic flow for identified charged particles like in figure 1.9 found in ref. [11], it is apparent that the observed flow splits into two distinct groups. Mesons ($\pi^{\pm}, K^{\pm}, K^0_s$) containing a quark-antiquark pair tend to have less flow than their baryon ($p + \bar{p}, \Lambda + \bar{\Lambda}, \Xi^{\pm}$) counterparts which are a triplet of quarks. When these flow values are scaled by the number of consituent quarks they all come into alignment despite the fact that these various species have vastly different masses. This is a good indication that flow develops while the thermalized fireball consists of quarks and gluons rather than later after hadronization has occured.

Though PHENIX analyses are primarily focused on the particles emited about midrapidity, PHOBOS had measured the elliptic flow as a function of η [12] shown in figure 1.11. For both Cu+Cu and Au+Au at different energies, v_2 diminishes as $|\eta|$ increases. This pseudorapdity dependece is is relevant to this analysis because multiple detector subsystems that lie in different pseudorapidity ranges will be used.

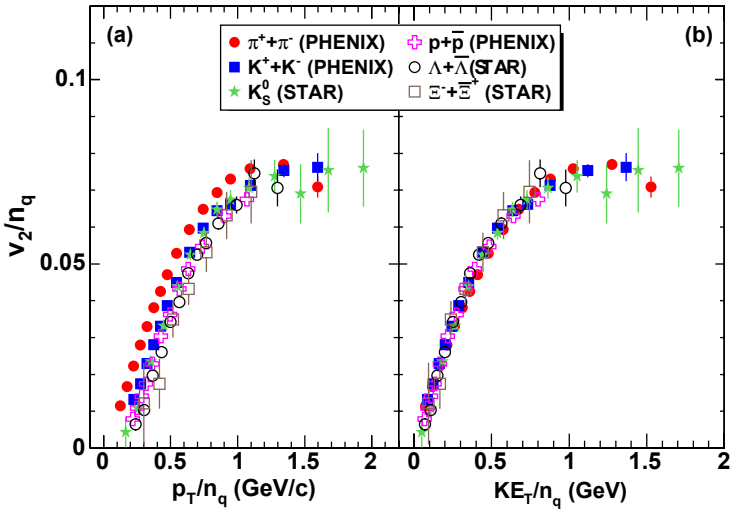

Figure 1.10: The elliptic flow of various identifed charged hadrons scaled by their number of constituent quarks n_q at PHENIX and STAR from minimum-bias Au+Au collisions. (a) v_2/n_q as a function of p_T/n_q. (b) v_2/n_q as a function of KE_T/n_q.

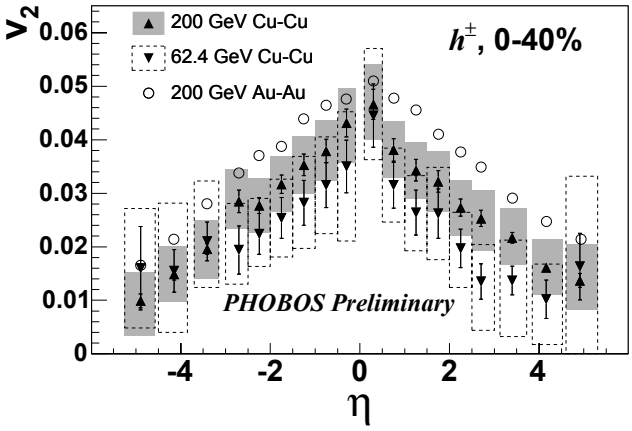

Figure 1.11: The PHOBOS event plane measurement of v_2 as a function of pseudorapidity.

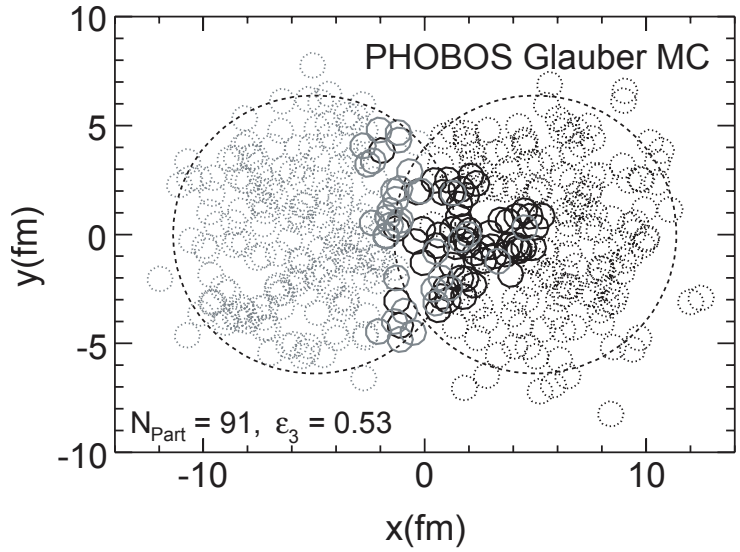

Figure 1.12: An extreme example of a geometrically triangular distribution of participating nucleons in heavy-ion collision in the Glauber model.

The odd numbered harmonics ($v_3, v_5, ...$) had been ignored for quite sometime because with the prevailing picture of a collision having a smooth profile, like that shown in figure 1.6, odd terms were assumed to be zero [13]. While figure 1.12 is a rather extreme case of having triangular geometry and would certainly lead to an augmentation of v_3, It is clear from even a simple model such as the Glauber model that one can have significant fluctuations from this idealized shape. it has also been suggested that they also be related to the near-side ridge seen in two-particle correlation studies. The observed v_3 signal may be smaller because it has been suggested that higher order terms are affected more by viscocity [14].

In essence, by studying these higher order terms, we are studying the lumpiness of the initial state configuration of the system. Studying Cu+Cu is an interesting collision system because it has fewer nucleons than Au+Au. Any fluctuations present would likely have a more pronounced effect.

Chapter 2
RHIC and the PHENIX Detector

2.1 The Relativisitic Heavy-Ion Collider

The Relativistic Heavy-Ion Collider is located at Brookhaven National Laboratory on Long Island, New York.

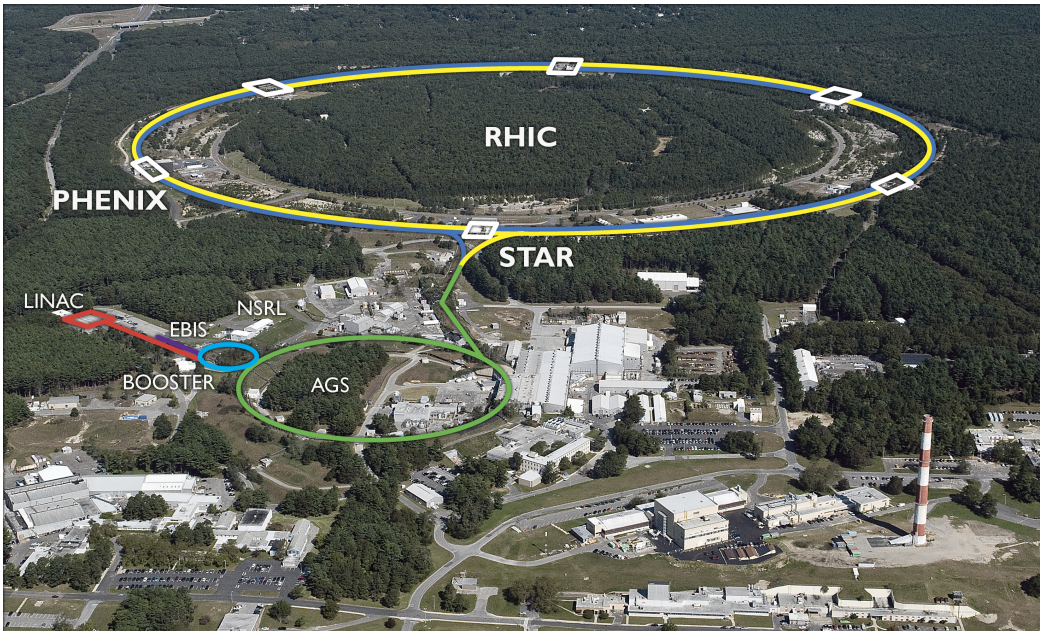

Figure 2.1: An arial view of the RHIC Accelerator Complex.

The ions used in this experiment start in the Linear Accelerator or Linac as seen in figure 2.1. Protons are accelerated up to 200 MeV before being injected into the Alternating Gradient Syncotron (AGS) Booster ring. The AGS booster as one might expect is used to boost the energy of protons or other heavy ions before injecting them into the larger AGS. In its yesteryears, the AGS has been home to many discoveries in nuclear physics producing several Nobel prizes including the discovery of the J/ψ meson in 1974[15], CP

Violation in 1980, and the discovery or the muon-neutrino in 1988. Later in the 2000s, the AGS became yet another booster accelerating ions into the much larger Relativistic Heavy-Ion Collider (RHIC) measuring 2.4 miles (3.9 km) in circumference. The heavy ion beam is split into two, counterpropagating rings, shown as yellow and blue in figure 2.1, , accelerated to the desired collision energy then colliding at the six crossing points. This accelerator has been used to collide many species of nuclei: p, d, $^{27}Al^{13+}$, $^{197}Au^{79+}$, $^{63}Cu^{29+}$, and $^{238}U^{92+}$ at various center of mass energies ($\sqrt{s_{NN}}$) ranging between 9.2 GeV/nucleon and 200 GeV/nucleon for heavy ions and going as high as 500 GeV for $p+p$ collisions. One advantage that RHIC has over the Large Hadron Collider at CERN (Conseil Européen pour la Recherche Nuclèaire) is the ability to produce spin-polarized proton beams[16] which is important for people studying spin physics. While only PHENIX and STAR are shown in the figure, there were two other collaborations, PHOBOS and BRAHMS who had finished their missions and are no longer present.

It is without question that the most important detector at RHIC is the PHENIX detector.

2.2 The PHENIX Detector

Many different subsystems comprise the full PHENIX detector.

The upper portion of figure 2.2 shows one of the most distinct characteristics of the PHENIX detector which is its Central Arm Detectors on the East and the West. Each arm covers the pseudorapidity region of $|\eta| < 0.35$ and subtends 90° in azimuth. There is a 67.5° opening on the top and 112.5° opening on the bottom.

It should come as no surprise that there is a large central magnet present in order to obtain the momentum of a charged particle.

In the forward and backward rapidity regions there are the muon arms whose names betray their purpose. There are also some critically important detectors like the beam-beam counters and reaction plane detectors.

Initially some of the main objectives of the PHENIX Experiment were to observe the leptonic decays of the $\omega, \rho, \phi, J/\Psi, \Psi', \Upsilon$ particles[17] which is the reason detectors sensitive to different decays are located where they are.

I will go into more detail about the detector systems that have been used in this analysis.

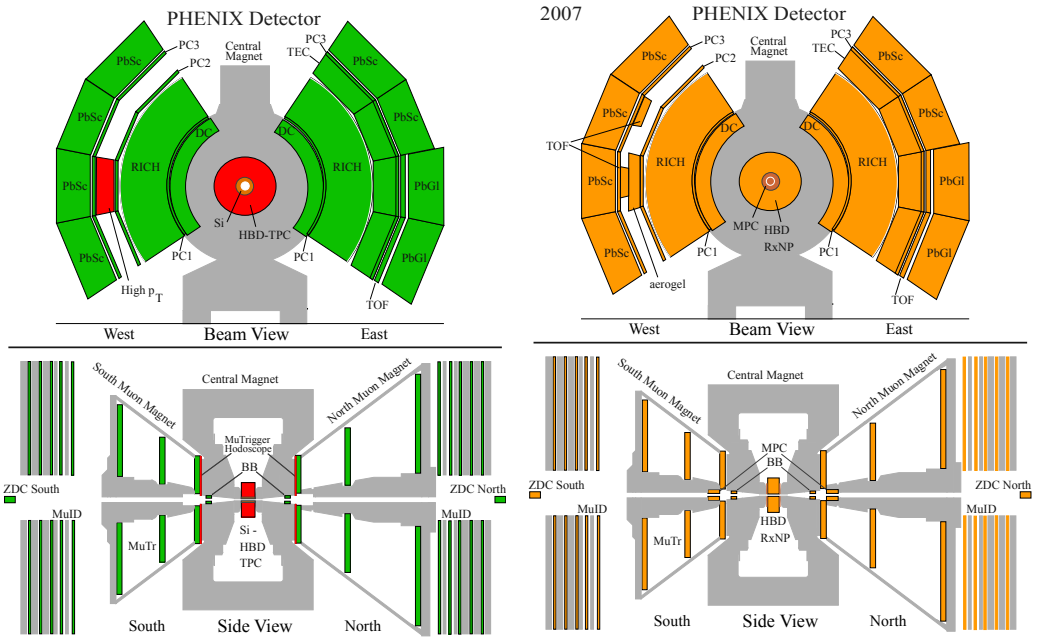

(a) 2005

(b) 2007

Figure 2.2: PHENIX detector configurations

2.2.1 PHENIX Central Magnet

In the presence of uniform magnetic field, a charged particle will travel in a circle, accelerating orthogonally from field and its velocity. This circle has a a gyroradius described by:

$$r = mv_{\perp}/B|q| \tag{2.1}$$

By measuring this gyroradius, it is easy this particle's momentum.

The magnetic field in the PHENIX detector is not so simple though as seen in figure 2.3 where the field is in its ++ configuration. It was designed such that at the collision vertex there would be zero field and also the field would be mostly contained within a 2 m radius.

A little bit more about the complexity of the field will be covered when discussing track reconstruction in section 3.1.

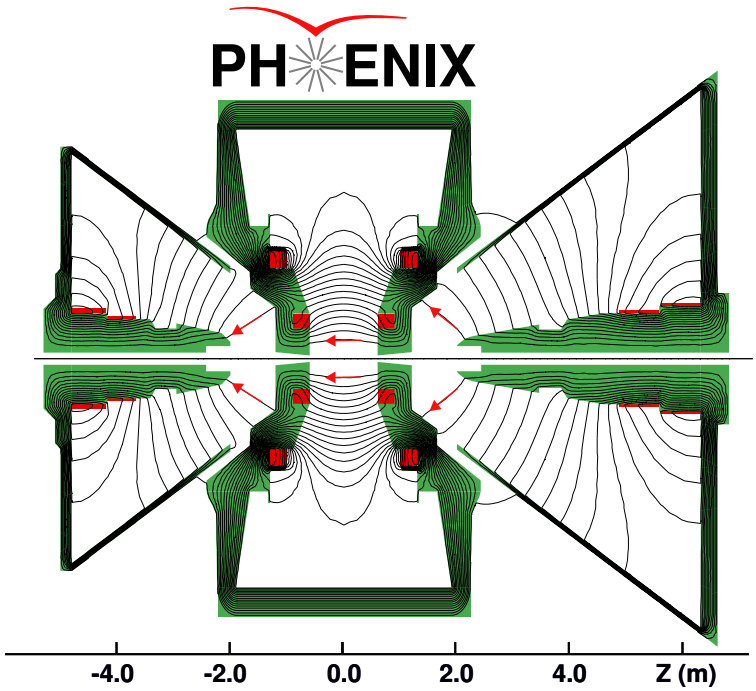

Figure 2.3: The PHENIX magnet in the ++ field configuration.

2.3 Forward Detectors

Unlike the central arms, there are a set of detectors that lie in the forward and backwards rapidity regions which have the full 2π azimuthal coverage. These detectors are primarily used to characterize global properties of an event rather than its constituent particles. Examples of what is designated as a global property might be the z-position of event vertex or the direction and magnitude of the reaction plane.

2.3.1 Beam-Beam Counter

The Beam-Beam Counter (BBC), located approximately 144 cm North and South from the nominal collision vertex, and sitting in the pseudorapdity range of $3.1 < |\eta| < 4.0$ as shown in fig. 2.2b, is responsible for some of the most critical event-level measurements:[18].

1. Minimum bias trigger (discussed in sec. 2.5)
2. Centrality determination (discussed in sec. 3.3)
3. Reaction plane determination (discussed in sec. 4.1)
4. Collision vertex determination
5. Time-zero determination

A brief overview of some of these items will be covered in this section with a more detailed discussion elsewhere.

Each BBC detector comprises 64 hexagonal quartz Cherenkov radiator crystals measuring 2.54 cm across and 3 cm long with a mesh dynode photomultiplier tube affixed to the back. Figure 2.4 shows a single crystal and its PMT as well as the fully assembled detector ready to be mounted either North or South of the collision vertex.

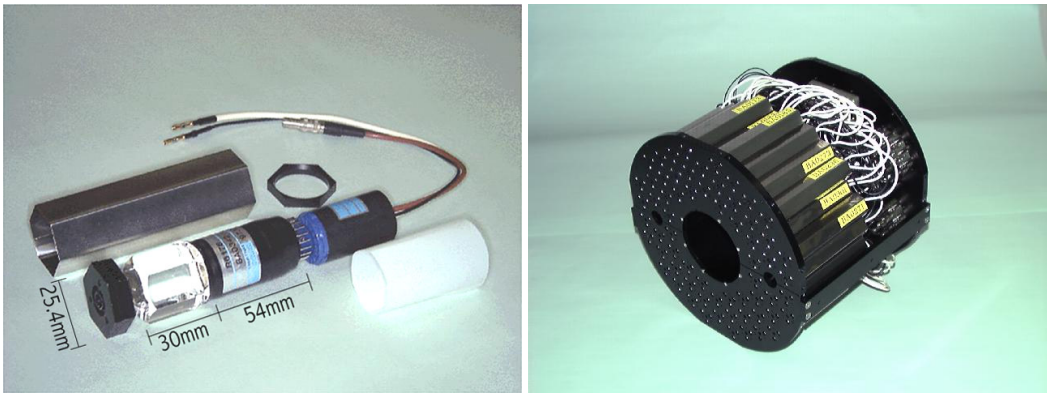

(a) One channel of the BBC where the quartz crystal and photomultiplier tube are visible.

(b) A full assembly of the BBC with all 64 channels arranged in a honeycomb-like fashion.

Figure 2.4: Photos of the BBC detector.

The first three items in the list are all measured by studying the charge deposited in the BBC which should be directly proportional to the number of charged particles passing through it.

With a timing resolution of 20 ps additional event information can be obtained by comparing the times at which a hit was registered in the North or South BBCs.

The z-vertex measured from the nominal collision vertex can be determined simply by looking at the timing difference between hits in the BBCs and assuming that the particles are travelling at the speed of light c.

$$z\text{-vertex} = \frac{T_S - T_N}{2} \times c \tag{2.2}$$

Where T_N and T_S denote the timestamps for a hit registered in the North and South BBCs respectively. The BBCs are able to determine the z-vertex with a resolution of 0.6 cm.

Another important measurement for particle identification is the precise timing for the start of the collision T_0. This quantity can be found with another simple equation 2.3

$$T_0 = \frac{T_S + T_N - 2L/c}{2} \tag{2.3}$$

In this equation, L represents the distance of the BBCs relative to the nominal collision vertex (144.35 cm).

2.3.2 Reaction Plane Detector

[19] Added in 2007, the two Reaction Plane Detectors (RXN) are situated at $|z| = 38$–40 cm of the nominal crossing point. Each detector is divided into 12 segments with an azimuthal coverage of $\Delta\phi = \pi/6$. These are then further subdivided into two rings with an outer part $\mathrm{RXN_{OUT}}$, $1.0 < |\eta| < 1.5$ and an inner part $\mathrm{RXN_{IN}}$, $1.5 < |\eta| < 2.8$.

This is yet another Cherenkov radiation detector with a utilizing a thick lead plate followed by a scintillating plastic and fiber optics to carry the Cherenkov photons to PMTs to be read out.

The hallmark of this detector is that it provides much better event plane resolution as described in section 4.1.3

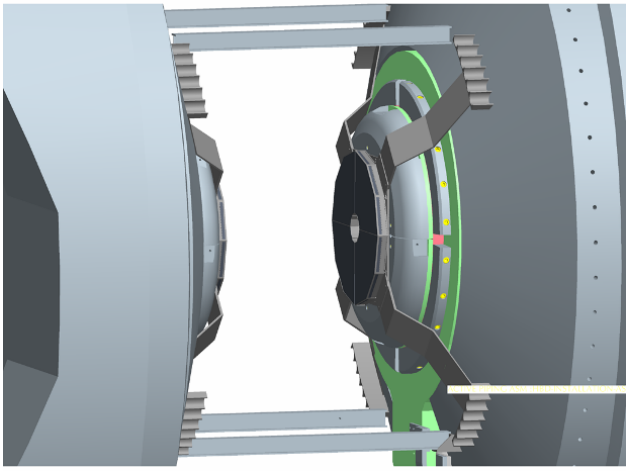

Figure 2.5: A rendering of one of the RXN detector showing how it is mounted on the central magnet.

2.3.3 Zero Degree Calorimeter

The Zero Degree Calorimeter (ZDC), used in all of the RHIC experiments, consist of two detectors sitting far North and South of the interaction region along the beam axis as shown in figure 2.6 They measure the energy deposited by spectator neutrons that do not participate in collision. As such, their signal is stronger as collisions become more peripheral. This behavior lends itself to being a useful trigger described later in section 2.5.

Because the spatial distribution of neutrons is very small, the construction of the detector did not emphasize segmentation in the transverse plane. [20] Only the total energy deposition was sought.

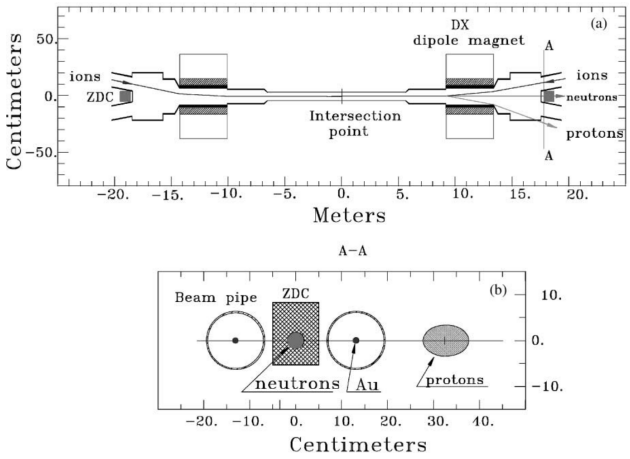

Figure 2.6: Top-down view of the ZDC in relation to the beam intersection point.

2.4 Central Arm Detectors

The central arms of the PHENIX detector span a pseudorapidity range of $|\eta| \leq 0.35$. The focus of these detectors are for hadron, electron, and photon identification.[21]

2.4.1 Drift Chamber

The cylindrically shaped drift chambers (DC), located between 2.0 m and 2.4 m from the beam, lie within the residual magnetic field (≤ 0.6 kG) produced by the central magnet.[22] They are primarily responsible for the momentum reconstruction and the tracking of charged particles in the PHENIX detector.

There are 6 wire planes that can be seen in figure 2.7 , X1, U1, V1, X2, U2, and V2. The X planes lie parallel to the beam axis whereas the U and V cross each other at some small stereoangle.

Each wire provides a track position measurement, with better than 120 μm spatial resolution and ~ 1 mrad angular resolution.

Figure 2.8 shows a simulation of the passage of a charged particle through the drift chamber. The gas (a 1:1 mixture of argon and ethane) is ionized as the particle passes through, the electrons drift away from the cathode wires on the sides towards the anode wires in the middle. There are low potential back wires that are arranged such that electrons from the right-hand side of

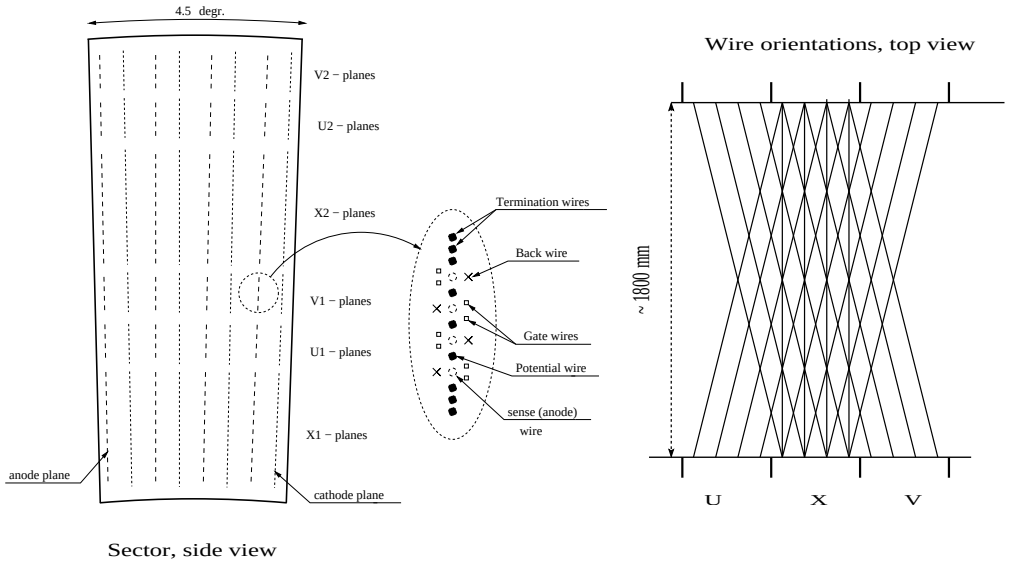

Figure 2.7: A schematic of the anode and cathode wires of the drift chambers.

of the wire plane will only hit the even numbered sense wires and the left-hand side will only hit the odd numbered ones. The gate wires allow only a 3 mm length of of drift lines in which helps decrease the pulse width.

Because the UV wires are at a small (6°) stereoangle relative to the X wires the DC is able to make some measurement of the z-coordinate, however the PC1 placed directly behind it provides a more accurate measurement.

Track reconstruction will be covered in section 3.1

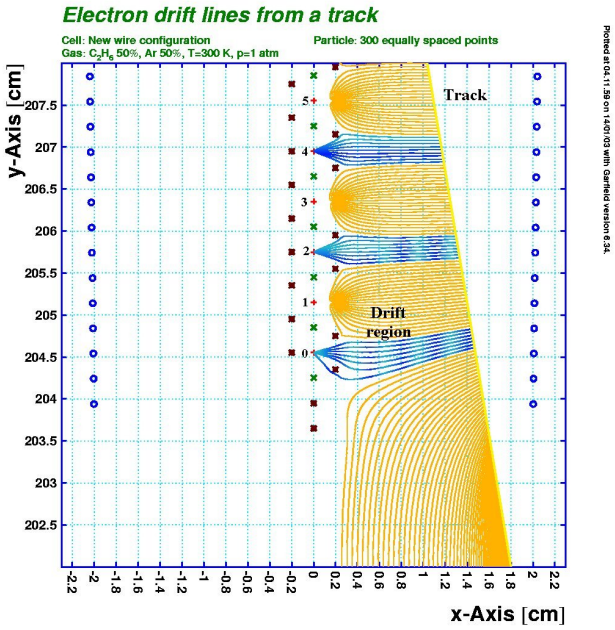

Figure 2.8: The drift of ionized electors through the DC from the passing of a charged particle.

2.4.2 Pad Chamber

The pad chambers (PC) consist of layers of multi-wire proportional chambers with a pad readout. Unlike the DC, the PC lies outside of the magnetic field so charged particles travel in straight line paths. The space points measured by the various layers of the PC are integral to reconstructing the charged particle tracks back through the DC and ultimately back to the collision vertex.[23] The West arm has three pad chambers PC1, PC2, and PC3 located at a radial distance of 2.4 m, 4.2 m, and 4.9 m respectively. The East arm has only PC1 and PC3 (due to budgetary constraints) located at the same distance.

The pad chambers, being rather thin (e.g. PC1 is 58 mm thick)[17] and placed in close proximity to other detectors, makes for conivenient entry and exit points. For instance, while the drift chambers are able to provide a z-coordinate using its UV stereo wires, however the PC1 is able to provide a more accurate measurement. Additionally the PC1 serves as an entry point to the RICH. A hit registered by the ElectroMagnetic Calorimeter

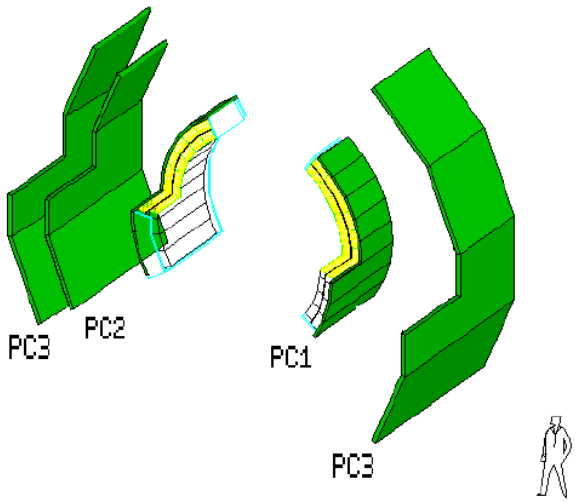

Figure 2.9: The pad chambers

(EMCal) can be caused by charged hadrons, electrons, and photons. The PC3 located directly before the EMCal, however, will only register hits by charged particles. If we are looking to study photons, we can employ a charge veto cut requiring the EMCal hit to be outside of a certain range from a projected track through the PC3. Conversely, if we want to reject photon when studying EMCal hits, we can require that these tracks also hit the PC3.

The layout of the pad readout is quite unique in that rather than opt for expensive, highly granular detector channels, the pad chamber is made up of layers of larger, staggered plates as seen in figure 2.10. Shown in this figure is a flattened projection of a a pad with 3x3 cells with an area of 8.4x8.4 mm^2 where the cells are shifted in the plane of the chamber as well as the layers being shifted relative to the anode wire. The PC1 has a position resolution of about ± 1.7 mm. The PC2 and PC3 were designed to cover the same solid angle and are therefore larger than the PC1.

Charged particles travel through a potential of $\sim$2000 V, ionizing a gas mixture of 50% argon, 50% ethane which effectively amplifies the charge that hits pads. Though each pad spans a large area, the staggered arrangment gives each cell a unique triplet coordinate. This configuration requires one

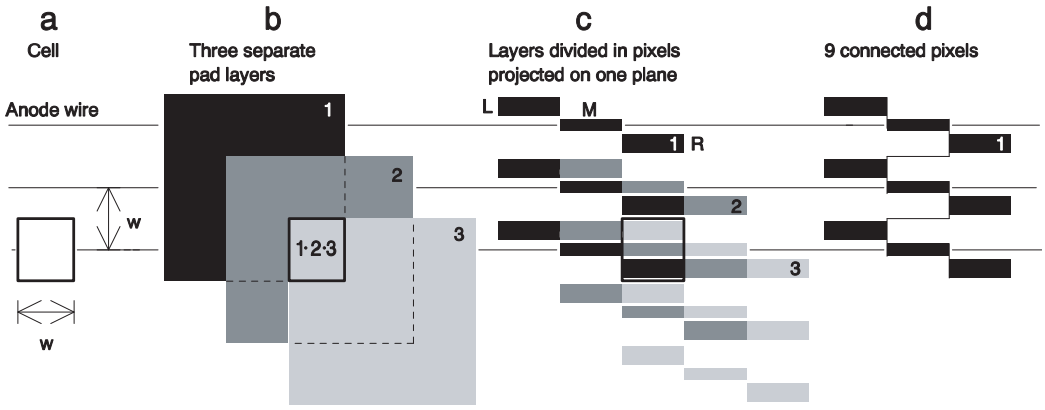

Figure 2.10: The pad layout

third the number of electronic channels as opposed to a configuration that has individual cells. The occupancy trade-off has not been a problem with the multiplicities seen in even the most central collisions at RHIC energies.

Signals from the pads are sent to read-out cards (ROCs) as shown in figure 2.12. These were kept simple so that there would not be much material in the fiducial volume of the detector. They are essentially voltage discriminators that require a coincident signal from three adjacent pads as described earlier. This requirement makes them somewhat resistant to random electronic noise. Additionally they simplicity lends itself to being efficient and reliable. Data from the 9x5 ROCs are then sent to Front-End Modules (FEMs) to be handled by the larger PHENIX data acquisition system discussed in section 2.5

Since the PC1 is so integral to track reconstruction, much care had been taken to minimize the radiation thickness in order to prevent reduce the number of electron pairs from high energy photons. Including the electronics, the PC1 had a radation thickness of 1.2% and a very small dead area in the PHENIX central arm acceptance, $< 0.7\%$ whereas the PC2 and PC3 had radiation lengths of $\sim 2.4\%$ and dead areas of 7.6%

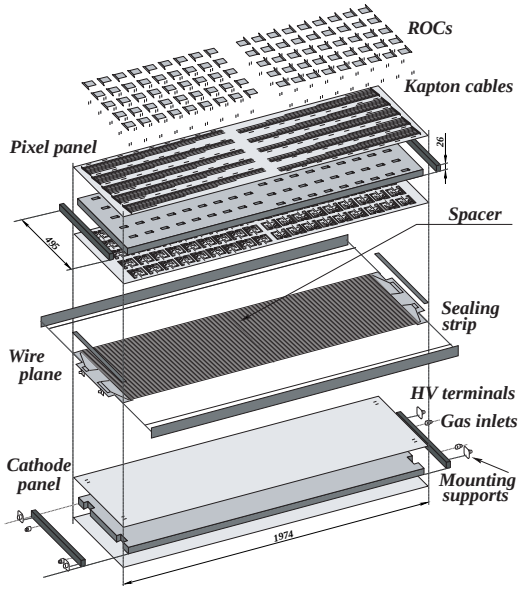

Figure 2.11: The pad chamber exploded view.

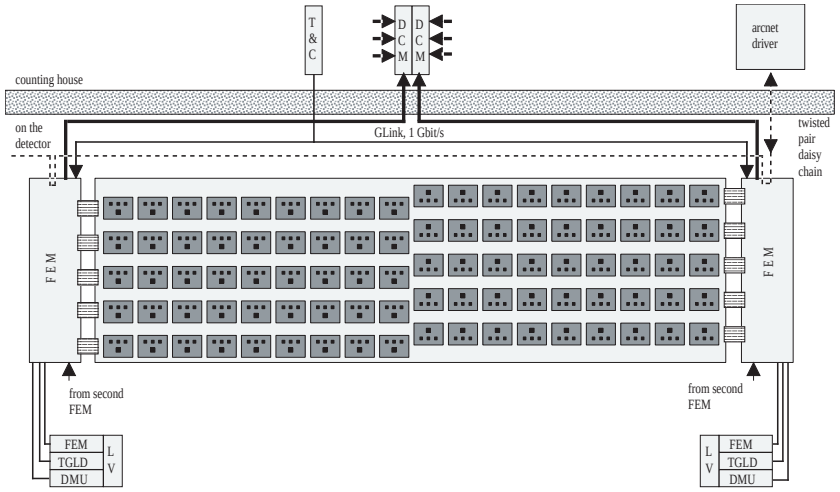

Figure 2.12: A top-down schematic of a single pad chamber showing the data acquisition components

2.4.3 Ring Imaging Cherenkov Detector

Ring Imaging Cherenkov detector (RICH), which sits in the region of 2.575 and 4.1 m from the beam about midrapidity, was designed for electron identification.[24]

The schematic view shown in figure 2.15 shows the passage of a charged particle originating at the collision vertex, passing into RICH, filled with CO_2 or ethane producing a cone of Cherenkov photons, which are then reflected off of curved mirrors, and finally collected by a highly angularly separated array of PMTs. The original charged particle proceeds through the PHENIX detector.

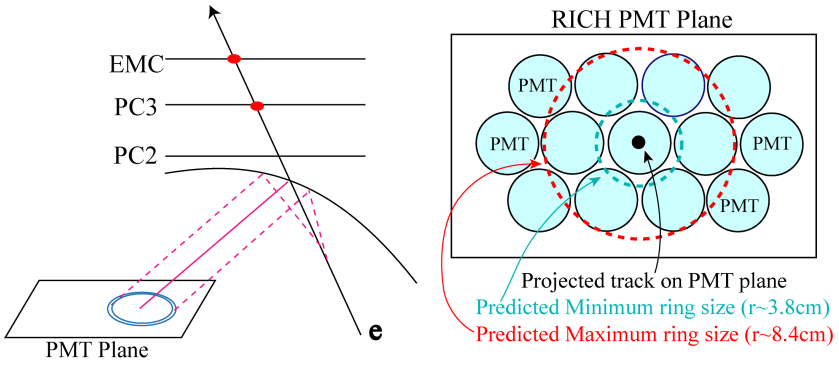

(a) An electron passing through the RICH. Cherenkov photons are reflected into a ring on the PMT plane.

(b) The expected minimum and maximum ring size of Cherenkov photons left on the PMT plane by passing electrons.

Figure 2.13: An electron passing through the RICH showing the Cherenkov photon ring.

In CO_2,a pion ($\pi^{\pm}$) needs to exceed a momentum threshold of 4.9 GeV/c in order to produce Cherenkov photons. In ethane, the threshold is lower

This gives us the ability to discriminate between tracks that come from electrons or charged hadrons at momenta lower than the threshold.

The radiation length in the fiduciary volume was kept quite small totalling about 2.1% when filled with ethane.

At the time of installation, the charged pion rejection was in excess of the 10^4 requirement and its electron efficiency was $> 99\%$ for isolated tracks

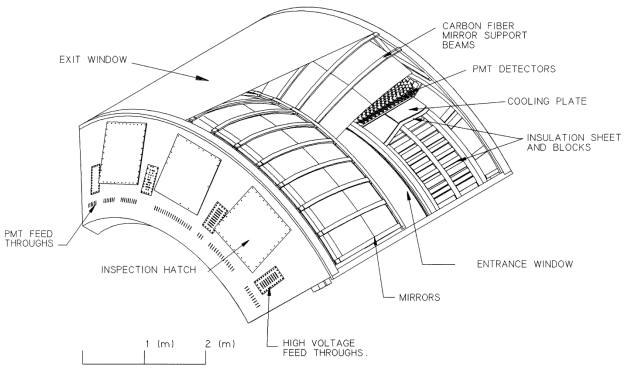

Figure 2.14: An arm of the RICH detector.

but drops somewhat due to background conversions of high energy photons during very central Au+Au collisions.

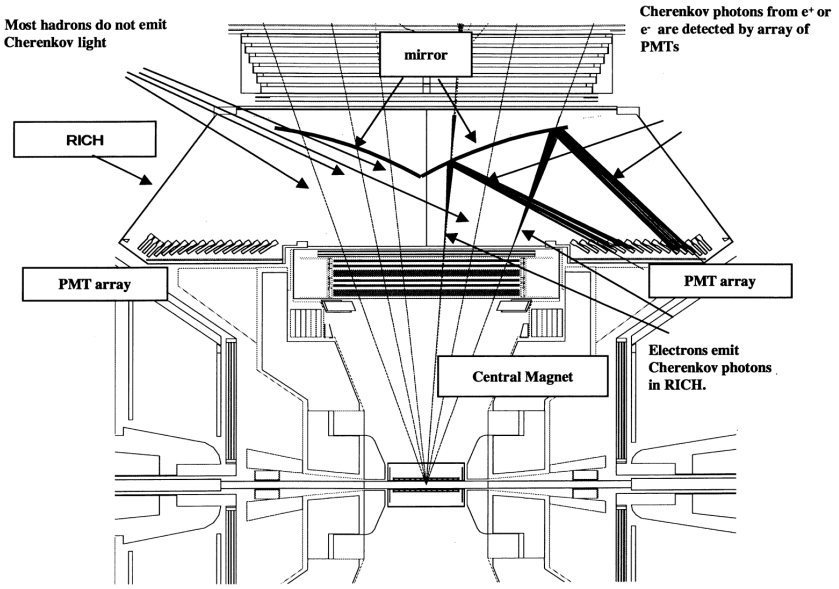

Figure 2.15: A more detailed schematic of charged particle passage through the RICH.

2.4.4 Electromagnetic Calorimeter

As implied by its name, the ElectroMagnetic Calorimeter (EMCal) is principally responsible for measuring the energy of electromagnetic particles like photons, eletrons, and to some degree, charged hadrons. The EMCal has two different detector technologies labeled as PbSc and PbGl in figure 2.2. On the East and West arms there is the Lead Scintilator (PbSc) whereas the Lead Glass (PbGl) is only on the East arm.

The PbGl has a simple design; It's essentially a $4 \times 4 \times 40$ cm^3 block of lead glass and a photomultiplier. (See figure 2.16a) The PbGl has an index of refraction of $n = 1.647$ so particles travelling faster than 60% of the speed of light will emit Cherenkov radiation. [25]

The PbSc consists of 66 layers of 1.5 mm of Pb absorber and 4 mm of a scintillating material. Particles collide with the absorber then create a shower which travels though the scintillator, generating light. This light then travels through fiber optics to photomultipliers on the back.

Despite both the PbSc and PbGl being Cherenkov light detectors, the PbSc has better timing resolution and the PbGl has beter energy resolution. [26]

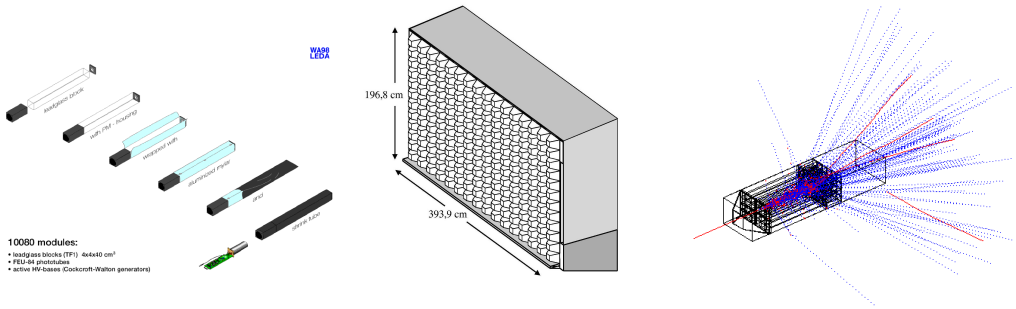

(a) One tower of the PbGl. (b) One of two sectors of the PbGl. (c) A shower in the PbGl.

Figure 2.16: The EMCal PbGl.

Charged hadrons, unlike electrons and photons, do not deposit all of their energy in the EMCal but their hits can be detected. Provided the start time of the collision from the BBC, the time of flight can be obtained and therefore the velocity of the particle.

As mentioned in sec. 2.4.2, the PC3, situated directly in front of the EMCal, can be used to cut on EMCal hits that lie very close to PC3 hits to ensure that the track came from a charged hadron. Alternatively it can be used to cut out EMCal hits that lie close to the PC3 hits to ensure that the track is that of a photon.

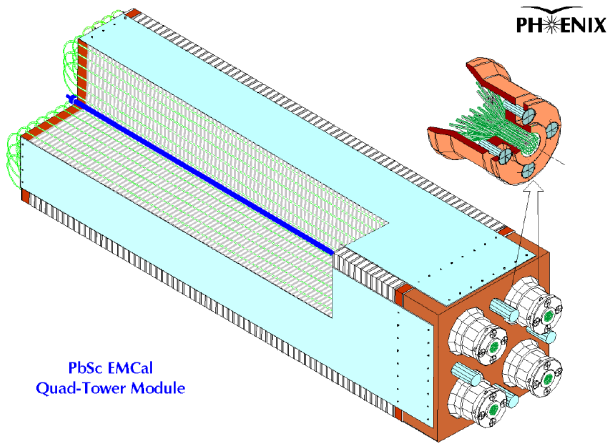

Figure 2.17: A single tower of the PbSc.

2.5 Data Acquisition

The PHENIX data acquisition system (DAQ) is responsible for receiving, rudimentary processing, and storage of the raw data from the detectors.

Some of the data acquisition was described eariler when discussing the pad chambers. A subsystem's FEMs send event data through a gigabit throughput connection known as the GLink to the Data Collection Modules (DCMs). With the Event Builder (EvB) running, data is sent to one or more Single Event Buffers (SEBs).[27] The Event Builder Controller (EBC) receives event notifications and assigns them and flushes the system. The Assembly Trigger Processors (ATPs) assembles the events and processes any Level-2 triggers then ships them off for temporary storage in the Advanced Multithreaded Logger (AMLs) of the Buffer Box (BB). Here event data is temporarily resides in an accessible filesystem and can analyzed by primarily subsystem experts and people really anxious to get new data. As filesystems fill, they are shipped over to the more permanent data facility, HPSS. This is shown in figure 2.19.

While different subsystems (granules) are able to be independently accessed, they all need instructions on when to take data.[28] Desired granules are added to another container known as a partition which is given the same triggers like the BBCLL1.

Multiple triggers are loaded for different physics goals. The Level-1 triggers act on a very basic level like hits registered in both the MuID North and

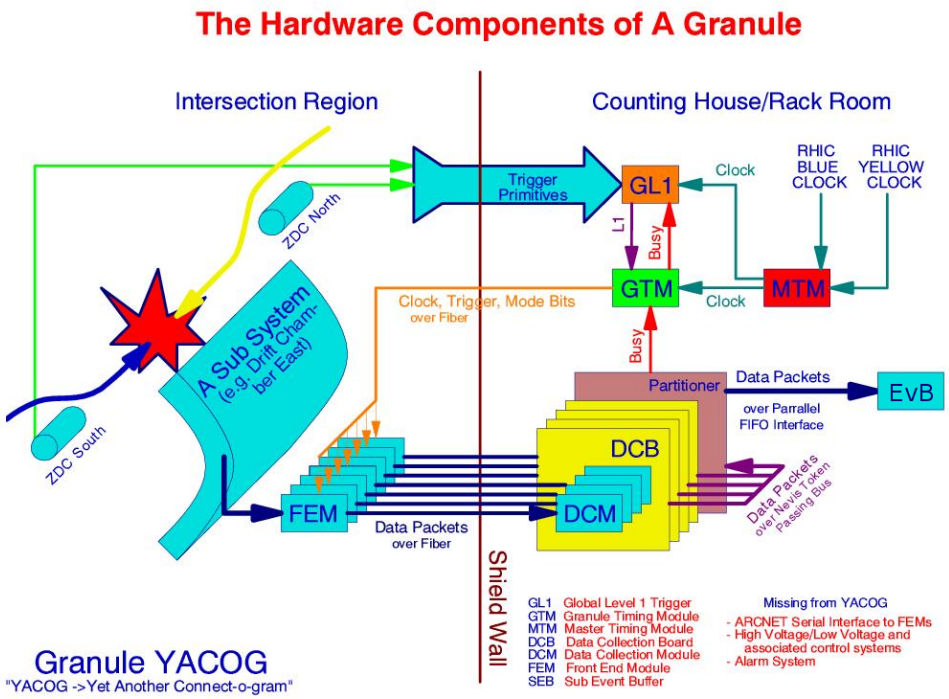

Figure 2.18: A top-level view of the PHENIX data acquisition system.

BBC North, or hits in the TOF or EMCal. Events not satisfying any of the trigger conditions are not deemed to have any physics that is of interest to the collaboration and is therefore discarded. Passing this stage, The event builder system can take a closer look and apply Level-2 triggers which can further reduce the data volume. While it is a shame to throw away collision data, it is a necessity due to computational limitations; the daq system can only handle so many events per second. Even events which satisfy these conditions may be randomly discarded with some probability dependent on the relative importance of PHENIX's physics goals for the year.

For my analyses, I utilize one of the most permissive triggers, the minimum bias (MB) dataset which we define as an event where at least one hit is recorded in both the North and South BBC, the BBC Local Level 1 or BBCLL1 trigger, with the event occuring within 30 cm of the nominal vertex position. Triggers are discussed in section 2.5

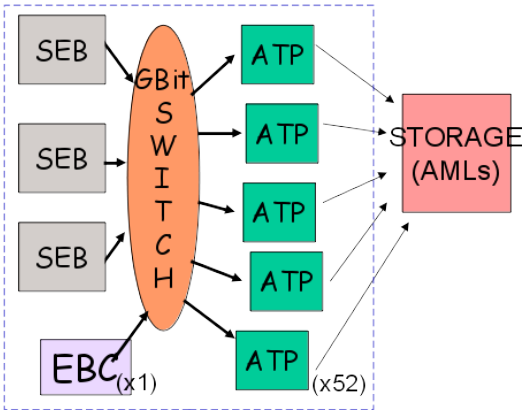

Figure 2.19: Schematic of the Event Builder.

Synchronization of the PHENIX DAQ and RHIC is critically important to the proper reassembly of events. One of the RHIC clocks is synchronized with the PHENIX Master Timing Module (MTM) which in turn synchronizes with the Global Timing Module (GTM) and the Globel Level 1 Trigger (GL1) Finally the GTM is tasked with synchronizing with all of the FEMs.

The GL1 manages all of the Local Level-1 Triggers reported by the FEMs then ultimately decides whether or not the FEMs should send their data to the DCMs.

Chapter 3
Calibration

3.1 Track Reconstruction

Particle tracks are reconstructed primarily based off of space points measured in the DC and PC1. And working on the assumption that they will be traveling in nearly straight-line paths by the time they get there. Figure 3.1

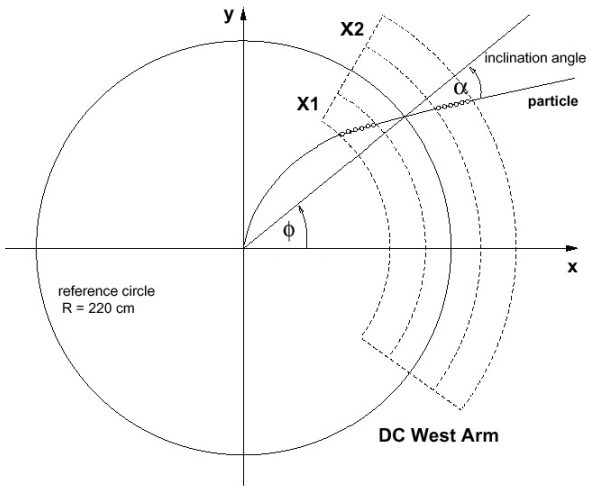

Figure 3.1: A charged particle being tracked to the collision vertex.

shows a track in the bending plane that is transverse to the beam. A line defined by any two points will intersect with the reference circle which lies radially in the middle of the DC, 220 cm from the beam. Two important values are determined at this intersection point, the azimuthal angle, ϕ with respect to the lab frame, and the inclination angle α, between the track line and ϕ. These values are not unlike the definition of a line where α is the slope and ϕ is the intercept [29]. Because charged particles are deflected in a magnetic field proportionally to their momentum, in this plane, α is inversely proportional to a particle's transverse momentum, p_T. That is to say, a higher momentum particle will be deflected less in a magnetic field,

Tracks are reconstructed back to the collision vertex using a pattern recog-

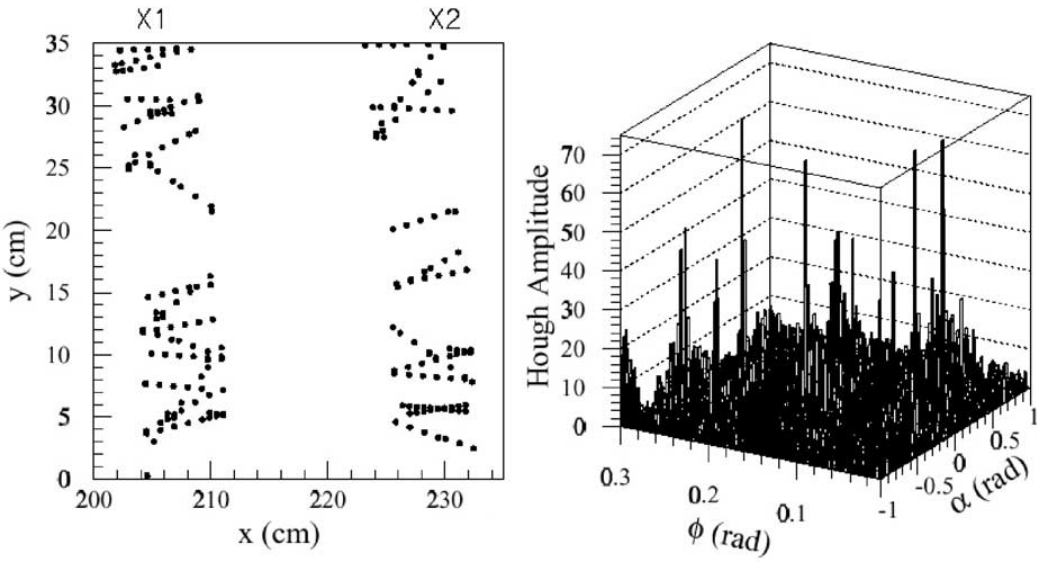

Figure 3.2: Left: Hits measured in the X1 and X2 wire planes in the DC. Right: Combinatorial Hough transform plot.

nition algorithm known as combinatorial Hough transformation [21]. With this method, α and ϕ values are recorded between combinations of hits in the DC. To save some processing power and time, pairs that would give unreasonable values are not included.

The right panel of figure 3.2 shows some combinations of hits in the drift chamber for a sample event. Most pair comibnations, not being from the same track, will produce a noise floor, while combinations from the same track, sharing the same α and ϕ values, will produce local maxima.

The track matching algorithm first looks for tracks that traverse both the X1 and X2 wire planes of the drift chamber before checking tracks that only cross one of those. If there is an unambiguous track leading to a PC1 hit, then the θ value in the non-bending plane is found by using its z-coordinate as well as the event's z-vertex. If, however, there is some ambiguity in PC1 or the PC1 hit is missing, the drift chamber's UV stereo-wires are used and the appropriate DC quality bits are set (sec. 4.2.2). The PC1 has better z-coordinate resolution so it is prefered when available. This method is robust in that it produces false tracks at a rate of less than 1% even with high-multiplicity, central Au+Au events.

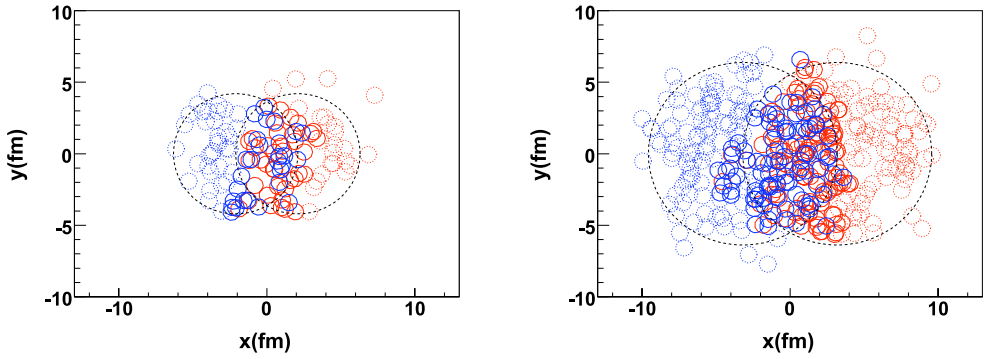

(a) Cu+Cu (b) Au+Au

Figure 3.3: Sample Glauber model outputs for Cu+Cu and Au+Au from ref. [30]. The colors red and blue indicate nucleons originating in one nucleus or the other. Circles with solid lines show wounded nucleons that have participated in the collion. The dashed lines show spectator nucleons that did not collide with any nucleons from the other nucleus.

3.2 The Glauber Model

3.2.1 Glauber Model Introduction

Nearly everything that is studied in heavy-ion collisions requires some knowledge or at least assumptions of the geometry of said collision which, unfortanately, cannot be studied with current technologies. For this reason various models are used as a starting point. One of said models, the Glauber model, is widely used throughout this field and this analysis. In particular the code used here is one developed by the PHOBOS collaboration [30] but has been adapted to suit PHENIX's needs. Figure 3.3 is a good example of a "collision" in this model.

Nucleon Distribution

The first step is to generate a nucleus by randomly distributing nucleons according to the charge density distribution of the three-parameter Fermi

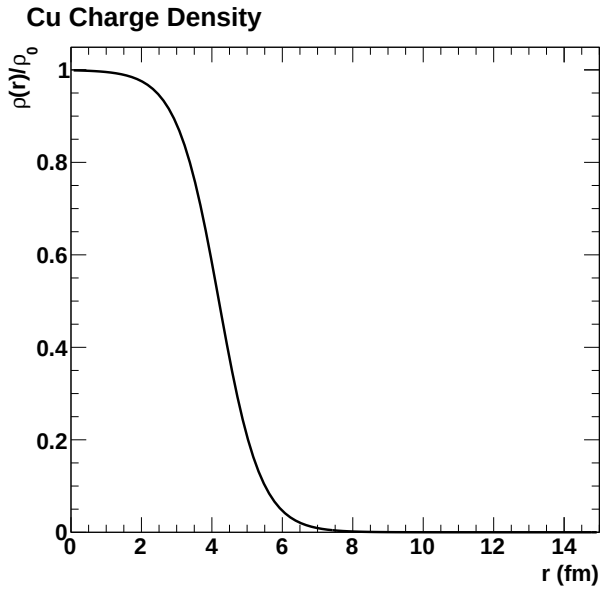

Figure 3.4: The charge distribution used for Cu nuclei.

model 3.1, with parameters obtained from electron scattering experiments [31]:

$$\rho(r) = \rho_0 \frac{1 + w(r/R)^2}{1 + e^{(r-R)/a}}, \tag{3.1}$$

where ρ_0 is nucleon density, R is the nuclear radius, and a is the nuclear skin depth. The wine-bottle parameter, w, represents the amount of deviation from a spherical shape. It should be noted that in this analysis and likely all others reported by PHENIX, Cu and Au have w set to zero which reduces equation 3.1 to the two-parameter Fermi model which is identical to the Woods-Saxon potential except that the former describes charge density (fig. 3.4) and the latter is an energy potential. The Woods-Saxon potential is used widely to describe the structure of the nucleus as it has some attractive features like a flat bottom and the nuclear skin has a smooth transition to zero as one moves away from the center of the nucleus and approaches the surface [32].

Nucleon Cross-section and Overlap

The size of the circles in figure 3.3 is representative of the inelastic scattering cross section, σ_{NN} of nucleons with other nucleons. This quantity is depen-

dent on the center of mass energy and at $\sqrt{s_{_{NN}}} = 200$ GeV, $\sigma_{NN} = 42$ mb where 1 barn $= 10^{-24}$ cm^2. Each of the circles in fig. 3.3 has a ball diameter of [30]:

$$D = \sqrt{\sigma_{NN}/\pi} \tag{3.2}$$

That is to say that if the transverse distance between two nucleons from different nuclei is less than this, they have collided.

The degree to which these spherical nucleons are allowed to overlap during the initial distribution of nucleons set to 0.4 fm, during construction one may allow nucleons to overlap. Also studied was the effect of assuming that each nucleon contains a small, hard core such that no two nucleons from the same nucleus could come within 0.4 fm during construction.

3.2.2 Impact Parameter, b

While the impact parameter, b, is an important quantity, in this field it has largely been supplanted by centrality as a measuring the amount of overlap between nuclei because b cannot be measured directly. An example of impact parameter distributions as a function of centrality can be found in figure 3.5. Somewhat confusingly, A low centrality indicates the most central or head-on collision and has the smallest b. Conversely a peripheral collision will have a high centrality percentage.

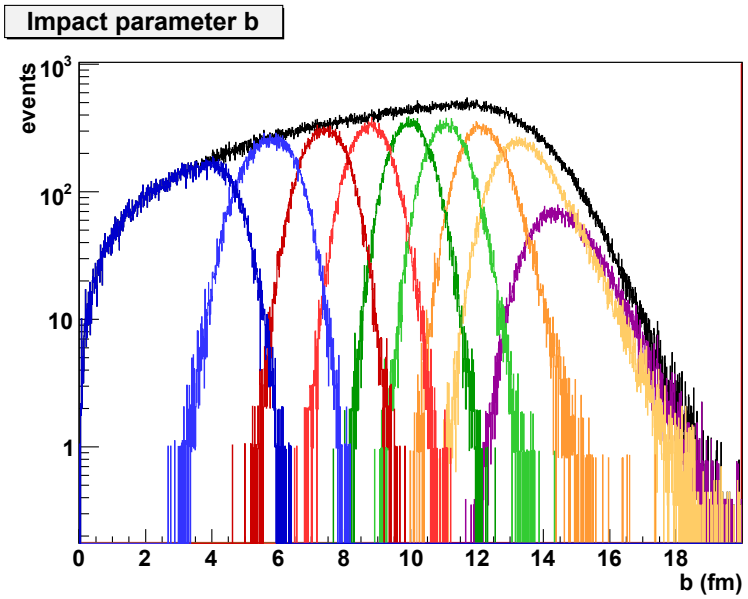

Figure 3.5: The impact parameter distributions in 10% centrality bins.

3.2.3 Number of Participants, N_{part}

The number of participants are simply the number of nucleons from one nucleus which end up overlapping with nucelons from the other nucleus. It should come to no surprise that this is highly dependent how central a collision is. A head-on collision will yield the highest N_{part} as seen in figure 3.7a, maxing out at the sum of the number of protons and neutrons for each nucleus. For Cu+Cu this will be $2 \times 63 = 126$ and for Au+Au, $2 \times 197 = 396$.

Figure 3.6 shows the distribution of N_{part} with the most central collisions starting at the right working its way left as collisions become more peripheral. Each centrality bin shows a spread of N_{part} values where some events that are in the 0-10% category may actually have a higher N_{part} than one from the 20-30% centrality bin.

In figure 3.7b it is apparent that leading contributor to systematic error comes from the trigger efficiency determination covered in section 3.3. A higher trigger efficiency leads to more central events being put in higher centrality bins which would lead to an enhancement of N_{part}. Conversely, a lower trigger efficiency means that more peripheral events will be accepted

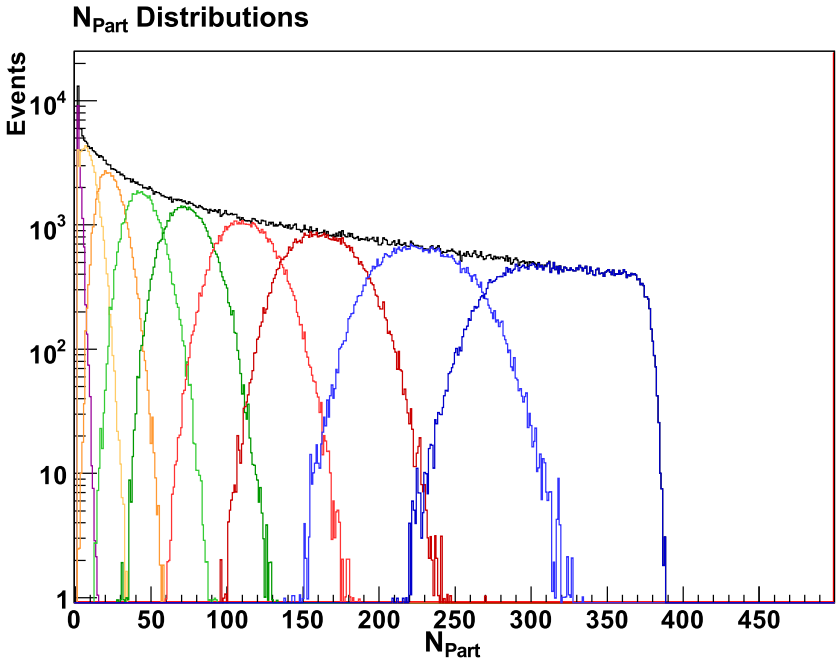

Figure 3.6: The N_{part} distributions for Au+Au $\sqrt{s_{NN}} = 39$ GeV in 10% centrality bins.

into lower centrality bins, diminishing N_{part}.

Adjusting the inelastic scattering cross section gave the expected result. If each nucleon had a larger cross section (a larger circle), it will have a higher probability of colliding with another nucleon.

By changing the parameters of the Woods-Saxon distribution such that each nucleus is more tightly packed, the chances of hitting another nucleon also increase. A constituent nucleons in a sparcely packed nucleus has a greater chance of missing those of the other nucleus.

Using a hard-cored nucleon as opposed to allowing overlaping nucleons did not change the packing of the nuclei appreciably enough to make a difference here.

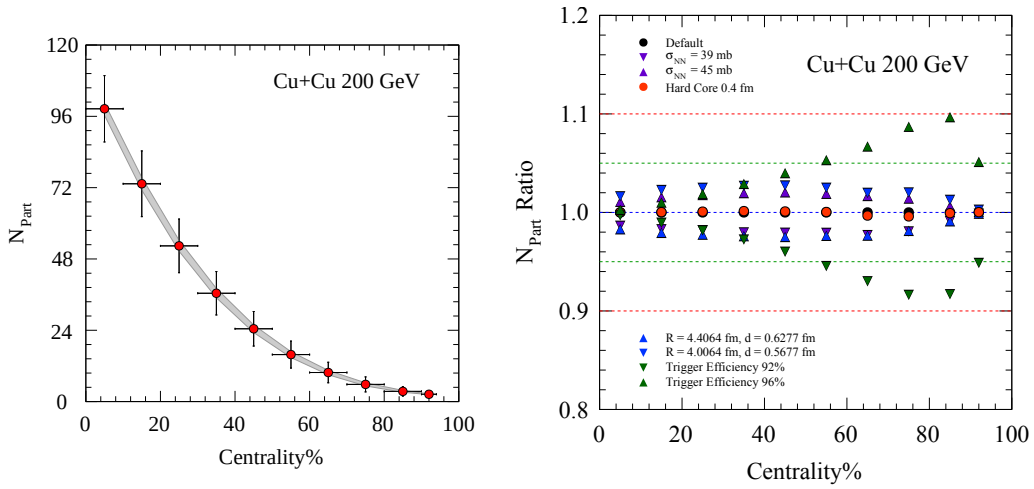

(a) (b)

Figure 3.7: (a) N_{part} as a function of centtrality and (b) its systematic error contributors.

3.2.4 Number of Binary Collisions, N_{coll}

Both N_{part} and N_{coll} are similar Glauber quantities. If a nucleon from nucleus A hits 3 nucleons from nucleus B then there were 4 participants but only 3 binary collisions. If 2 nucleons from A each hit 3 from B there would be 5 participants but 6 binary collisions. The fuzzy relationship that these two quantities have is shown in figure 3.8.

While entirely possible to have a N_{coll} value that is lower than N_{part}, as N_{part} increases, it's increasingly likely that N_{coll} will be higher. Like with N_{part}, N_{coll} distributions like the ones seen in figure 3.9 start from the right and work to the left with increasing centrality.

Both N_{coll} and N_{part} follow the same trend moving to very central to very peripheral collisions as one would expect. The systematic errors shown in figure 3.10b does show a notable difference in regard to the changing the scattering cross section as well as changing the Woods-Saxon parameters.

In a very central collision, increasing the size of the nucleons will mean that there is a greater chance for them to overlap leading to a higher N_{coll}. When considering N_{part}, however, these nucleons that have hit are already wounded (counted). Increasing their size to hit additional wounded nucleons

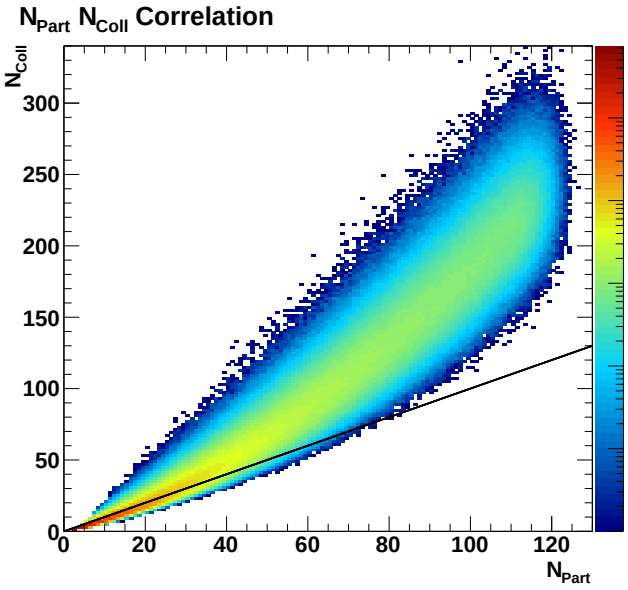

Figure 3.8: The $N_{\rm part}$-$N_{\rm coll}$ correlation for Cu+Cu $\sqrt{s_{NN}} = 200$ GeV . A line has been drawn to show where a 1-to-1 correlation would lie.

will not have too much of an effect.

Similarly, packing the nucleons in tighter will lead to more nucleons being hit but at some point it also saturates when talking about wounded nucleons. When talking about binary collisons, a tighter packing will lead to a greater chance for multiple overlaps. The effect of the trigger efficiency and the hard-cored nucleon on $N_{\rm coll}$ are the same as seen with $N_{\rm part}$.

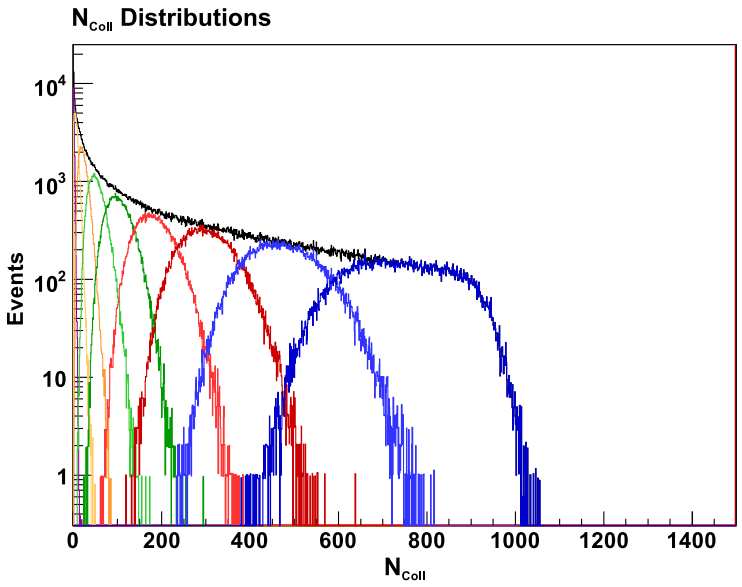

Figure 3.9: The N_{coll} distributions for Au+Au $\sqrt{s_{NN}}$ = 39 GeV in 10% centrality bins.

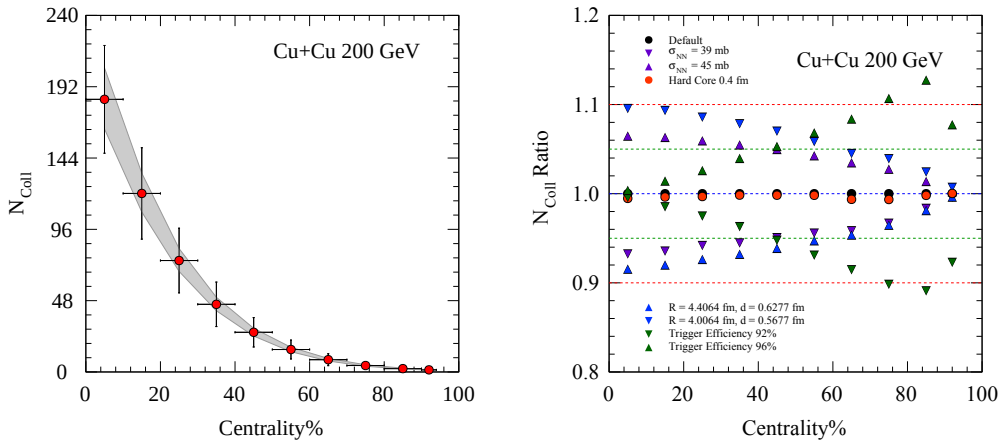

(a) (b)

Figure 3.10: (a) N_{coll} as a function of centtrality and (b) its systematic error contributors.

3.2.5 Ellipticity ϵ_2

The QGP at the time of the collision is largely believed to have an almond-like shape with some amount of eccentricity. While the two nuclei in figure 3.11

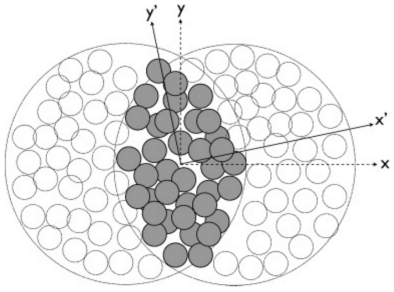

Figure 3.11: The transverse projection of the participant plane may not be colinear with the reaction plane depending on the fluctuations in the participant distribution.

have an impact parameter that is horizontal in the laboratory frame, fluctations in the initial state lead to the participants forming a distribution that is rotated by some amount. This is what we refer to as the participant plane [33]. Because of this, we cannot simply measure the x and y components and measure the eccentricity from that, instead we want to look at the eccentricity relative to the participant plane once the participants have been recentered about zero ($\langle x \rangle = \langle y \rangle = 0$),

$$\epsilon_2 = \frac{\sqrt{\langle r^2 \cos(2\phi) \rangle^2 + \langle r^2 \sin(2\phi) \rangle^2}}{\langle r^2 \rangle}, \tag{3.3}$$

where r is the radial distance of a participating nucleon from the center and ϕ is its azimuthal angle. The participant plane can also be easily found,

$$\psi_2 = \frac{\text{atan2}(\langle r^2 \sin(2\phi) \rangle, \langle r^2 \cos(2\phi) \rangle) + \pi}{2} \tag{3.4}$$

In figure 3.12 we proceed from central to peripheral collisions the eccentricity also increases. Because these collisions are lumpy instead of having a smooth profile, there is some spread in the eccentricity any one event will have. Case in point, while the orange curve represents the 50-60% centrality bin and has a higher average eccentricity than the 40-50% bin, it still has

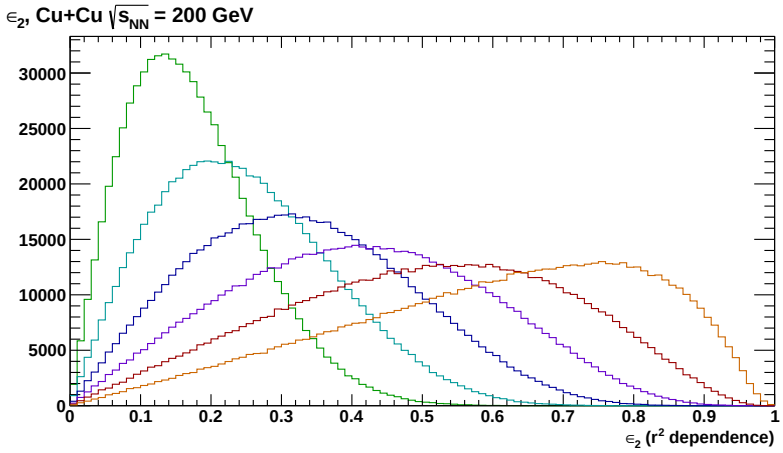

Figure 3.12: The eccentricity ϵ_2 distributions for 0-60% in centrality in 10% centrality bins.

events that register with vanishing eccentricity. Figure 3.13a shows the mean ϵ_2 for 5% centrality bins. It should be noted here that the error bars represent one standard deviation for the distributions that made them. There is also an error band with its contributors shown in figure 3.13b. Each change in the Glauber settings did little to change the ϵ_2 distribution; most everything stayed within 2%. The biggest source of systematic error came from changing the trigger efficiency. A lower trigger efficiency leads to centrality bins containing comparably more peripheral, eccentric events while conversely a higher trigger efficiency lead to centrality bins containing more head-on collisions.

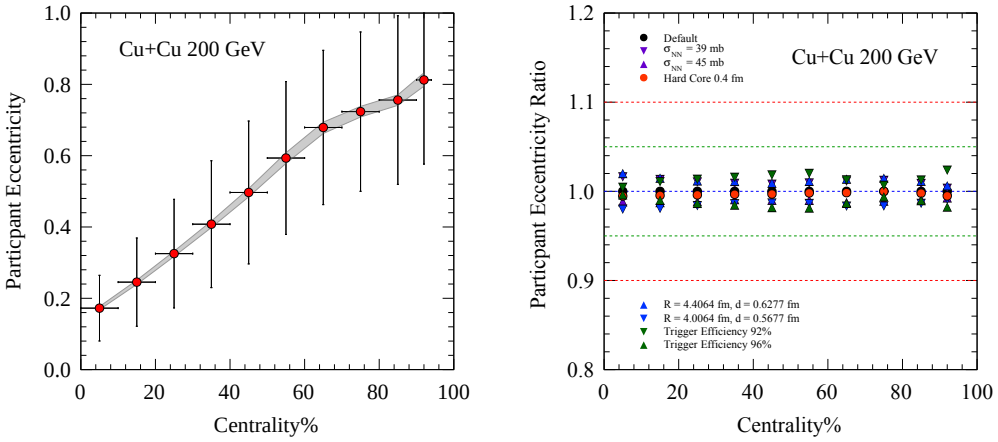

(a) (b)

Figure 3.13: (a) The eccentricity ϵ_2 as a function of centtrality and (b) its systematic error contributors.

3.2.6 Triangularity, ϵ_3

The triangularity of an event follows very much the same logic as the ellipticity, ϵ_2, but instead of looking at a periodicity of 2, one uses 3.

$$\epsilon_3 = \frac{\sqrt{\langle r^2 \cos(3\phi)\rangle^2 + \langle r^2 \sin(3\phi)\rangle^2}}{\langle r^2 \rangle}, \tag{3.5}$$

and similarly, its participant plane is defined by,

$$\psi_3 = \frac{\text{atan2}(\langle r^2 \sin(3\phi)\rangle, \langle r^2 \cos(3\phi)\rangle) + \pi}{2} \tag{3.6}$$

While both ϵ_2 and ϵ_3 increase initially with centrality, it is clear that ϵ_3 begins to saturate. This largely has to do with the fact that ϵ_2 is greatly aided by the overall geometry of the collision whereas ϵ_3 has more to do with the fluctuations within a givien collision.

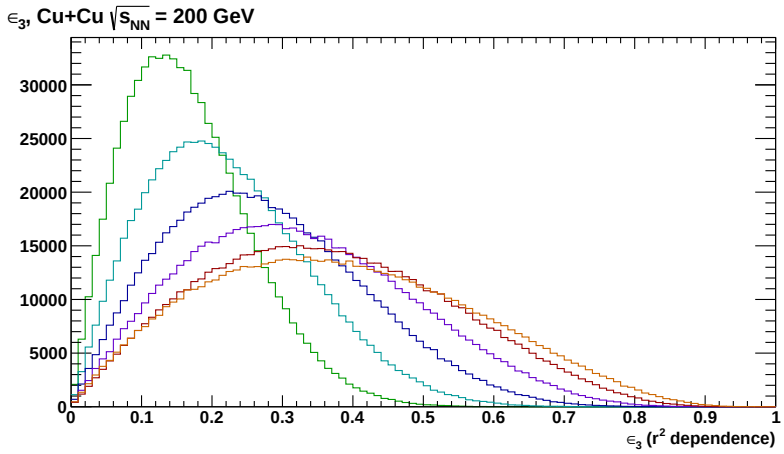

Figure 3.14: The eccentricity ϵ_3 distributions for 0-60% in centrality in 10% centrality bins.

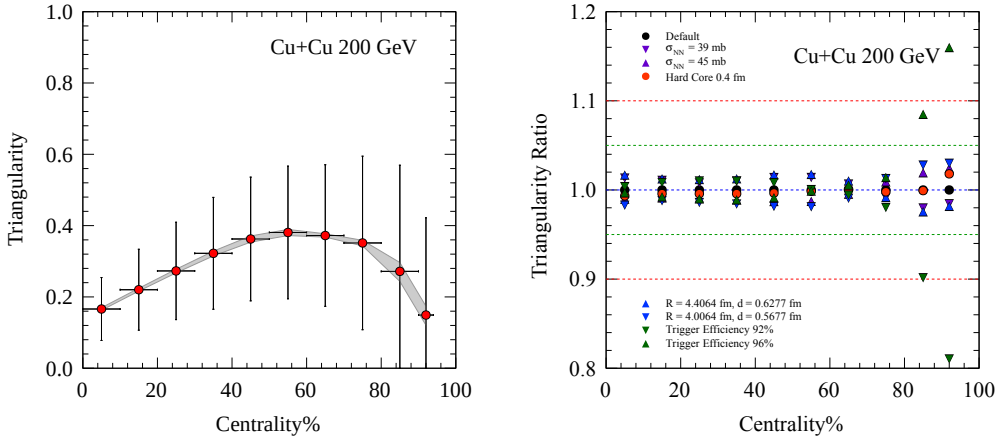

(a) (b)

Figure 3.15: (a) The eccentricity ϵ_3 as a function of centtrality and (b) its systematic error contributors.

Table 7.9 contains the Glauber values that were used in sections 5.3.2 and 5.3.3

3.3 Centrality Calibration

At this stage the Glauber values that have been output need to be related to experimental values. In order to do this we take the negative binomial distribution [34]:

$$P(n,\mu,k) = \frac{\Gamma(n+k)}{\Gamma(k)n!}\frac{(\mu/k)^n}{(1+\mu/k)^{n+k}}, \tag{3.7}$$

where $\Gamma(n) = (n-1)!$, $P(n,\mu,k)$ is the probability given n successes before k failures of a series of trials with an equal probability of successes and failures. If these trials are not correlated and are truly independent, the factor $1/k$ vanishes yielding the Poisson distribution which is frequently used to describe nuclear decays [35]. The mean of the distribution μ is related to its variance σ^2 by:

$$\frac{\sigma}{\mu}^2 = \frac{1}{k} + \frac{1}{\mu} \tag{3.8}$$

This distribution is then convolved with the N_{part} distribution [36]:

$$\frac{1}{\varepsilon(N_{\text{hit}})}P(N_{\text{hit}}) = \sum_{N_{\text{part}}} NBD(\mu N_{\text{part}}, kN_{\text{part}}) \times MCG(N_{\text{part}}), \tag{3.9}$$

The simulated detector response (green) is then matched to the BBC data (blue) as shown in figure 3.16. The flat area of this logarithmic plot, being rather featureless, is not terribly helpful for determing μ and k. It his helpful, however, for area normalization between the two plots so that fitting can take place. The parameter μ largely affects the width of the distribution so it must be found first. The "knee" on the right-hand side of this plot can be adjusted by varying k. On the very left-hand side the green curve clearly lies above the blue. The green, representing and ideal detector, does not have the BBCLL1 trigger applied and therefore the difference in the intergrals in that region are the estimated events that are lost due to the trigger inefficiencies. The ratio, fig. 3.17, better illustrates the region of interest below a BBC charge sum of 100. The trigger efficiency is finally established by parameterizing

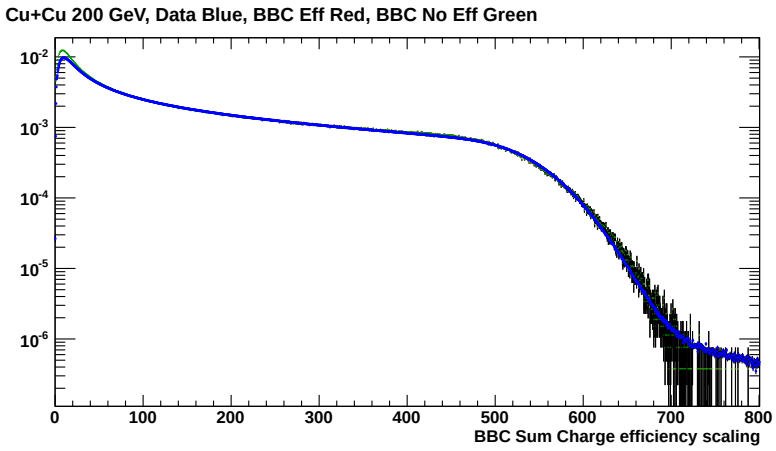

Figure 3.16: Estimated BBC charge deposition from the Glauber $N_{\rm part}$ distribution of Cu+Cu $\sqrt{s_{_{NN}}} = 200$ GeV . Green points are from Glauber/NBD and the blue points are from data.

this curve by the following:

$$\varepsilon(N_{\rm hit}) = 1 - \exp\left[\frac{N_{\rm hit} - threshold^{power}}{slope}\right], \tag{3.10}$$

where *slope* and *threshold* define the shape of the curve and *threshold* is just a minimum $N_{\rm hit}$ value to be fit. The trigger efficiencies were $93 \pm 2\%$ and $94 \pm 2\%$ for Cu+Cu $\sqrt{s_{_{NN}}} = 200$ GeV and Au+Au $\sqrt{s_{_{NN}}} = 200$ GeV respectively. Finally the BBC charge distribution is divided into centrality bins like in figure 3.18 assuming that the data only contains $93 \pm 2\%$ or $94 \pm 2\%$ of events and that the events lost are at the end of the towards the higher centralities.

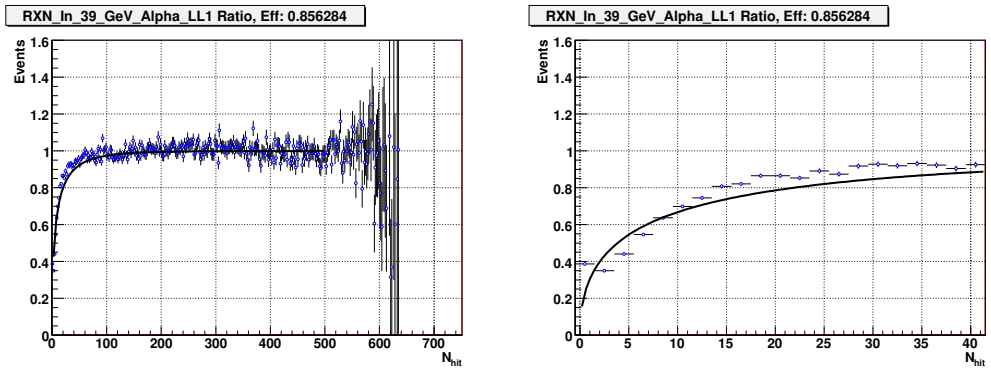

(a) (b)

Figure 3.17: Dividing the Glauber/NBD result by the data shows losses due to the BBCLL1 Trigger. This example is from a Run10 Au+Au $\sqrt{s_{NN}} = 39$ GeV trigger efficiency study that I was involved with. (b) is a zoomed in version of (a) in the region of interest.

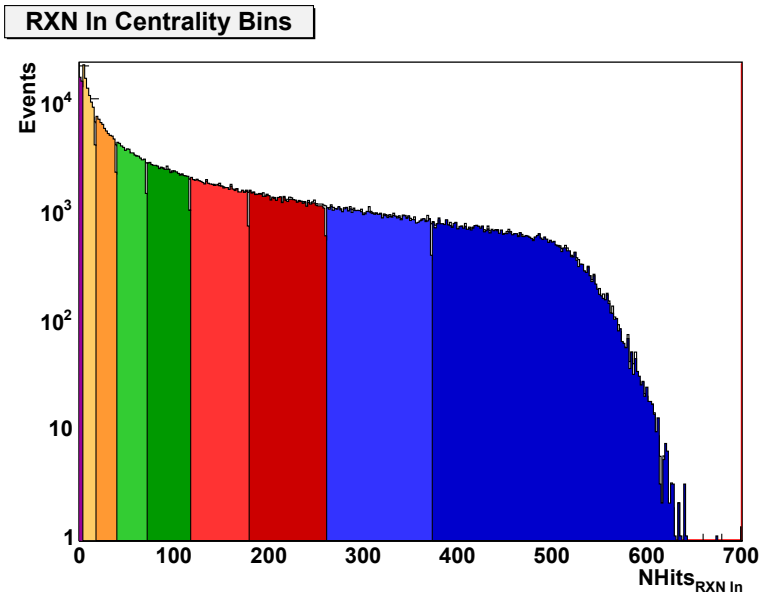

Figure 3.18: The BBC Distribution for Run10 Au+Au $\sqrt{s_{NN}} = 39$ GeV chopped into 10% centrality bins.

Chapter 4
Analysis

4.1 Event Plane Analysis

4.1.1 Event Plane Overview

The event plane method is a way of studying collective flow of particles emitted during an event measured relative to the event plane. The event plane is our best measurement of the reaction plane due to having a finite number of particles and therefore having a finite ability to resolve its angle.[10]

An outline of the proceedure is as follows: We measure the event plane with a detectors that have a full 2π azimuthal coverage. Then we have to find determine how well we can resolve the event plane. And finally the particles, measured relative to the event plane, are to be decomposed into a Fourier series.

4.1.2 Event Plane Determination

In this section, calibration of the n^{th} order event plane using one of the forward detectors will be covered. In 2005, the BBC was really the only detector to use in order to determine event planes. By 2007 there were three good choices, the BBC, RXN, and MPC. For brevity these detectors will just be called event plane detectors or EPD. Of these three, the RXN had the best performance.

Regarding only the transverse plane, the degree to which we the n^{th} harmonic of the azimuthal anisotropy flows is described by what is known as the flow vector:

$$\vec{Q}_n = (Q_x, Q_y) \tag{4.1}$$

While in practice the BBC detector response is a not a binary hit or miss, figure 4.1 still serves as a good visualization of an event plane that is largely horizontal in the laboratory frame.

Quantitatively, the event plane Ψ_n can be determined by summing the weighted signal of the azimuthal angles ϕ_i of each channel in the event plane detector.

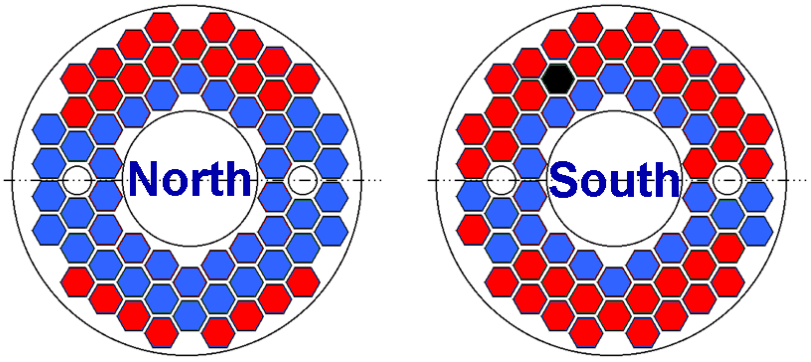

Figure 4.1: A simple figure showing hits in both sides of the BBC largely in the v_2 event plane. From [18].

$$Q_x \equiv |\vec{Q}_n| \cos(n\Psi_n) = \sum_i^M w_i \cos(n\phi_i), \tag{4.2}$$

$$Q_y \equiv |\vec{Q}_n| \sin(n\Psi_n) = \sum_i^M w_i \sin(n\phi_i), \tag{4.3}$$

$$\Psi_n = \frac{1}{n} \arctan\left(\frac{Q_y}{Q_x}\right) \tag{4.4}$$

Where M denotes the number of channels in the EPD and ϕ_i is the azimuthal angle of the geometric center of each channel, and w_i its weight, the charge deposited. It should come as no surprise that the range of Ψ_n is $-\pi/n < \Psi_n \leq \pi/n$.

A standard $\vec{Q}_n$ recentering and flattening technique is then used to remove the residual non-uniformities that may arise due to engineering limitations or in the event disabled detector components.

The orientation that these nuclei hit each other is completely random, making the event plane distribution isotropic in azimuth. The black markers in figure 4.2 show an example of the event plane distribution of all events within a run segment before any correction is applied. Finessing the detector energy calibration on a ring-by-ring basis, the event plane distribution is flattened somewhat shown in light green. The $\vec{Q}_n$ distributions tend to look like a 2D Gaussian function which may or may not be centered about zero.

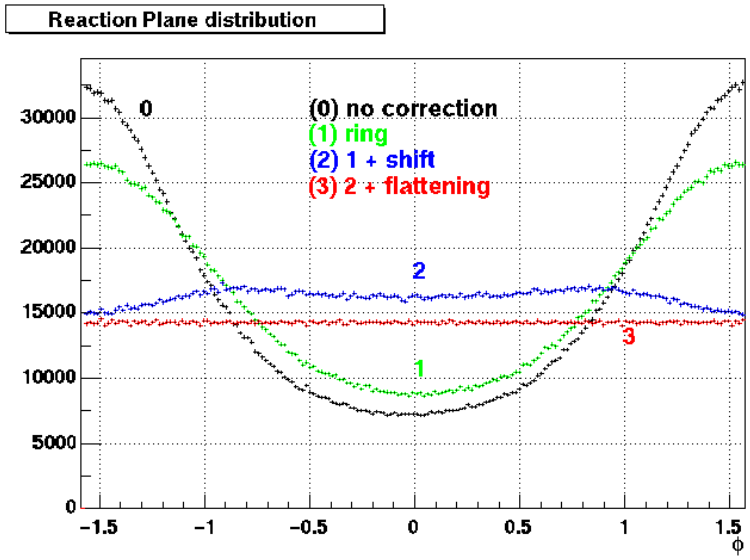

Figure 4.2: The event plane distribution at different stages in the calibration process.

After recentering this distribution there are still some irregularities depicted by the blue markers. At this point we perform a Fourier decomposition and remove any unwanted elements, guaranteeing a flat final distribution (red markers).

In the end, what one hopes to see is a one-to-one correlation between event planes measured in the north and south event plane detectors like that of figure 4.3.

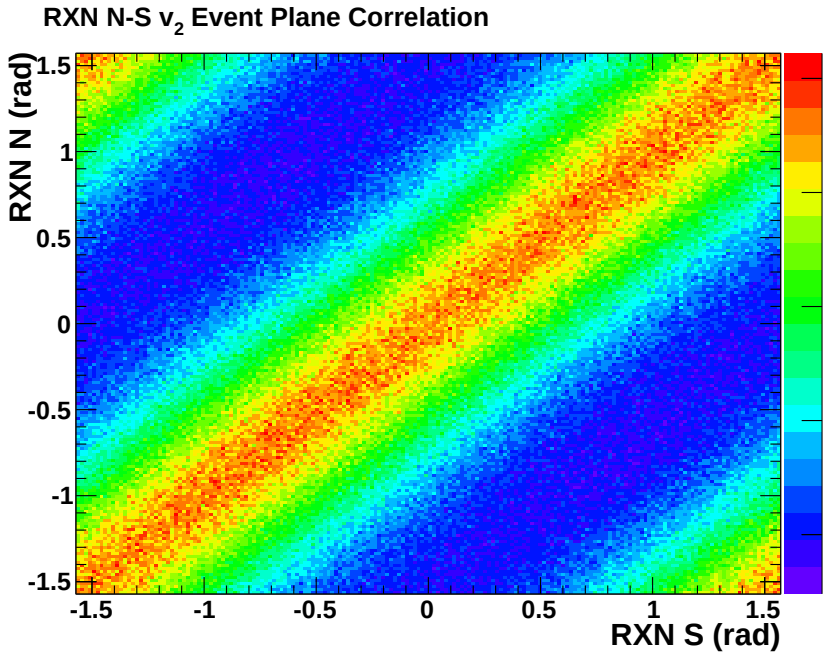

Figure 4.3: Correlation between the North and South RXN v_2 event plane measurements.

4.1.3 Event Plane Resolution

Event plane correlations seen in fig. 4.3 look linear, however there is a spread between the north and the south signals. An event plane measured at Φ_2 in the north may not yield Φ_2 in the south, the amount of spread between these two measurements is what is known as the event plane resolution. The better the resolution of the detector, the less the spread will be between north and south. It is entirely possible to measure v_n using an m^{th}-order event plane provided that m is a factor of $(n = km)$. And it is possible to measure v_n with Φ_1 however the event plane resolution suffers dramatically with increasing k.[10] The best practice is to measure v_n using Φ_n plane.

Two-Subevent Method

The lengthy derivation for the event plane resolution is covered in references [37] but the final result will be shown here where $n = 2, k = 1$.

$$\text{Res}\{n\Psi_n\} = \langle\cos[n(\Phi_n - \Psi_n)]\rangle \tag{4.5}$$

$$= \frac{\chi_n\sqrt{\pi}}{2}e^{-\frac{\chi_n^2}{2}}\left[I_0\left(\frac{\chi_n^2}{2}\right) + I_1\left(\frac{\chi_n^2}{2}\right)\right] \tag{4.6}$$

Where I_α is a modified Bessel functions of the first kind, and χ_n, known as the "resolution parameter", is a comparison between strength of the flow and finite-multiplicity fluctuaitons.

We attempt to find this resolution using the two-subevent method wherein some particles from an event are analyzed separately from other particles in an event. A typical choice is to use the sets of particles going into one of the north event plane detectors and another going into the south.

$$\langle\cos[n(\Phi_n^N - \Phi_n^S)]\rangle = \langle\cos[n(\Phi_n^N - \Psi_n)]\rangle\langle\cos[n(\Phi_n^S - \Psi_n)]\rangle \tag{4.7}$$

For a symmetric collision, using the same detector systems, at the same psedorapidity ranges, it is not unreasonable to assume that the north and the south detectors will have similar, if not the same, multiplicities and event plane resolution.

$$\langle\cos[n(\Phi_n^N - \Psi_n)]\rangle = \langle\cos[n(\Phi_n^S - \Psi_n)]\rangle \tag{4.8}$$

Combining equations 4.7 and 4.8 we get:

$$\langle\cos[n(\Phi_n^{N(S)} - \Psi_n)]\rangle = \sqrt{\langle\cos[n(\Phi_n^N - \Phi_n^S)]\rangle} \tag{4.9}$$

Once the resolution parameter of the subevent has been established by inverting eq. 4.6, it can be related to the full event's resolution parameter by $\chi_n = \sqrt{2}\chi_{n,\text{sub}}$, The $\sqrt{2}$ factor comes from theh two-fold increase in multiplicity between the sub and full event. The new χ_n can be reinserted into eq. 4.6 in order to find the event plane resulotion for the full event.

Three-Subevent Method

Provided enough options for dividing an event into subevents, one may choose to use the three-subevent method,

$$\mathrm{Res}\{n\Psi_n^{\mathrm{A}}\} = \sqrt{\frac{\langle \cos n\left(\Psi_n^{\mathrm{A}} - \Psi_n^{\mathrm{B}}\right)\rangle \langle \cos n\left(\Psi_n^{\mathrm{A}} - \Psi_n^{\mathrm{C}}\right)\rangle}{\langle \cos n\left(\Psi_n^{\mathrm{B}} - \Psi_n^{\mathrm{C}}\right)\rangle}} \tag{4.10}$$

where A, B and C indicate different subevent planes which may or may not have disparate η values. (e.g. A = RXN, B = $\mathrm{BBC_N}$ and C = $\mathrm{BBC_S}$).

4.1.4 Event Plane Final Step

In order to study v_n with this method the n^{th}-order event planes and resolutions must be found a priori as covered in sections 4.1.2-4.1.3. The azimuthal angles of a different set of particles (e.g. central arm tracks) are then binned relative to the n^{th}-order event plane (Φ_n).

The resulting distribution, can be written as a Fourier series

$$\frac{dN}{d\Delta\phi} = \frac{1}{2\pi}\left[1 + \sum_{n=1}^{\infty} 2v_n^{\mathrm{obs}} \cos n(\phi - \Phi_n)\right] \tag{4.11}$$

Equation 4.11 is almost identical to the eq. 1.6 except that the observed v_n^{obs} values are lower than the true v_n due to the dispersion of the event plane Φ_n about the true reaction plane Ψ_n

except that the true reaction plane, Ψ_n is unknown, we are using the event plane, Φ_n which has so we are only measuring the observed v_n, denoted v_n^{obs}.

$$v_n^{\mathrm{obs}} = \langle \cos n(\phi - \Phi_n)\rangle, \tag{4.12}$$

Where the angled brakets indicate the average between all particles and events. Dividing this result by the event plane resolution yields the true v_n.

$$v_n = \frac{v_n^{\mathrm{obs}}}{\mathrm{Res}\{n\Psi_n\}} = \frac{\langle \cos n\left(\phi - \Psi_n\right)\rangle}{\langle \cos n\left(\Psi_n - \Phi_n\right)\rangle}, \tag{4.13}$$

Measurement of the different event planes and their resolutions are often incorporated in the systematic error for v_n measurements since the choice of detector should have no bearing on the true value of v_n for an event.

4.2 Long-Ranged, Two-Particle Method

4.2.1 Two-Particle Correlation Method

The most common two-particle azimuthal correlation analyses performed by PHENIX involves using tracks measured in central arms which span a pseudorapidity range of $|\eta| \leq 0.35$ and therefore have a maximum $\Delta\eta = 0.7$. The correlation function in $\Delta\phi - \Delta\eta$ space as in figure has a pronounced peak for pairs that are very close in $\Delta\phi$ and $\Delta\eta$ caused by non-flow effects like jets in addition to the flow effects which are seen globally.

In order to avoid these non-flow effects, tracks were correlated between the BBC and the central arm ($2.6 < |\Delta\eta| < 4.1$), the $\mathrm{BBC_S}$ with the $\mathrm{BBC_N}$ ($6.2 < |\Delta\eta| < 7.3$). In Run7, the RXN also became available. Between the RXN and the central arm ($0.7 < |\Delta\eta| < 2.3$), the $\mathrm{RXN^S}$ with the $\mathrm{RXN^N}$ ($2.3 < |\Delta\eta| < 3.7$)

This method relies heavily on the idea that azimuthally, particles are only correlated because they originated in the same event where some amount of flow was present and that one event will not influence another. An excellent derivation from first principles can be found in reference [38]. Some of the major points will be highlighted here.

In general, for each p_T and centrality bin, a distribution for the number of all of the combinations of pairs (N^{AB}) as a function of relative angle ($\Delta\phi \equiv \phi_A - \phi_B$) is generated. The labels A and B are simply used to denote two sets of tracks being used. In the case of a standard two-particle correlation used in jet studies they can be particles of different p_T or if one were studying the correlations between π^0 production and photons, one could assign $A \equiv \pi^0$ and $B \equiv \gamma$. In this case, A can be the full BBC and B might be the central arm tracks, A can also be the $\mathrm{BBC_N}$ and B, the $\mathrm{BBC_S}$. Likewise one can substitute the RXN for the BBC. For the sake of brevity, we will use the term EPD (event plane detector) to mean either the BBC or the RXN. For a single event, there should be some relation between N^A and N^B and therefore N^{AB}_{same} would hopefully reflect that. There is, however the problem that all combinations of particles were taken and so the $dN^{AB}_{\mathrm{same}}/d\Delta\phi$ distribution by itself is not particularly informative. Comparing the N^{AB} ratio between correlated and uncorrelated pairs we arrive at the correlation function $C(\Delta\phi)$:

$$C(\Delta\phi) \equiv N \cdot \frac{N^{AB}_{\mathrm{same}}(\Delta\phi)}{N^{AB}_{\mathrm{mix}}(\Delta\phi)}, \tag{4.14}$$

where N is the ratio of factors that area normalize each pair distribution. While N^{AB}_{same} may have an intuitive meaning, N^{AB}_{mix} is slightly more involved. Here particles of group A are taken from the event in hand, and particles that make group B are taken from a pool of events that are in the same centrality and z-vertex bin. Assuming that there is no transverse polarization in the beam, all collisions should happen isotropically and therefore there should be no azimuthal correlation between a particle in one event and another particle in a completely separate event [39]. This mixed event distribution will still contain information about detector response, and she shape of the combinatorial distribution. These effects are all cancelled out in the ratio.

With the single particle distributions following the form of equation 1.6, The final correlation function will be

$$C(\Delta\phi) = 1 + \sum_{n=1}^{\infty} 2\langle v_n^{\text{A}} v_n^{\text{B}}\rangle \cos(n\Delta\phi), \tag{4.15}$$

where the brackets denote that this is the average over all events.

These correlation functions are produced twice. In one instance A is the central arm tracks (CNT) and B is one of the event plane detectors (EPD). In another instance the North and South EPDs are used individually, $A \equiv \text{EPD}_{\text{S}}$ and $B \equiv \text{EPD}_{\text{N}}$. This yields two values, $\langle v_n^{\text{CNT}} v_n^{\text{EPD}}\rangle$, $\langle v_n^{\text{EPD}_{\text{S}}} v_n^{\text{EPD}_{\text{N}}}\rangle$. Factorization of these products is the key to this analysis:

$$\langle v_n^{\text{A}} v_n^{\text{B}}\rangle = \langle v_n^{\text{A}}\rangle\langle v_n^{\text{B}}\rangle \tag{4.16}$$

Should the v_n measured in EPD_{N} be the same as that measured in the EPD_{S} then

$$\langle v_n^{\text{EPD}}\rangle = \sqrt{\langle v_n^{\text{EPD}_{\text{N}}} v_n^{\text{EPD}_{\text{S}}}\rangle} = \sqrt{\langle v_n^{\text{EPD}_{\text{N}}}\rangle^2} \tag{4.17}$$

This value can then be used in

$$\begin{aligned}\langle v_n^{\text{CNT}}\rangle &= \langle v_n^{\text{CNT}}\rangle\langle v_n^{\text{EPD}}\rangle / \langle v_n^{\text{EPD}}\rangle \\ &= \langle v_n^{\text{CNT}} v_n^{\text{EPD}}\rangle / \langle v_n^{\text{EPD}}\rangle \\ &= \langle v_n^{\text{CNT}} v_n^{\text{EPD}}\rangle / \sqrt{\langle v_n^{\text{EPD}_{\text{N}}} v_n^{\text{EPD}_{\text{S}}}\rangle}\end{aligned} \tag{4.18}$$

At this point we arrive at a single v_n point for the hadrons measured in the central arm for a centrality and p_T bin. Details about the EPD_{S}-EPD_{N},

and EPD-CNT correlations will be presented in greater detail in the following sections.

4.2.2 Run and Event Selection

Run Selection

From the calibrated Cu+Cu $\sqrt{s_{NN}} = 200$ GeV minimum bias dataset containing 508 M events, two cuts were employed to help introduce incleased quality assurance of the result. A centrality flatness cut was first performed since a non-flat distribution could indicate that the centrality was not calibrated correctly which could have some effects on centrality dependent measurements like this.

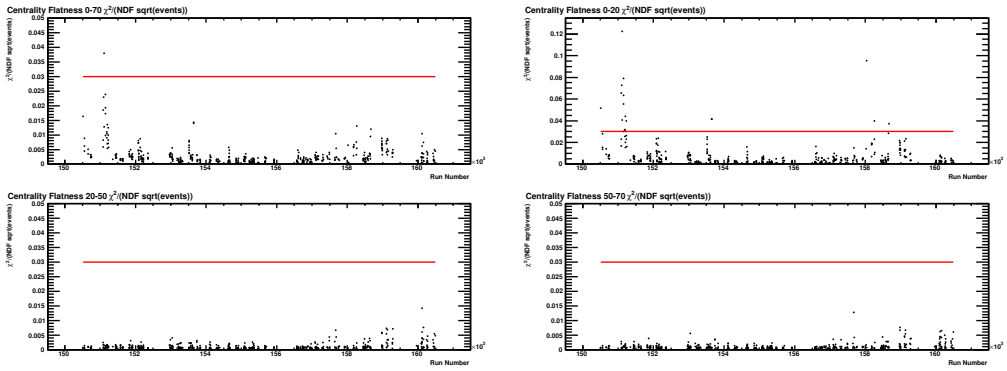

Figure 4.4: Centrality flatness of runs for the Cu+Cu $\sqrt{s_{NN}} = 200$ GeV . Anything above the red line at $\chi^2/(NDF\sqrt{N_{\text{events}}}) = 0.03$ is not used.

This centrality flatness cut was performed in several regions and it was found that the 0-20% centrality region was the most likely place to show problems. Cutting out runs where $\chi^2/(NDF\sqrt{N_{\text{events}}})$ exceeded 0.03, the 484 M events of the original 508 remained, a 95.3% retention. The effect of the z-vertex shape was also studied since an anomalous distribution could be indicative of a detector problem.

Fitting z-vertex distributions like ones found in figure 4.5, to a simple Gaussian function, the descriptive mean and standard deviation values could be plotted.

In figure 4.6 there clear outliers where three runs had skewed distributions and another handful had broader distributions than were expected. The

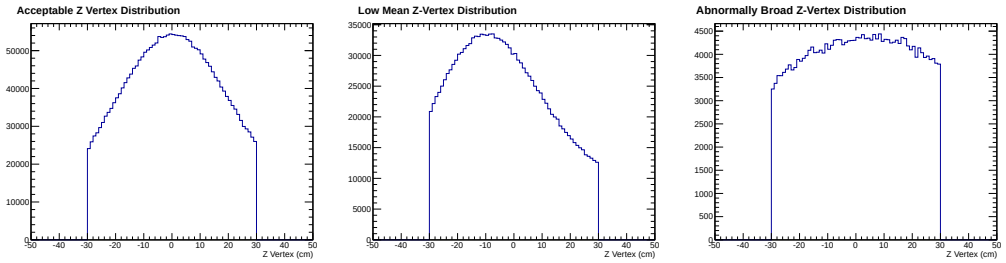

(a) (b) (c)

Figure 4.5: Three different z-vertex distributions for three different runs. (a) is an acceptable z-vertex distribution. (b) The mean value of this distribution is far from the nominal crossing point of the PHENIX detector. (c) The z-vertex distribution is unusually broad.

green box has limits at -7 cm $\leq \langle z \rangle \leq$ 7 cm, 15 cm $\leq \langle \sigma_z \rangle \leq$ 35 cm, representing a loose cut that only excludes the most offensive runs. The red box is far more restrictive with limits at -2 cm $\leq \langle z \rangle \leq$ 2 cm, 19 cm $\leq \langle \sigma_z \rangle \leq$ 26 cm. For the purposes of this study, the loose cut was what had been found to have the best balance data quality and numbers of events. After the loose cut, 461 M events remained which is 90.7% of the minimum bias events.

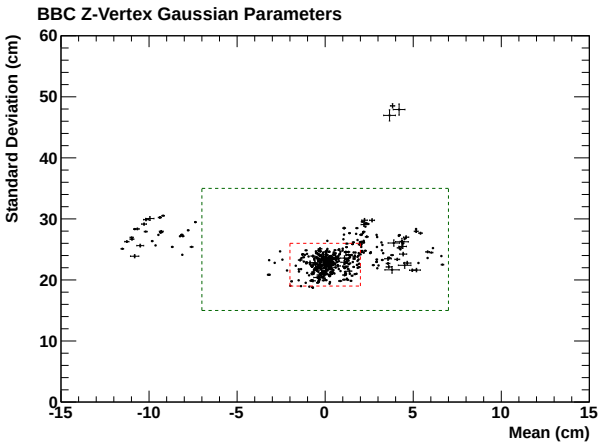

Figure 4.6: A two-dimensional plot showing the means and the standard deviations of the z-vertex distributions for all of the runs in the Cu+Cu $\sqrt{s_{NN}} = 200$ GeV dataset.

Event Selection

There were only a few event cuts that have been employed here. Firstly the z-vertex of the event must occur within 30 cm of the nominal collision vertex. An event must have satisfied the BBCLL1 requirement of a coincident hit in the BBC North and BBC South. When employing this method in Au+Au and using the RXN detector, An event must have at least one hit in the RXN.

Track Selection

Reconstructed charged tracks measured in the central arm needed to meet to meet the following requirements:

As stated in section 3.1, the drift chamber is critical for track reconstruction. Tracks are tagged depending on the track reconstruction algorithm's ability to resolve unique tracks given hits in the X1, X2, and UV tracks in the DC as well as hits in the PC1. Like most PHENIX analyses, the DC quality bits had to be either 31 or 63. A DC quality of 63 that PC1 is found and unique as well as the the UV hits also being found and unique. Though 31 is not quite as good since PC1 is found but ambigious, it indicates that UV still prefers a single PC1 hit. In both cases X1 and X2 are used.

Tracks that hit the PC1 with a z-coordinate that is in excess of 75 cm

from the nominal collision vertex were discarded. That is to say that we required that $|Zed| \leq 75$ cm. This is to ensure that the track goes through the bulk of the fiducial volume of the detector.

Trying to study hadrons, A RICH cut on the number of PMTs found inside the expected ring of Cherenkov photons like shown in fig. 2.13, $n_0 \leq 0$, was employed to remove unwanted electrons. This is not to be confused with the Cherenkov detector quality factor, N_0 [16].

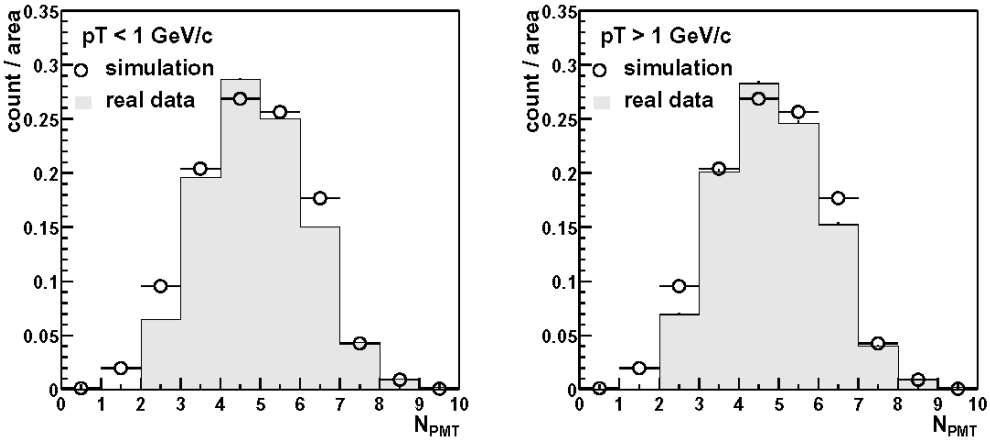

Figure 4.7: The RICH n_0 for electrons.

And finally the track projection was required to be reasonably close to a measured hit in the PC3 $\sigma_{\mathrm{PC3}} \leq 2.5$.

4.2.3 EPD-EPD Correlations

The $dN^{AB}/d\phi$ pair distributions for the event plane detectors is slightly different from correlations where particle tracks are used. Neither the RXN nor the BBC resolve individual tracks rather the sum of the energy deposited into each of the channels (fig. 4.8) should be proportional to the number of particles passing through its acceptance and their azimuthal angles

The azimuthal angles are obtained from the centers of each of the channels.

Since the mixed event technique typically involves mixing with multiple events, it is only natural that its distributions would have more pair combinations than the same event couterpart. This is remedied by area normalizing

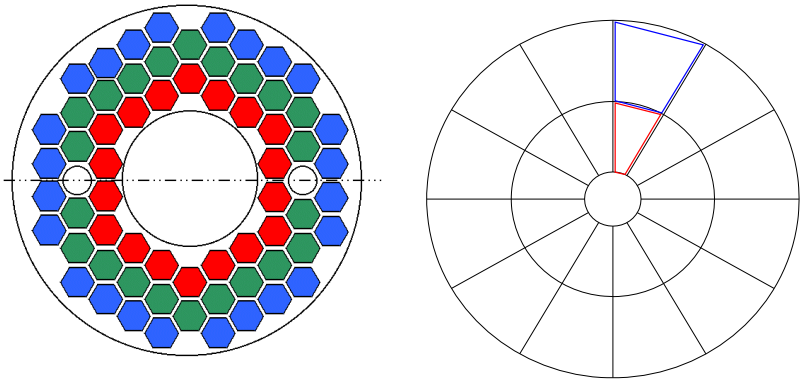

(a) (b)

Figure 4.8: Schematics of the (a) BBC (b) RXN channels.

both distributions before taking their ratios to make the correlation function, $C(\Delta\phi)$.

While figure 4.10 shows a points jumping above and below the line, this is merely caused by binning the correlation function.

If one were to make a correlation between each of the 64 $\mathrm{BBC_S}$ and the 64 $\mathrm{BBC_N}$ channels individually, it would look like figure 4.12a. There are several problems to leaving it like this, however, The biggest problem is that $f(x)$ is not single valued, certain combinations of i, and j vill give rise to the same $\Delta\phi_{i,j}$, but radically different amount of charge deposition. (e.g. an inner ring channel with a middle ring channel will produce a smaller signal than an inner ring with an outer ring.) Another major problem with making a nice looking histogram is that the BBC is made up of many hexagons inscribed into a circle which means that $\Delta\phi$ does not at all have regular spacing in contrast to the RXN.

In figure 4.13 The benefits of of the RXN's twelve-fold symmetry are apparent. The differences in $\Delta\phi$ are such that they are all evenly spaced. For this reason, the RXN correlation function is very easily binned into a histogram with $\Delta\phi = \pi/6$ bins without concern.

Both the RXN and the BBC give ϕ values at the centroid of the channel which may not be truly representative of where the actual particles have passed. For this reason, it is not completely unreasonable to attempt to smear the distribution a little in order to improve the histogram. In fig-

ure 4.14 the foreground and background distributions were smeared by a Gaussian function with a standard deviation of $\sigma = 0.12$ radians (fig. 4.14a) Which produces a correlation function resembling figure 4.14b. One can see that there are still some undesireable peaks with widths comparable to the Gaussian function that smeared it. Ultimately this smearing only helped make the correlation functions look more jumpy and had little effect on the Fourier decomposition. Because there was little improvement in the values that we were seeking, ultimately smearing was not used.

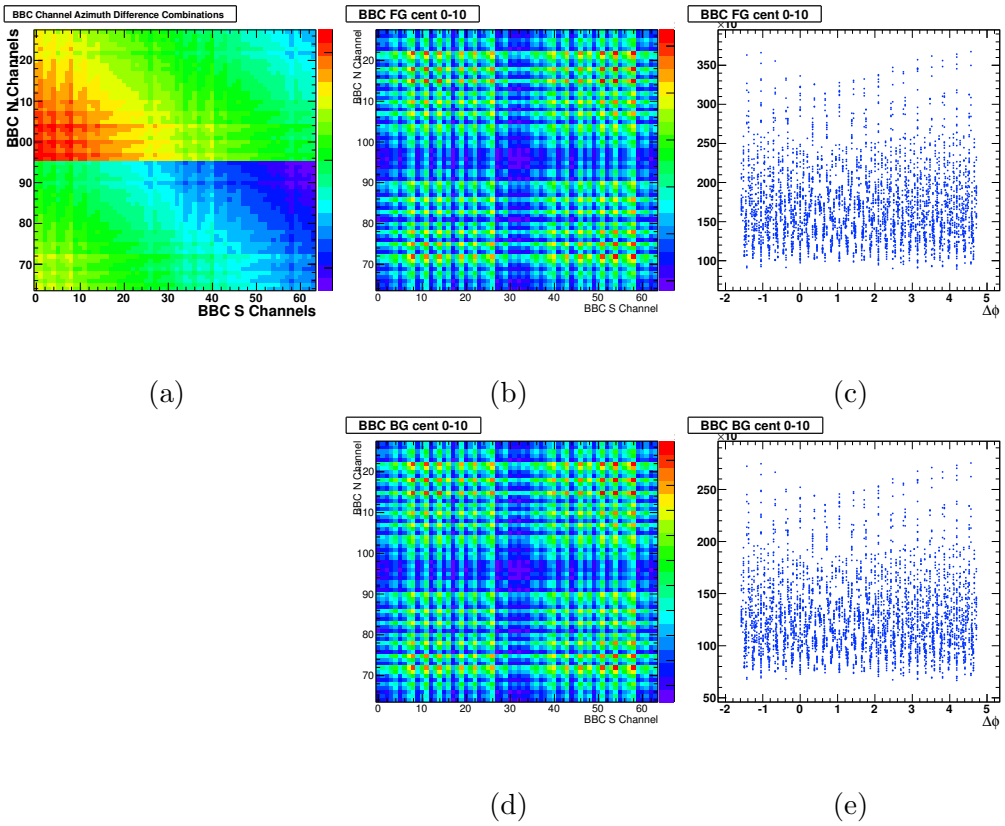

Figure 4.9: Foreground and background distributions of the EPD-EPD correlations. (a) The $\Delta\phi$ between BBC channel combinations. (b) The single event foreground accumulated between each BBC channel combination. (c) The single event foreground distribution with all 4096 channel combinationo. (d-e) The same as (b-c) but using the mixed event backround instead.

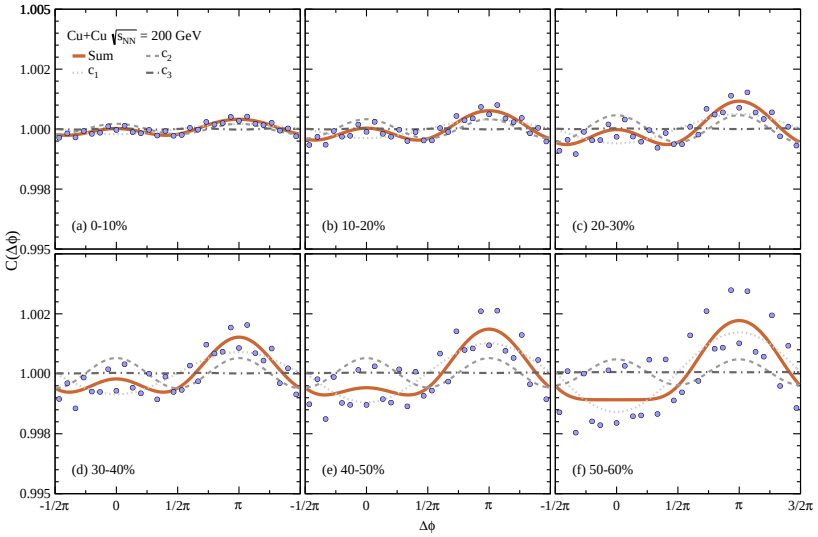

Figure 4.10: The BBC-BBC Correlation function for Cu+Cu $\sqrt{s_{NN}}$ = 200 GeV .

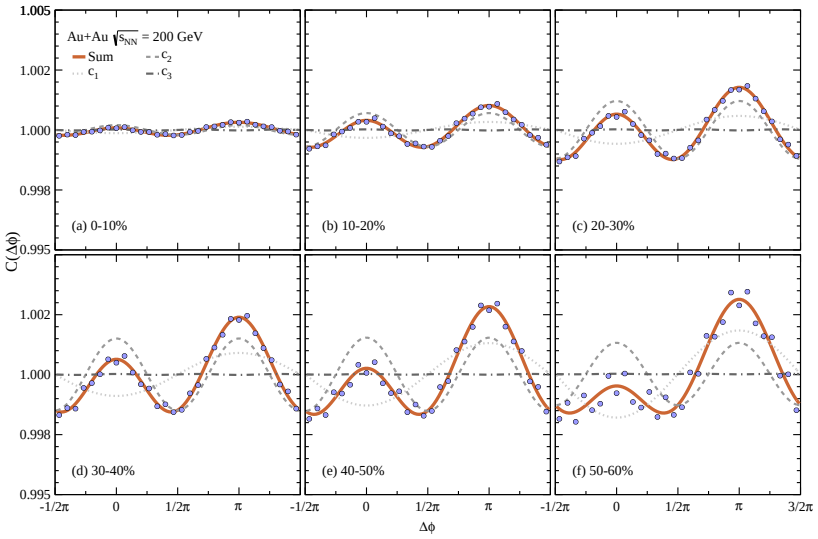

Figure 4.11: The BBC-BBC Correlation function for Au+Au $\sqrt{s_{NN}}$ = 200 GeV .

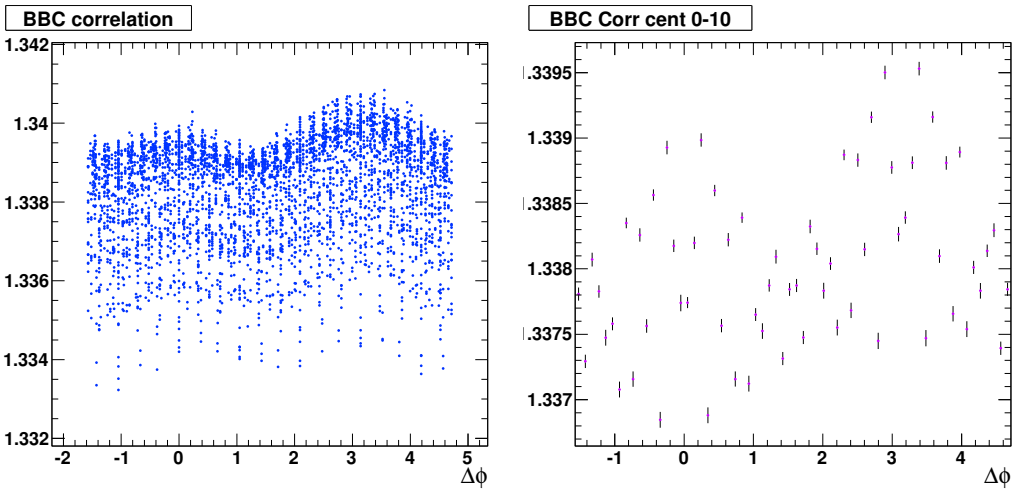

(a) (b)

Figure 4.12: The BBC-BBC Correlation function for Au+Au $\sqrt{s_{NN}}$ = 200 GeV .

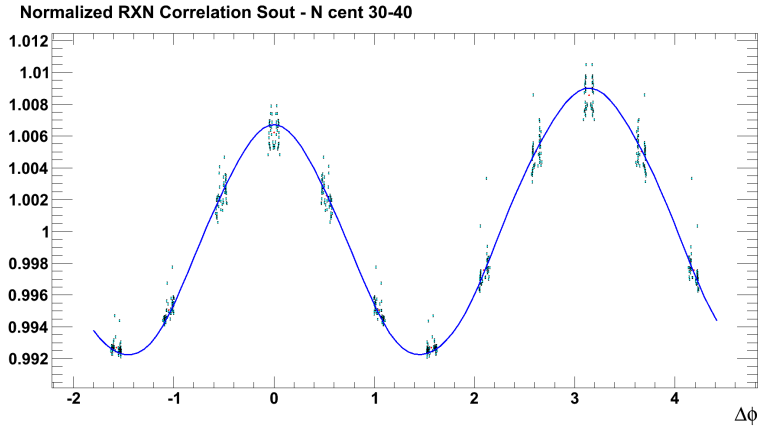

Figure 4.13: A RXN^{N}- RXN^{S}_{OUT} correlation function.

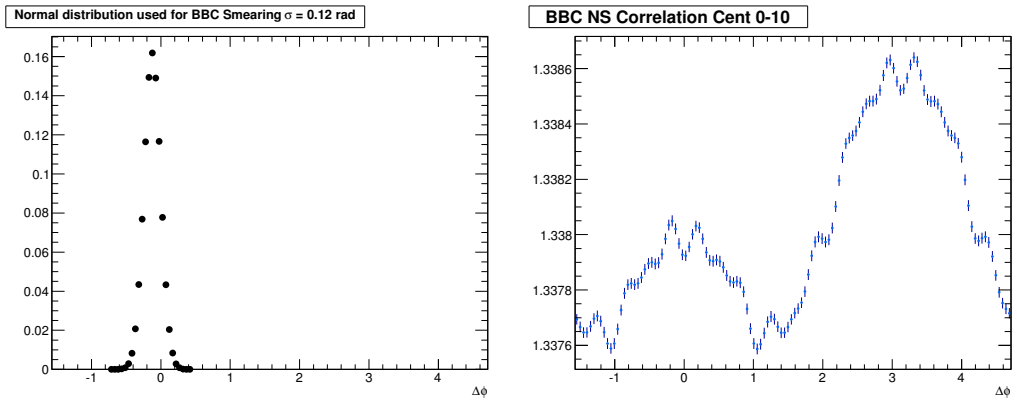

(a) (b)

Figure 4.14: The BBC-BBC Correlation function after smearing by a Gaussian function.

4.2.4 EPD-CNT Correlations

This procedure is similarly carried out between the EPDs and the hadron tracks (HAD) measured in the central arm detectors. In this case the tracks are given unit weight and the channels of the EPDs are given weights proportional to the number of tracks passing through them. An example of the correlation functions for Cu+Cu and Au+Au at $\sqrt{s_{NN}} = 200$ GeV in different centrality ranges can be seen in figure The individual harmonic contributions c_1, c_2, c_3 are shown by the dotted lines and their sum the solid line.

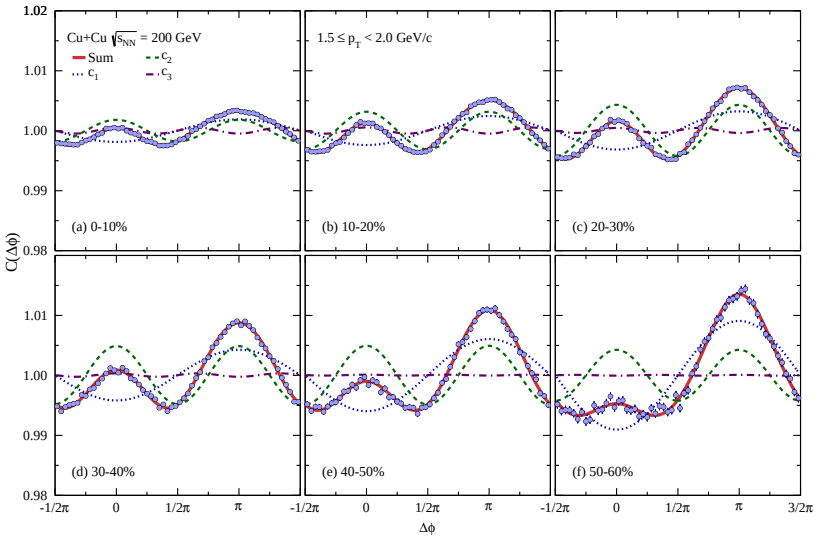

Figure 4.15: The BBC-CNT Correlation function for Cu+Cu $\sqrt{s_{NN}} = 200$ GeV for $1.5 \leq p_T < 2.0$ GeV/c.

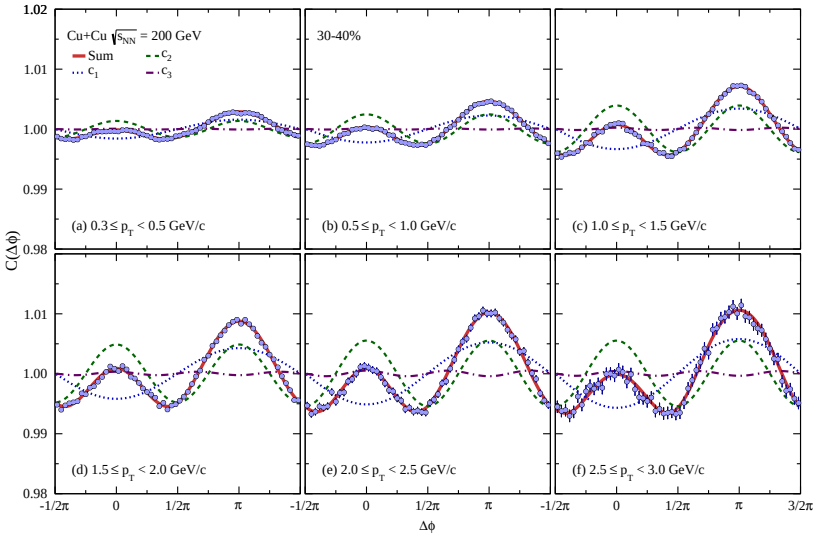

Figure 4.16: The BBC-CNT Correlation function for Cu+Cu $\sqrt{s_{NN}}$ = 200 GeV for the 30-40% centrality bin.

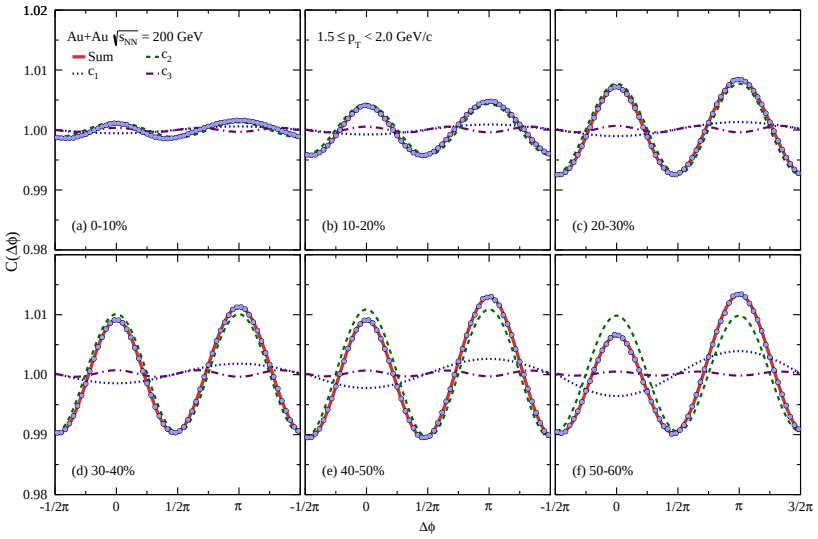

Figure 4.17: The BBC-CNT Correlation function for Au+Au $\sqrt{s_{NN}}$ = 200 GeV for $1.5 \leq p_T < 2.0$ GeV/c.

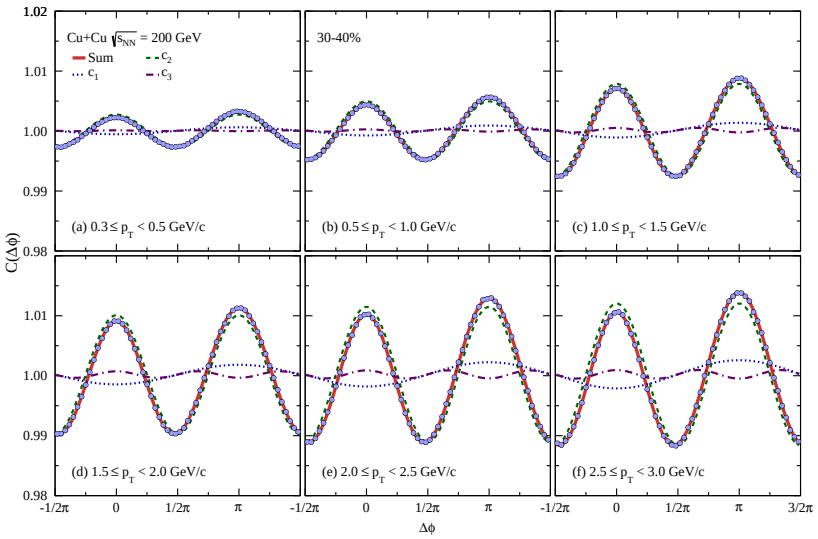

Figure 4.18: The BBC-CNT Correlation function for Au+Au $\sqrt{s_{NN}}$ = 200 GeV for the 30-40% centrailty bin.

4.2.5 Systematic Errors

While v_n results for Au+Au $\sqrt{s_{NN}} = 200$ GeV have are referenced throughout this document, it is not the focus of this analysis and its values and systematic error analysis have been covered in numerous PHENIX publications.

What is covered, however, is v_n and its systematic errors for Cu+Cu $\sqrt{s_{NN}} = 200$ GeV using the long-ranged correlation method.

Trigger Efficiency

As discussed in section 3.3, the determination of the BBC trigger efficiency is subject to same amount of error. For Cu+Cu $\sqrt{s_{NN}} = 200$ GeV , the trigger efficiency was found to be 93±2%. If the trigger efficiency had infact been 91, then all of the events would normally have been in the 51% centrality might now be 49%. This means that each centrality bin will contain more peripheral events than if the trigger efficiency were 93% or 95%. Conversely, at 95%, centrality bins would contain more central collisions. Since the geometry of collision is highly dependent on the centrality, this is expected to have some impact on v_n

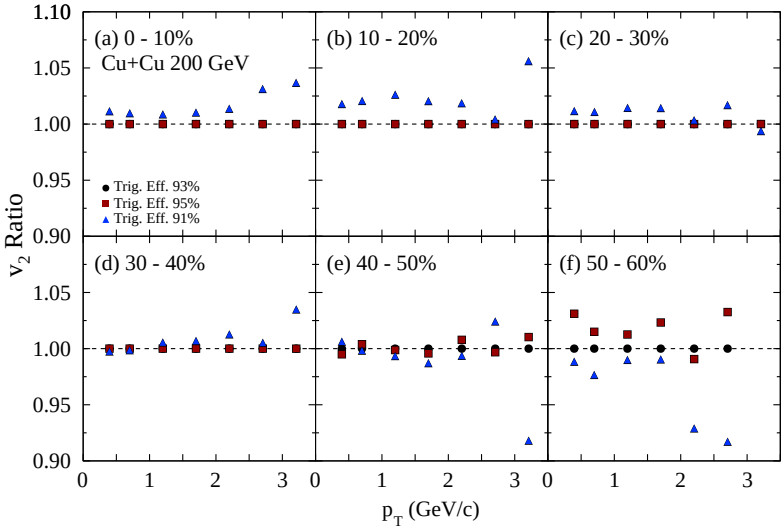

Figure 4.19: A systematic error check of the trigger efficiency on the Cu+Cu v_2.

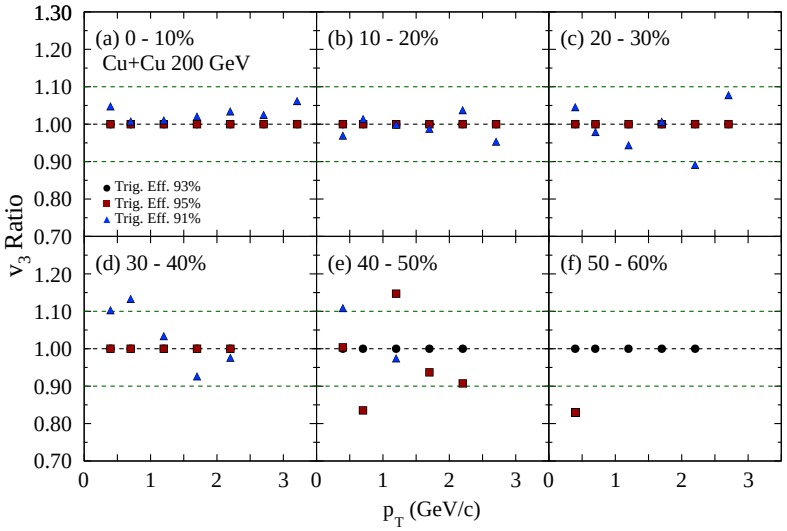

Figure 4.20: A systematic error check of the trigger efficiency on the Cu+Cu v_3.

What can be seen from figure 4.19 is that changing the a trigger efficiency of 95% has very little to no effect on v_2 until the 50-60% centrality bin in which it enhances the v_2 by about 3%. Decreasing the trigger efficiency to 91%, on the otherhand, has a much more pronounced effect. Each bin is slightly more peripheral than the 93% baseline and we see an enhancement which then diminishes as we appreach the higher centralities.

The effect on v_3 if fig. 4.20 is not as significant due to fluctuations in the initial state being largely independent of collision geometry. At around the 30-40% centrality bin, our ability to even measure v_3 begins to become questionable. Nothing after 40-50% is reported in the final results since very little useable data can be gleaned from the final results.

Binning of the z-vertex

As described earlier in the event mixing process, the event being analyzed is correlated with a separate, similar event. Like with the other systematic checks, we have arbitrarily decided on the degree to which one event is similar to another. For this analysis the z-vertex binning was 5 cm. Here we vary it to 5 ± 1 cm to see how much of an effect this decision had.

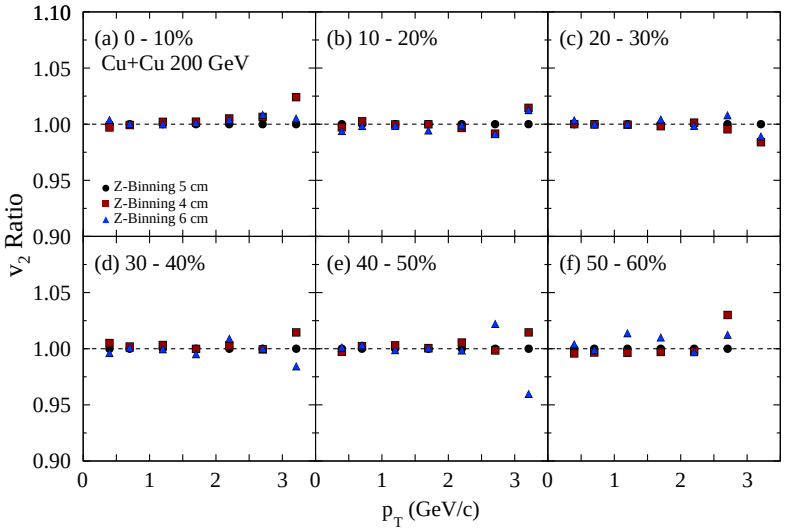

Figure 4.21: A systematic error check of the z-vertex binning on the Cu+Cu v_2.

The v_2 in figure 4.21 shows very little effect from varrying the bin size. In the vast majority of points, The effect is $< 1\%$. In the most periheral collions or the higher p_T points, the effect can be as large as 3$.

The v_3 ratio in figure 4.22 seems to be more highly affected being largely within 5%. A few points are even larger than that. Also like with the other systematics, we can see a breakdown of our measurement ability start in the 30-40% bin to be nearly lost at higher centralities.

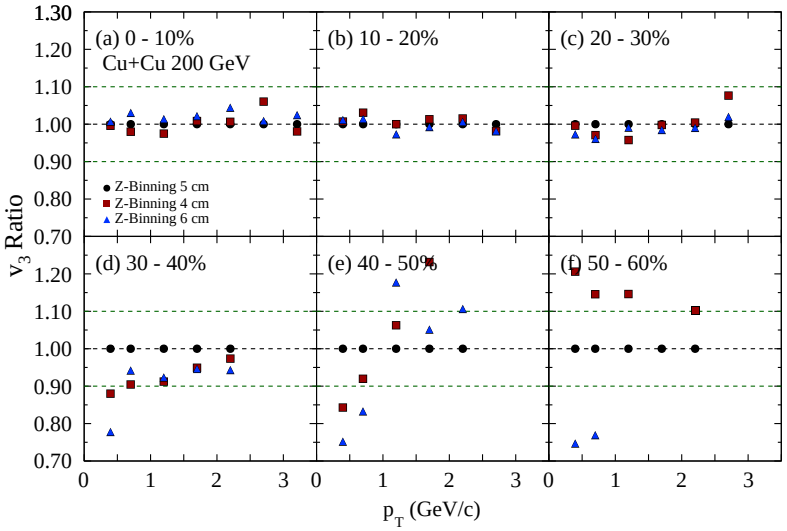

Figure 4.22: A systematic error check of the z-vertex binning on the Cu+Cu v_3.

PC3 Track Matching Cuts

In trying to keep with some of the parameters from [40], a default PC3 track matching cut of $\sigma_{\mathrm{PC3}} \leq 2.5$ was required. It's systematic error was estimated by varying it by 0.5σ.

Figure 4.23 shows that like with most measurements, this one is very well behaved in all but the highest p_T bin or the highest centrality bins. Nearly all of the points lie within 1-2% of the baseline value. Only a few points exceed this 2% threshold.

Even the v_3 values in figure 4.24 show little divergence outside of 5% of the baseline until the centrality climbs above 40%.

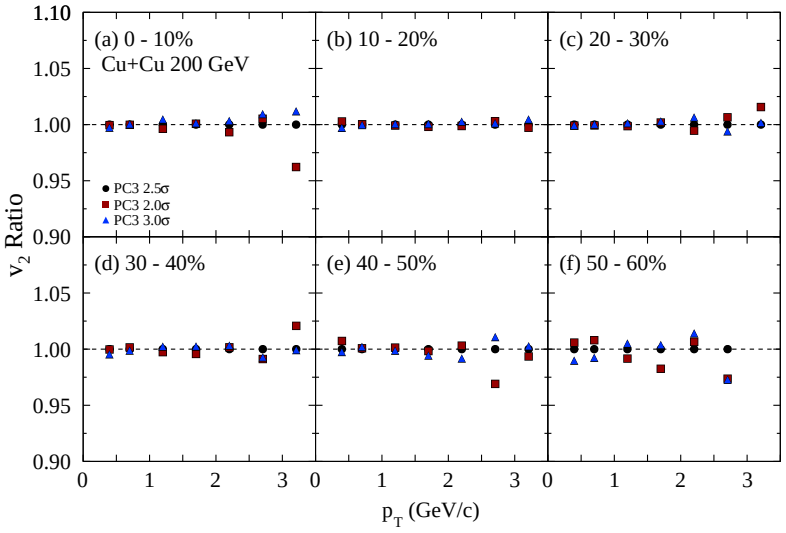

Figure 4.23: A systematic error check of the σ_{PC3} cut on the Cu+Cu v_2.

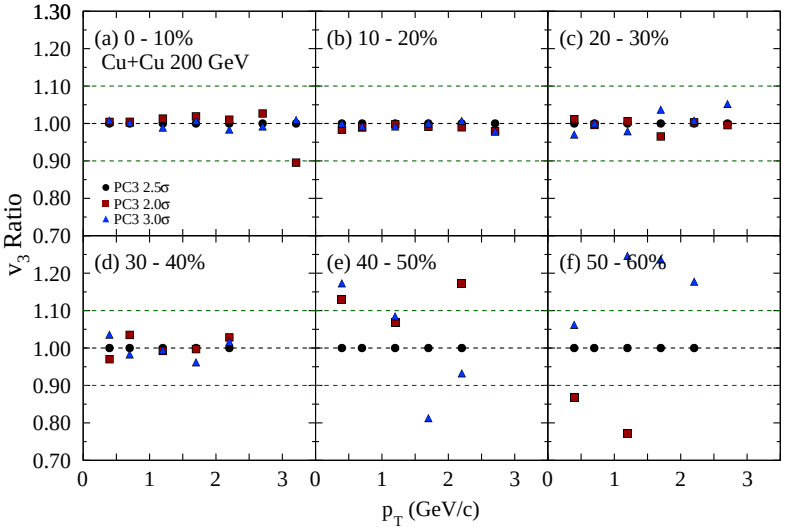

Figure 4.24: A systematic error check of the σ_{PC3} cut on the Cu+Cu v_3.

East vs. West Central Arms

The east and west arms of the PHENIX detector are not exactly identical. There are different detectors, different amounts of material, and different dead areas. For our default v_n we naturally use the full PHENIX acceptance but for the purposes of trying to find different sources of systematic error, we have run this analysis using correlation functions built from just the east or west arms of the detector.

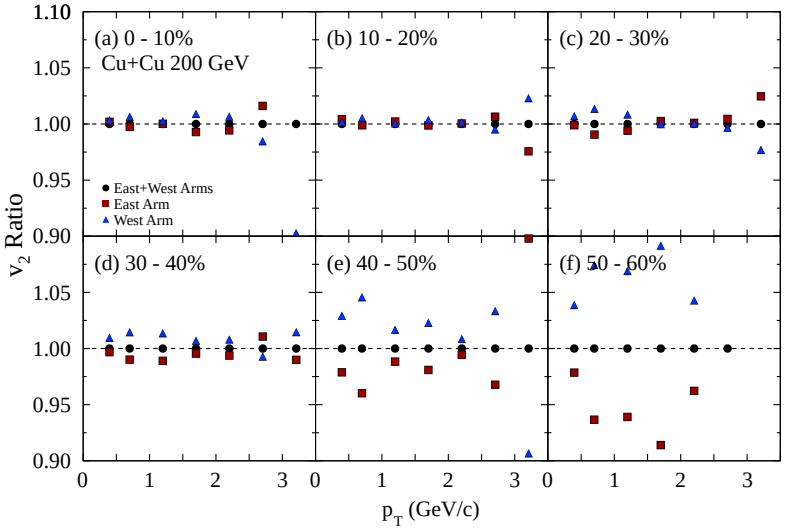

Figure 4.25: A systematic error check of the East and West central arms on the Cu+Cu v_2.

We can see in figure 4.25 that the difference between the east and west arms is the second largest contributor of systematic error. That being said, most of the points still lie within 2.5% of the baseline. One noteable difference, however, is that the systematic error contribution climbs 5% in the 40-50% centrality bin and goes even higer after that.

As expected, figure 4.26 show the systematic error as being much greater. With the exception of the last p_T datapoints, the error is about 10-20% and tends to be worse at lower p_T. After 40% in centrality, the error just becomes quite large.

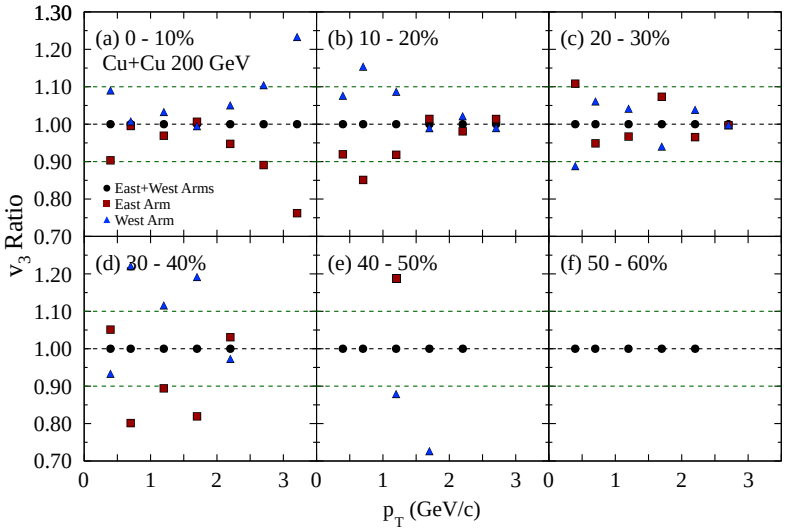

Figure 4.26: A systematic error check of the East and West central arms on the Cu+Cu v_3.

Systematic Error Summary

The final systematic error bands were added in quadrature separately for points above or below the baseline values. Tables 7.1-7.8 include the statistical and systematic errors as a percentage.

Chapter 5
Results

5.1 Comparison to Established Results

The results yielded by this analysis are in good agreement with established v_n values from both the PHENIX and STAR collaborations.

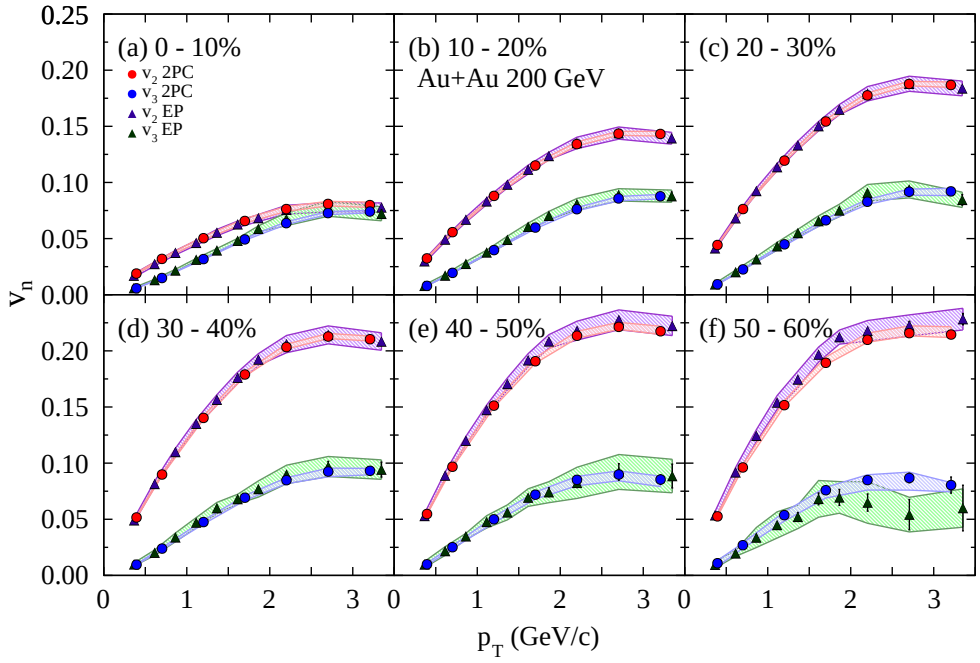

Figure 5.1: Au+Au v_n event plane vs. two-particle correlation results.

Figure 5.1 shows nearly complete overlap between the official PHENIX Au+Au $\sqrt{s_{NN}} = 200$ GeV results obtained obtained using the event plane method. In order to perform the various systematic checks listed in section 4.2.5, additional passes over the dataset would be required. Seeing as PHENIX already has official flow results for the event plane method [41] and the two-particle correlation method [42], this was merely a check to ensure that the the reproducibility of established results. The systematics shown

reflect differences in measured v_n between the east and west central arm detectors.

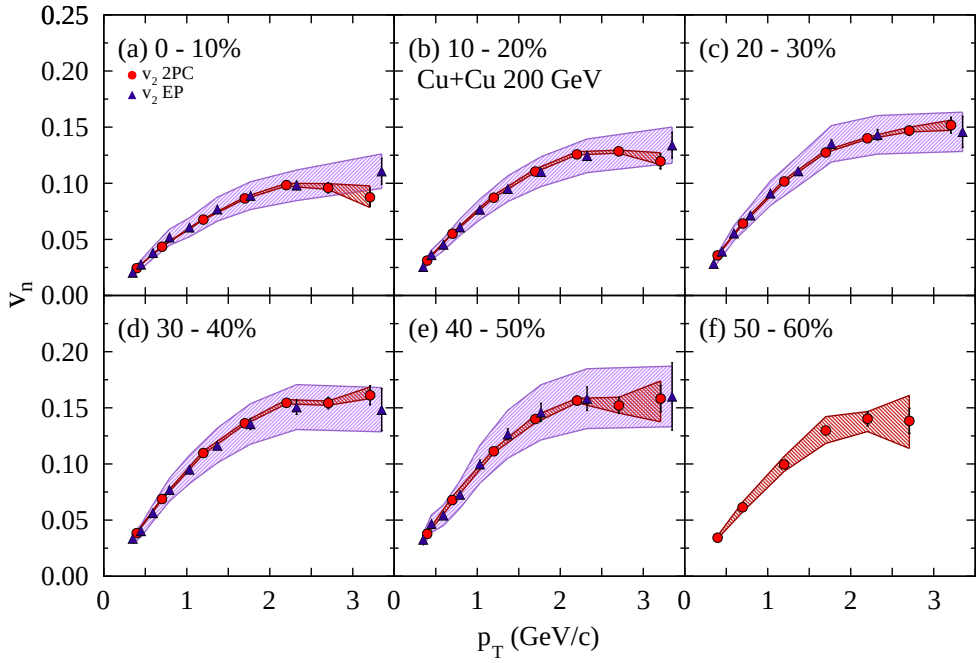

Figure 5.2: Cu+Cu v_n event plane vs. two-particle correlation results.

Within the PHENIX collaboration, there have been v_2 results produced using the event plane method for Cu+Cu $\sqrt{s_{NN}} = 200$ GeV [43], which is compared to the results in this analysis in figure 5.2. With the exception of the $3.25 \leq p_T < 3.5$ GeV/c data point in the 0-10% centrality bin, these points reside well within the large systematic errors of the event plane measurement.

The STAR v_2 event plane measurement for Cu+Cu $\sqrt{s_{NN}} = 200$ GeV [44] is also compared in figure 5.3. STAR estimates systematic error by measuring the difference in correlation functions between the Cu+Cu and p+p as measured by the Forward Time Projection Chamber (FTPC) and attributing this to non-flow correlations. This detector lies in a similar pseudorapidity range ($2.8 < |\eta| < 3.8$) as the PHENIX BBC. This difference is far more pronounced in their Time Projection Chamber (TPC) which straddles midrapidity much like the PHENIX central arms ($|\eta| < 1.0$). Systematic er-

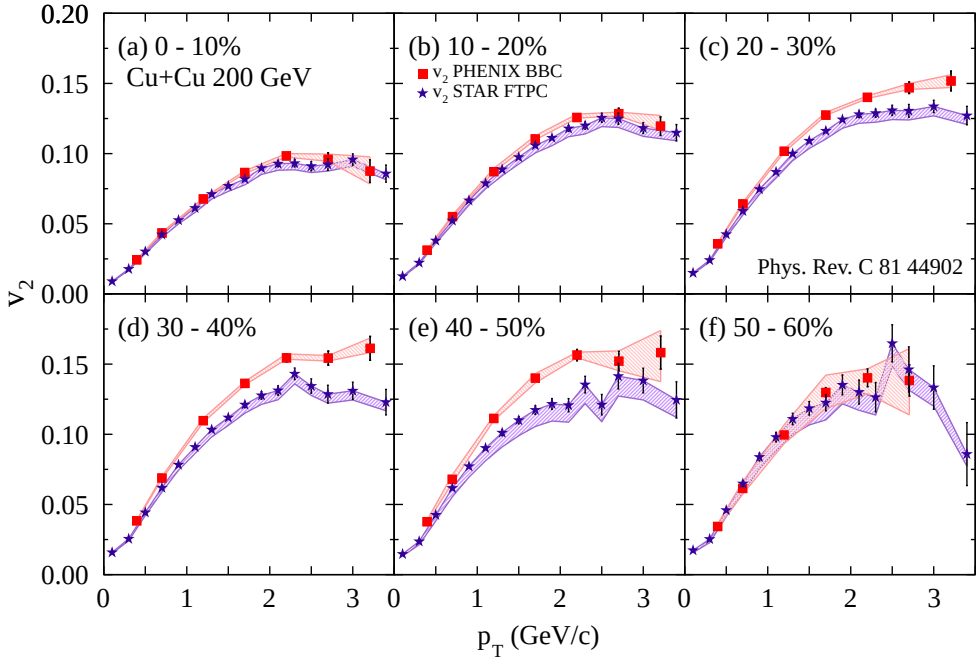

Figure 5.3: Cu+Cu v_n results compared to STAR.

rors were then simplified to -5% for centralities 0-40% and -10% for 40-60%. The 0-10%, 10-20% centrality binned results show a remarkable amount of overlap between the two vastly different detectors. The 20-30% centrality v_2 is lower by around 10% which then reaches about 20% in the 40-50% centrality bin. In the final 50-60% bin, both results align once again. The PHENIX author in the previous Cu+Cu comparison also noted this disparity. Directly reading the datapoints from the STAR Collaboration website, it appears that STAR is using 0.2 GeV/c p_T bins until 2.8 GeV/c where 0.4 GeV/c p_T bins are adopted. The p_T values which make up the x-coordinate appear to be the midpoint which lies to the right of the true mean p_T for the single particle distribution. That is to say, the STAR points should be shifted left slightly which would further improve the agreement by a small degree.

5.2 Elliptic and Triangular Flow Results for Cu+Cu $\sqrt{s_{NN}} = 200$ GeV

The final v_n results for Cu+Cu $\sqrt{s_{NN}} = 200$ GeV are presented 10% centrality bins in figure 5.4 and 5% bins in figure 5.5.

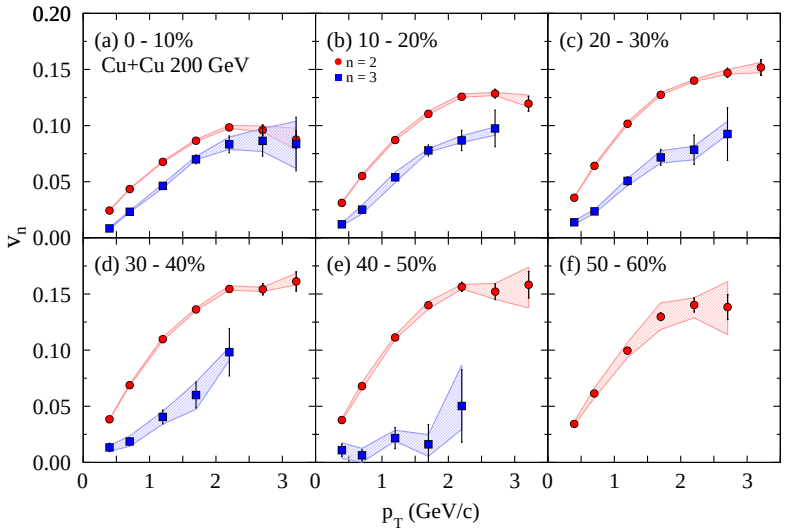

Figure 5.4: Final Cu+Cu $\sqrt{s_{NN}} = 200$ GeV v_n results as a function of p_T in 10% centrality bins.

Despite the fact that Cu+Cu is so much smaller that Au+Au, it still has very strong flow signals, v_2 and v_3. The v_3 magnitude is comparable to the v_2 for very central collision (0-10%) where the fireball that is left is largely isotropic and therefore does not produce much of an elliptic flow signal. The triangular flow in this symmetric collision system, on the otherhand, is primarily driven by fluctuations which are present at all centralities.

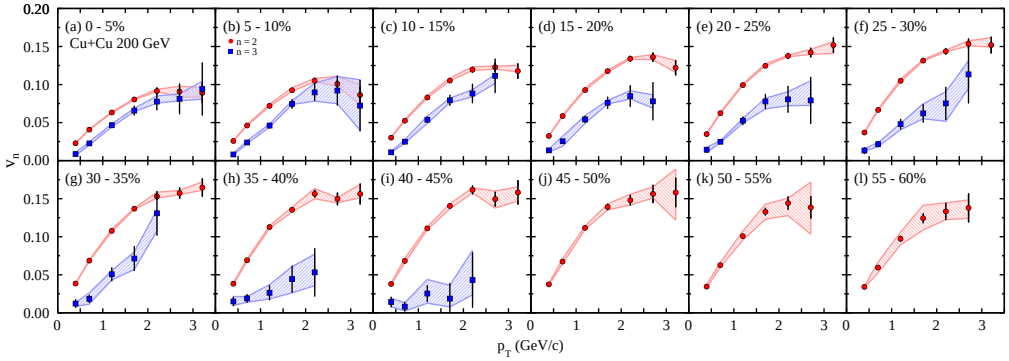

Figure 5.5: Final Cu+Cu $\sqrt{s_{NN}} = 200$ GeV v_n results as a function of p_T in 5% centrality bins.

5.3 Comparisons between Au+Au and Cu+Cu

5.3.1 Centrality Dependence

One can alternatively look at $v_n(\text{centrality}, p_T)$ as a function of centrality for different p_T ranges as in figure 5.6.

The most obvious difference between the two systems is that at larger p_T values, the v_2 for Au+Au keeps rising, peaking at about 0.23 between 40-50% centrality, whereas Cu+Cu saturates much earlier than that barely getting above 0.16. Additionally, for any given p_T bin, there is not a tremendous change from one centrality to another. This is the reason that most of the v_2 curves look very similar to each other in figures 5.5 and 5.4. Another noticable difference is that at from 0-10% centrality, the elliptic flow for Cu+Cu is greater than that of Au+Au. Despite being so dissimilar in size, the triangular flow signal seen is nearly the same in both systems. While the Au+Au v_3 shows a slight centrality dependence, the Cu+Cu v_3 shows a downward trend.

These departures can better explained when combining the centrality dependent values obtained from the Glauber Monte Carlo.

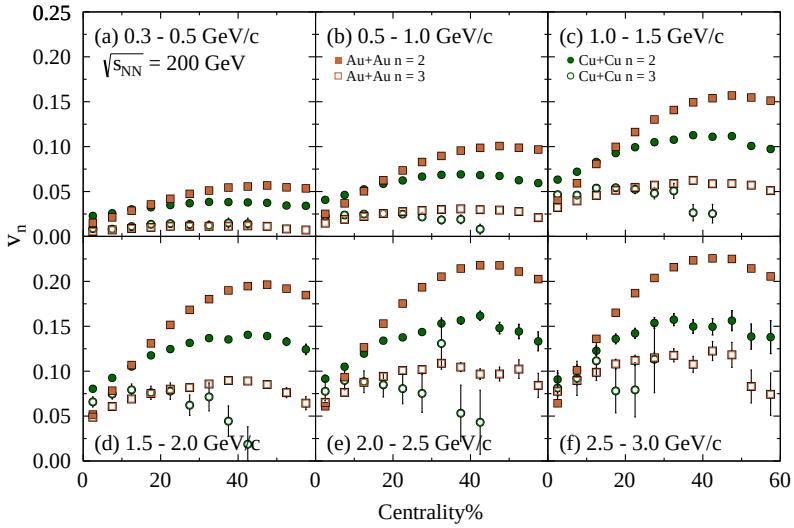

Figure 5.6: Elliptic and triangular flow as a function of centrality.

5.3.2 N_{part} Dependence

Comparing results for in terms of centrality can be problematic because ^{197}Au has so many more nucleons than ^{63}Cu. In a midcentral 20-25% central collision, a Au+Au collision may have around 180 nucleons participating whereas Cu+Cu will have only 60. Figure 5.7 does a better job of comparing the two collision systems using N_{part} instead. With centrality defined as it is, the right-hand side of each data series represents a central collision where nucleon overlap is maximal. As the collision becomes more peripheral, the shape of the interaction region becomes more elliptical leading to greater v_2 values. Once N_{part} falls below a certain point, the dominance of geometry induced flow is lessened by competing effects like jets or fluctuations in the initial state configuration of the nuclei. The curves for Cu+Cu resemble that of Au+Au but its maximum N_{part} is only 126. It can be seen here that while v_3 seemed to differ considerable when plotted as a function of centrality, these regions happen at a lower N_{part} in Cu+Cu.

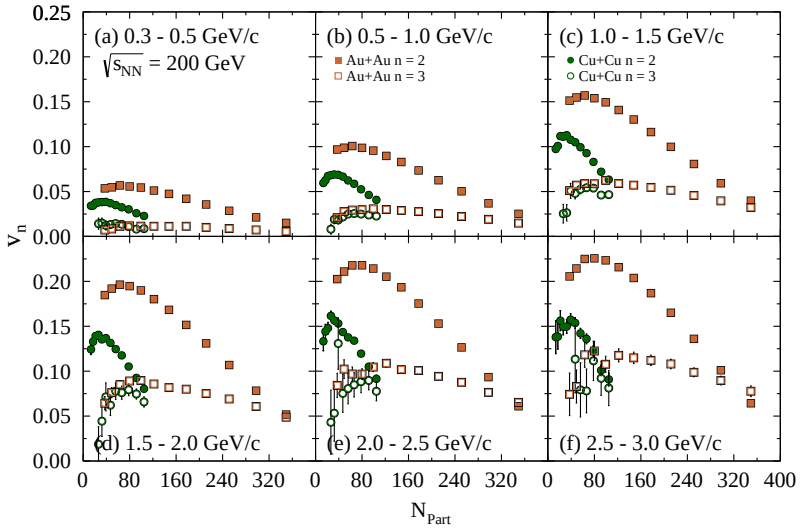

Figure 5.7: Elliptic and triangular flow as a function of N_{part}.

5.3.3 Eccentricity Dependence

Considering the number of participating nucleons does improve the comparison between the two systems. At any given N_{part}, however, there will be great differences in the average eccentricities. Figure 5.8 is the result of dividing the v_n by its corresponding eccentricity ϵ_n. The eccentricity scaling bridges the gap between the Cu+Cu and Au+Au collision systems. Two distict branches corresponding to each harmonic can be seen. These results also make clear that even with a very low number of participating nucleons, flow still develops [12]. PHOBOS has also found measuring v_2 that collisions at $\sqrt{s_{NN}} = 62.4$ GeV will also produce points that overlap with these [45].

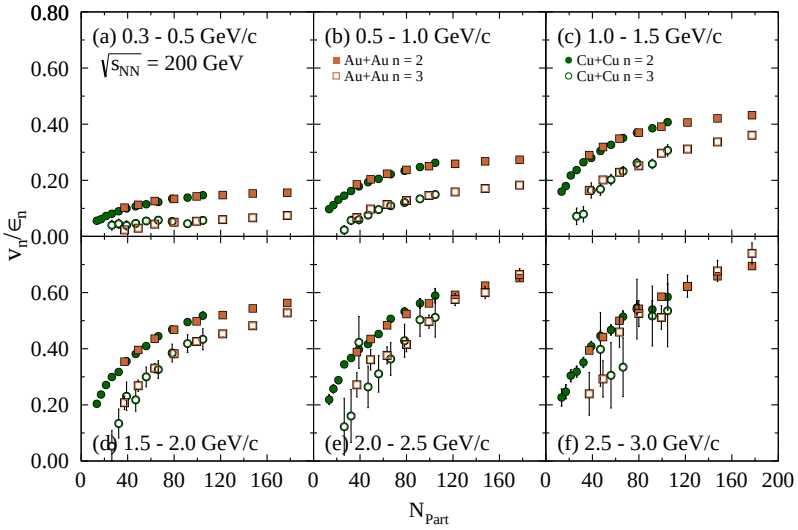

Figure 5.8: Elliptic and triangular flow scaled by ϵ_n as a function of $N_{\rm part}$.

5.3.4 $N_{\rm Part}^{1/3}$ Dependence

In an effort to further scale by system size, the analysis in ref. [43] additionally scales v_2 by $N_{\rm Part}^{1/3}$ due to an observed system size dependence seen in a Hanbury-Brown-Twiss (HBT) analysis [46].

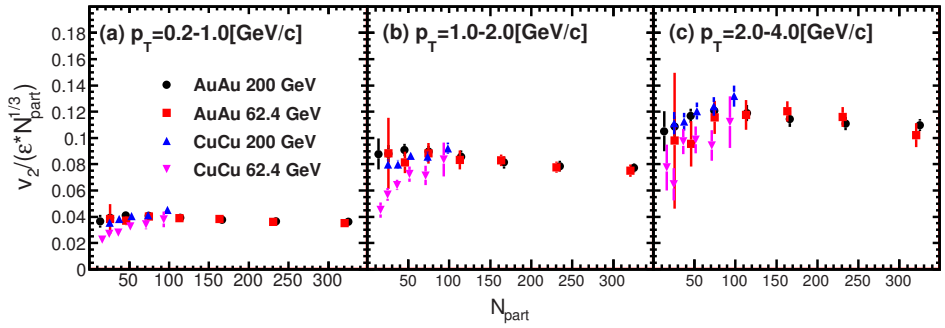

Figure 5.9: The elliptic flow scaled by ϵ_2 and $N_{\rm Part}^{1/3}$ as a function of $N_{\rm part}$ for Cu+Cu and Au+Au collisions at $\sqrt{s_{NN}} = 62.4$ and 200 GeV.

This scaling in figure 5.9 does a fairly decent job of parameterizing the curve seen with just the eccentricity scaling at least in the case of Au+Au

collisions. This scaling does not seem to work as well for Cu+Cu and does quite poorly at $\sqrt{s_{NN}} = 62.4$ GeV at low N_{part}.

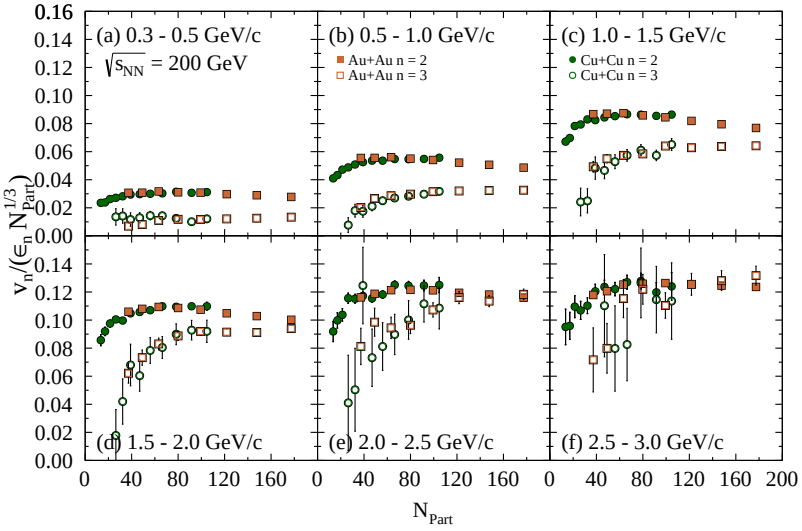

Figure 5.10: Elliptic and triangular flow scaled by ϵ_n and $N_{\text{Part}}^{1/3}$ as a function of N_{part}.

Adding in v_3 and restricting ourselves to $\sqrt{s_{NN}} = 200$ GeV in figure 5.10, it can be more clearly seen that Au+Au and Cu+Cu still line up decently. The curves produced by v_2 takes a dive at $N_{\text{part}} < 40$. While the Au+Au seems more resistant to diving for v_2, the v_3 curves in the higher p_T bins begin the decline at a higher N_{part} for both Cu+Cu and Au+Au.

Chapter 6
Conclusion

The anisotropic flow of particles has long been recognized as an important indicator for the presence of the quark-gluon plasma. Throughout the years there have been many studies of the even-numbered v_n terms due to the assumption that a smooth profile and symmetry would prohibit odd-numbered terms. PHENIX has published Au+Au v_2 and v_3 results however there has not yet been a v_3 result for Cu+Cu. The event plane method has been a favorite method for studying v_n but using a long-ranged, two-particle correlation method works just as well if not better. It tends to have smaller systematic errors and can be performed in one pass over the data because the event plane determination step need not be performed.

The Cu+Cu $\sqrt{s_{NN}} = 200$ GeV v_n was explored as a function of both p_T and centrality. The v_2 signal was very strong even for such a small system though it was quickly outpaced by Au+Au. The result from v_3 showed very good agreement between the two systems which further supports the idea that fluctuations in the initial state configuration of the nuclei are the main driving force behind it.

Unfortunately this initial state configuration is not experimentally known so one must use models as a starting point. We used the Glauber model to obtain certain quantities: the number of participating nucleons (N_{part}), the number of collisions (N_{coll}), the impact parameter (b), and the eccentricities (ϵ_n). Combining N_{part} with a negative binomial distribution to emulate the detector response of the BBC, we are able to correlate the model's centrality bins with the centrality bins of our data. Centrality is useful but not the perfect way to compare different collision systems so we have also explored v_n in terms of N_{part} as well as scaling by the eccentricity as well as $N_{\text{Part}}^{1/3}$, an analogue for the system size suggested by HBT studies. By doing this common properties can be found once the geometric differences are removed.

The internal workings of the quark-gluon plasma is, at the moment, unknown. We can only build models based off of the physical principles that we've learned and compare them to the experimental data. Figure 6.1 from [41] does exactly that. When we were only measuring v_2, different models with different parameters like sheer viscosity could reasonably describe what we saw. Upon measuring v_3, it became clear that some models per-

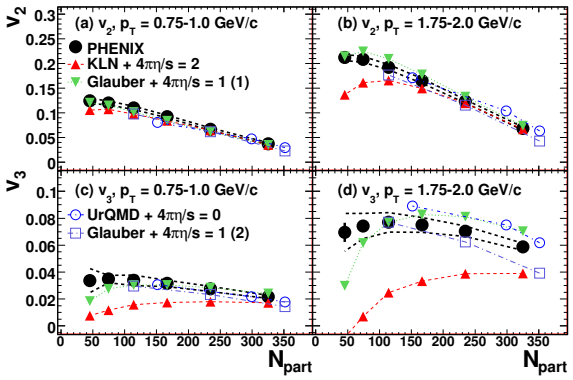

Figure 6.1: A comparison of different models across v_2 and v_3 for Au+Au $\sqrt{s_{NN}}$ = 200 GeV .

formed better than others. It is far from perfect but a greater variety of measurements can give theorists the constraints that their models need.

The next logical step is to study the flow in terms of identified particles like π, K, p. In 2005 there were fewer detector systems that could perform particle identification. It was possible to measure them for v_2 despite the loss of statstics. For v_3, however, more statistics would be desired in order to make a useful measurement. Other energies could also be explored. We took 200 GeV data for 7.8 weeks, 62.4 GeV data for 12 days, and 22.4 GeV data for 2 days. Lower energies have lower multiplicities and so it would be desireable to have much longer runs. Alternatively, we could study different nuclei like deformed uranium nuclei. Another collision system that is of particular interest is that of Cu+Au. Copper, being significantly smaller, would impact the gold nucleus like a cookie cutter through dough. From the initial state distributions, a midcentral collision would produce more binary collsisions towards the center of the Au making an azimuthally asymmetric fireball.

The two-particle correlation method is robust and can be applied not only azimuthally but also in terms of pseudorapidity. If one wants to see how photons correlate with protons, this method can work there. Honestly, wherever particles share some sort of correlation, this method will be able to pick up on it.

Chapter 7
Appendix

This chapter contains data tables of select plots.

	p_T Bin (GeV/c)	$\langle p_T \rangle$ (GeV/c)	v_3	±stat%	+sys%	-sys%
Cent 0-10%	0.3-0.5	0.396153	0.0243464	1.82432	1.27442	0.401721
	0.5-1	0.701684	0.0434843	0.904648	1.17122	0.272251
	1-1.5	1.19985	0.0676682	1.06727	1.04346	0.373393
	1.5-2	1.69886	0.086521	1.55911	1.40381	0.719289
	2-2.5	2.19977	0.0983666	2.56217	1.69027	0.882372
	2.5-3	2.70287	0.0959873	4.78996	3.83466	1.53137
	3-3.5	3.2069	0.0875149	9.18593	11.6203	10.4267
Cent 10-20%	0.3-0.5	0.396305	0.0311446	1.21707	1.87127	0.716571
	0.5-1	0.701624	0.0551101	0.608103	2.15022	0.193322
	1-1.5	1.19984	0.0871532	0.706567	2.63479	0.162667
	1.5-2	1.69932	0.110464	1.03839	2.08896	0.594831
	2-2.5	2.20068	0.125738	1.69102	1.88902	0.367374
	2.5-3	2.7039	0.128487	2.98163	0.839489	1.30172
	3-3.5	3.20755	0.119559	5.53207	6.38552	2.45065
Cent 20-30%	0.3-0.5	0.396311	0.0357719	1.13612	1.40958	0.161325
	0.5-1	0.70097	0.0641541	0.562128	1.74402	0.949227
	1-1.5	1.1995	0.101633	0.656734	1.68549	0.614704
	1.5-2	1.69958	0.127411	0.977117	1.55884	0.177389
	2-2.5	2.20121	0.14006	1.63937	0.747787	0.556838
	2.5-3	2.70459	0.146946	2.78747	2.03771	0.819398
	3-3.5	3.20815	0.15177	4.6122	2.92126	3.06675

Table 7.1: Cu+Cu $\sqrt{s_{_{NN}}} = 200$ GeV v_3 data points for centralities 0-30% in 10% centrality bins.

	p_T Bin (GeV/c)	$\langle p_T \rangle$ (GeV/c)	v_3	±stat%	+sys%	-sys%
Cent 30-40%	0.3-0.5	0.396271	0.0383877	1.29697	1.08756	0.717883
	0.5-1	0.7004	0.0688034	0.644437	1.48434	1.00799
	1-1.5	1.19906	0.109737	0.752984	1.52488	1.13025
	1.5-2	1.69968	0.136236	1.13347	1.01315	0.7801
	2-2.5	2.20175	0.154468	1.83442	1.82053	0.628839
	2.5-3	2.70525	0.154266	3.25377	1.18881	1.34797
	3-3.5	3.20922	0.161215	5.27815	4.55566	1.85378
Cent 40-50%	0.3-0.5	0.396131	0.0377273	1.81556	3.08392	2.21217
	0.5-1	0.699186	0.0678964	0.906052	4.61244	3.98509
	1-1.5	1.19834	0.111275	1.04341	1.71201	1.35653
	1.5-2	1.69974	0.139997	1.55782	2.30028	2.41627
	2-2.5	2.20239	0.156428	2.55288	1.32215	1.19817
	2.5-3	2.70604	0.152102	4.62223	4.81213	4.48452
	3-3.5	3.20958	0.158214	7.46947	9.95828	13.0666
Cent 50-60%	0.3-0.5	0.395918	0.0342948	3.0589	5.02167	2.67976
	0.5-1	0.69747	0.061412	1.55304	7.63436	6.80942
	1-1.5	1.19735	0.0995346	1.84167	7.17645	6.24517
	1.5-2	1.69943	0.129778	2.67321	9.5211	8.83211
	2-2.5	2.20252	0.140238	4.52509	4.55997	8.10663
	2.5-3	2.7063	0.138349	8.04868	16.4172	17.7481

Table 7.2: Cu+Cu $\sqrt{s_{NN}} = 200$ GeV v_3 data points for centralities 30-60% in 10% centrality bins.

	p_T Bin (GeV/c)	$\langle p_T \rangle$ (GeV/c)	v_2	±stat%	+sys%	-sys%
Cent 0-10%	0.3-0.5	0.396153	0.00840858	15.6808	10.3051	9.66569
	0.5-1	0.701684	0.0232383	5.02586	3.26247	2.06961
	1-1.5	1.19985	0.0463124	4.62686	3.93784	4.1194
	1.5-2	1.69886	0.0699544	5.71864	3.78452	0.500477
	2-2.5	2.19977	0.0833538	8.96948	7.64552	5.49396
	2.5-3	2.70287	0.0864014	15.7867	12.6503	10.9468
	3-3.5	3.2069	0.0835749	28.5331	24.286	26.0493
Cent 10-20%	0.3-0.5	0.396305	0.0120645	13.3973	7.75068	8.76193
	0.5-1	0.701624	0.0251507	5.68306	15.8303	14.9533
	1-1.5	1.19984	0.0539712	4.86396	8.69983	8.6472
	1.5-2	1.69932	0.0779154	6.27296	1.92063	1.94208
	2-2.5	2.20068	0.0868124	10.44	4.70839	2.15876
	2.5-3	2.7039	0.0974478	16.7572	1.38464	6.16721
Cent 20-30%	0.3-0.5	0.396311	0.0139032	16.7838	11.8088	11.8638
	0.5-1	0.70097	0.0236016	8.77574	6.11101	7.38147
	1-1.5	1.1995	0.0507193	7.55559	4.21814	8.0679
	1.5-2	1.69958	0.0716857	9.96683	8.24548	7.05768
	2-2.5	2.20121	0.0785	16.791	3.99577	11.4019
	2.5-3	2.70459	0.0925294	25.4203	12.2709	0.557408
Cent 30-40%	0.3-0.5	0.396271	0.0133579	27.8114	12.0717	26.3006
	0.5-1	0.7004	0.0186319	17.7651	26.0397	22.8648
	1-1.5	1.19906	0.0404858	15.2333	12.0893	15.7774
	1.5-2	1.69968	0.0600222	19.1958	19.1973	21.2115
	2-2.5	2.20175	0.0981884	21.5417	4.52598	7.22969

Table 7.3: Cu+Cu $\sqrt{s_{_{NN}}} = 200$ GeV v_3 data points for centralities 0-40% in 10% centrality bins.

	p_T Bin (GeV/c)	$\langle p_T \rangle$ (GeV/c)	v_3	±stat%	+sys%	-sys%
Cent 0-5%	0.3-0.5	0.396108	0.0228347	3.03996	1.73795	0.928905
	0.5-1	0.701709	0.0407608	1.50899	1.40576	0.340082
	1-1.5	1.19987	0.0632637	1.78421	1.37731	0.906681
	1.5-2	1.69872	0.0804054	2.62351	1.25294	0.513837
	2-2.5	2.19956	0.0915199	4.31563	2.3336	0.659071
	2.5-3	2.70254	0.0907953	7.9611	7.6235	7.5177
	3-3.5	3.20688	0.088994	14.2488	8.14429	6.37799
Cent 5-10%	0.3-0.5	0.396195	0.0258569	2.19821	2.54129	0.286764
	0.5-1	0.701661	0.0461894	1.08944	2.52492	0.446803
	1-1.5	1.19984	0.0720457	1.2828	2.85662	0.742025
	1.5-2	1.69899	0.0925337	1.86461	3.52587	1.72581
	2-2.5	2.19995	0.104979	3.06444	2.94921	1.31276
	2.5-3	2.70317	0.10092	5.79769	9.86547	3.07949
	3-3.5	3.20692	0.0863327	11.8131	15.2003	14.5163
Cent 10-15%	0.3-0.5	0.396295	0.0301967	1.76924	2.04549	0.756761
	0.5-1	0.701714	0.0524804	0.899744	2.80779	0.12041
	1-1.5	1.19989	0.0829692	1.04466	3.01898	0.564717
	1.5-2	1.69925	0.105166	1.53539	3.13956	0.160409
	2-2.5	2.2005	0.119536	2.50715	3.16999	0.97804
	2.5-3	2.70369	0.122749	4.40986	1.23095	1.95725
	3-3.5	3.20748	0.117734	7.95675	6.24257	0.854843
Cent 15-20%	0.3-0.5	0.396318	0.0324511	1.64351	1.85684	0.723756
	0.5-1	0.701516	0.0586155	0.804774	1.46645	0.519919
	1-1.5	1.19979	0.09278	0.935466	2.42248	0.423657
	1.5-2	1.6994	0.117583	1.37473	1.02688	1.20239
	2-2.5	2.20091	0.133964	2.23312	1.15354	0.466059
	2.5-3	2.70416	0.135975	3.95187	2.52093	2.52653
	3-3.5	3.20763	0.122117	7.57444	7.6224	5.04764

Table 7.4: Cu+Cu $\sqrt{s_{_{NN}}} = 200$ GeV v_3 data points for centralities 0-20% in 5% centrality bins.

	p_T Bin (GeV/c)	$\langle p_T \rangle$ (GeV/c)	v_3	±stat%	+sys%	-sys%
Cent 20-25%	0.3-0.5	0.396326	0.0349044	1.5863	2.18787	1.08816
	0.5-1	0.701168	0.0623695	0.786736	1.77391	0.880795
	1-1.5	1.19962	0.0993156	0.912507	1.63003	0.315226
	1.5-2	1.69955	0.124581	1.35596	2.15174	0.0710045
	2-2.5	2.20113	0.137628	2.26566	0.555659	0.780194
	2.5-3	2.70426	0.142108	3.9204	2.98301	1.82677
	3-3.5	3.20798	0.151788	6.28536	3.05831	7.09943
Cent 25-30%	0.3-0.5	0.396293	0.0369715	1.61016	1.55249	0.996648
	0.5-1	0.700732	0.0666394	0.793989	1.73841	1.07024
	1-1.5	1.19937	0.10494	0.935723	1.98051	1.26458
	1.5-2	1.69962	0.131477	1.39425	1.01331	0.355886
	2-2.5	2.20131	0.143571	2.35226	1.22289	0.35297
	2.5-3	2.70498	0.153673	3.91253	2.4786	2.00879
	3-3.5	3.20836	0.151886	6.74711	6.3904	1.66974
Cent 30-35%	0.3-0.5	0.39629	0.0384606	1.71466	1.27595	1.30845
	0.5-1	0.700575	0.0686195	0.854873	1.02667	0.549708
	1-1.5	1.19918	0.107699	1.01319	2.11486	1.09466
	1.5-2	1.69963	0.136835	1.48905	0.412337	0.548967
	2-2.5	2.20161	0.153091	2.4447	3.53259	1.57715
	2.5-3	2.70494	0.157366	4.2181	2.21028	1.25061
	3-3.5	3.20912	0.164654	6.83912	4.60399	2.14196
Cent 35-40%	0.3-0.5	0.396247	0.038282	1.97823	3.24564	2.70233
	0.5-1	0.700187	0.0690711	0.97798	2.19209	1.7737
	1-1.5	1.19891	0.112733	1.1194	1.57004	1.64823
	1.5-2	1.69975	0.135357	1.74423	2.60523	2.01716
	2-2.5	2.20193	0.156492	2.76471	4.42879	4.2416
	2.5-3	2.70564	0.149735	5.11009	1.00123	3.40771
	3-3.5	3.20934	0.156226	8.29469	8.18502	3.21721

Table 7.5: Cu+Cu $\sqrt{s_{NN}} = 200$ GeV v_3 data points for centralities 20-40% in 5% centrality bins.

	p_T Bin (GeV/c)	$\langle p_T \rangle$ (GeV/c)	v_3	±stat%	+sys%	-sys%
Cent 40-45%	0.3-0.5	0.39617	0.037928	2.33551	2.95361	1.80458
	0.5-1	0.699535	0.0682535	1.16298	4.43684	3.9501
	1-1.5	1.19851	0.111008	1.3452	1.73308	1.46084
	1.5-2	1.69975	0.140495	1.99368	1.98307	2.74098
	2-2.5	2.20238	0.161615	3.17414	1.61536	2.42809
	2.5-3	2.70601	0.149493	6.04647	7.08553	7.86693
	3-3.5	3.20941	0.158251	9.61563	4.55486	7.2126
Cent 45-50%	0.3-0.5	0.396082	0.0374254	2.88487	3.62512	3.263
	0.5-1	0.69875	0.0673386	1.44454	5.16774	4.06927
	1-1.5	1.19811	0.111685	1.65143	2.00593	1.92481
	1.5-2	1.69972	0.139146	2.49485	2.90579	2.82559
	2-2.5	2.20241	0.147986	4.29412	5.26616	4.27393
	2.5-3	2.70608	0.156278	7.1503	5.97291	3.4611
	3-3.5	3.20979	0.158144	11.8511	19.3505	22.9693
Cent 50-55%	0.3-0.5	0.395976	0.0344201	3.86057	8.22386	5.01249
	0.5-1	0.697902	0.0625876	1.925	5.31083	4.25237
	1-1.5	1.19757	0.10077	2.28875	6.35305	5.28736
	1.5-2	1.69952	0.132873	3.27959	7.43533	7.44633
	2-2.5	2.20258	0.144174	5.52594	4.4606	11.328
	2.5-3	2.7063	0.138526	10.0997	23.9876	25.4685
Cent 55-60%	0.3-0.5	0.395845	0.03412	5.01394	2.49551	3.51748
	0.5-1	0.696914	0.0594383	2.62744	11.9181	11.5825
	1-1.5	1.19706	0.0973636	3.10156	8.8108	8.57512
	1.5-2	1.69929	0.124269	4.61079	13.8006	12.4438
	2-2.5	2.20244	0.133233	7.8725	8.50976	8.1762
	2.5-3	2.70631	0.13794	13.3279	7.55397	9.93576

Table 7.6: Cu+Cu $\sqrt{s_{_{NN}}} = 200$ GeV v_3 data points for centralities 40-60% in 5% centrality bins.

	p_T Bin (GeV/c)	$\langle p_T \rangle$ (GeV/c)	v_2	±stat%	+sys%	-sys%
Cent 0-5%	0.3-0.5	0.396108	0.00867664	21.5812	20.4	22.7424
	0.5-1	0.701709	0.0226697	7.3195	8.94302	9.52814
	1-1.5	1.19987	0.0465335	6.53933	3.69992	4.50193
	1.5-2	1.69872	0.0657814	8.6404	4.32608	2.12096
	2-2.5	2.19956	0.0776185	13.715	9.33095	2.62818
	2.5-3	2.70254	0.0812053	23.9929	8.2827	3.16513
	3-3.5	3.20688	0.0941727	36.2899	10.587	14.2423
Cent 5-10%	0.3-0.5	0.396195	0.00811083	22.8068	18.3639	5.32463
	0.5-1	0.701661	0.0238735	6.86095	9.04831	7.06034
	1-1.5	1.19984	0.0460766	6.52512	4.509	3.98523
	1.5-2	1.69899	0.0745917	7.52147	5.39105	0.903065
	2-2.5	2.19995	0.0896765	11.6681	13.5657	12.8467
	2.5-3	2.70317	0.0920738	20.6706	19.927	18.662
	3-3.5	3.20692	0.0722803	45.8928	47.0639	44.7888
Cent 10-15%	0.3-0.5	0.396295	0.0110027	19.667	8.272	5.30521
	0.5-1	0.701714	0.0249	7.68252	10.81	7.64275
	1-1.5	1.19989	0.0538119	6.52198	8.61199	8.49108
	1.5-2	1.69925	0.0792583	8.24529	3.52777	4.12194
	2-2.5	2.2005	0.0882471	13.7491	5.69094	5.02345
	2.5-3	2.70369	0.111531	19.65	1.33506	8.95837
Cent 15-20%	0.3-0.5	0.396318	0.0135449	17.8918	10.3204	15.6077
	0.5-1	0.701516	0.0255002	8.40762	25.9941	25.7616
	1-1.5	1.19979	0.0541961	7.2753	9.15344	9.2912
	1.5-2	1.6994	0.076033	9.65386	4.12383	2.20191
	2-2.5	2.20091	0.0848138	16.023	8.28934	4.3772
	2.5-3	2.70416	0.0780115	31.2882	10.8451	11.5314

Table 7.7: Cu+Cu $\sqrt{s_{NN}} = 200$ GeV v_3 data points for centralities 0-20% in 5% centrality bins.

	p_T Bin (GeV/c)	$\langle p_T \rangle$ (GeV/c)	v_2	±stat%	+sys%	-sys%
Cent 20-25%	0.3-0.5	0.396326	0.0143244	20.9648	21.4855	24.5869
	0.5-1	0.701168	0.0248508	10.7124	5.63975	5.44629
	1-1.5	1.19962	0.0524809	9.36509	5.42172	5.99016
	1.5-2	1.69955	0.0777605	11.7765	5.44068	12.5442
	2-2.5	2.20113	0.080585	20.9822	12.4277	10.4108
	2.5-3	2.70426	0.0791915	38.1589	32.436	8.35466
Cent 25-30%	0.3-0.5	0.396293	0.0132698	27.9663	19.2535	7.03072
	0.5-1	0.700732	0.0216779	15.2206	9.14778	14.4533
	1-1.5	1.19937	0.0479648	12.7629	2.17509	15.3071
	1.5-2	1.69962	0.0621218	18.3886	20.2259	11.388
	2-2.5	2.20131	0.0752594	27.9706	20.2895	31.3119
	2.5-3	2.70498	0.113374	33.0685	15.6705	16.1415
Cent 30-35%	0.3-0.5	0.39629	0.0121992	41.3566	9.27666	31.6994
	0.5-1	0.700575	0.0183993	24.4015	42.7846	37.3231
	1-1.5	1.19918	0.0507324	16.4586	8.96241	14.6954
	1.5-2	1.69963	0.0713715	21.8377	12.3987	20.1544
	2-2.5	2.20161	0.130796	21.8981	3.35652	17.6736
Cent 35-40%	0.3-0.5	0.396247	0.0149609	36.5278	44.042	35.4595
	0.5-1	0.700187	0.0189843	25.6888	11.634	26.8959
	1-1.5	1.19891	0.0263471	34.5757	40.6584	30.5558
	1.5-2	1.69975	0.0443362	38.4291	36.8839	40.6863
	2-2.5	2.20193	0.0531957	58.7163	45.0971	32.7175

Table 7.8: Cu+Cu $\sqrt{s_{NN}} = 200$ GeV v_3 data points for centralities 0-20% in 5% centrality bins.

	Cu+Cu 200 GeV			Au+Au 200 GeV		
Centrality	N_{part}	ϵ_2	ϵ_3	N_{part}	ϵ_2	ϵ_3
0-5%	104.725	0.155335	0.15172	349.365	0.0834944	0.0777613
5-10%	91.5946	0.186914	0.17828	297.678	0.128526	0.0986664
10-15%	78.3293	0.22451	0.206045	251.326	0.178669	0.117015
15-20%	66.3914	0.264462	0.23335	211.651	0.225849	0.134063
20-25%	56.0001	0.304275	0.259495	177.363	0.269094	0.151482
25-30%	46.9287	0.34471	0.285146	147.682	0.309614	0.169596
30-35%	39.0403	0.385049	0.309439	121.824	0.346673	0.189184
35-40%	32.2846	0.4266	0.33192	99.368	0.381703	0.210539
40-45%	26.4167	0.469567	0.352952	79.9718	0.416077	0.233072
45-50%	21.3906	0.513928	0.36881	63.2823	0.450526	0.257258
50-55%	17.0871	0.561095	0.378653	49.1096	0.485288	0.28369
55-60%	13.4633	0.609601	0.381766	37.282	0.521951	0.31025
60-65%	10.4524	0.653875	0.377414	27.5652	0.562577	0.335464
65-70%	7.98109	0.688282	0.371631	19.7557	0.609362	0.354116
70-75%	6.00038	0.70822	0.373838	13.7591	0.658555	0.362815
75-80%	4.46403	0.717944	0.391913	9.26462	0.698532	0.359999
80-85%	3.36099	0.721535	0.425829	5.986	0.716055	0.365
85-90%	2.61854	0.723772	0.47175	3.72586	0.716667	0.407448
90-95%	2.22168	0.727006	0.518758	2.49408	0.715396	0.477809
95-100%	2.07272	0.732491	0.546403	2.0577	0.727604	0.560143

Table 7.9: The Glauber values used in sections 5.3.2 and 5.3.4.

Bibliography

[1] David Griffiths. *Introduction to Elementary Particles*. 2nd. Wiley-VCH, 2004.

[2] *Eightfold Way (physics)*. URL: https://en.wikipedia.org/wiki/Eightfold_Way_(physics).

[3] Peter Braun-Munzinger and Johanna Stachel. "The Quest for the Quark-Gluon Plasma". In: *Nature* 448 (7151 Aug. 2007), pp. 302–309. DOI: 10.1038/nature06080. URL: http://dx.doi.org/10.1038/nature06080.

[4] Kenji Fukushima. "Quest for the QCD phase diagram in extreme environments". English. In: *Hyperfine Interactions* 215.1-3 (2013), pp. 45–51. ISSN: 0304-3843. DOI: 10.1007/s10751-013-0779-8. URL: http://dx.doi.org/10.1007/s10751-013-0779-8.

[5] Shinji Ejiri. "Canonical partition function and finite density phase transition in lattice QCD". In: *Phys. Rev. D* 78 (7 Oct. 2008), p. 074507. DOI: 10.1103/PhysRevD.78.074507. URL: http://link.aps.org/doi/10.1103/PhysRevD.78.074507.

[6] S. S. Adler et al. "Centrality Dependence of Direct Photon Production in $\sqrt{S_{NN}} = 200$ GeV Au + Au Collisions". In: *Phys. Rev. Lett.* 94 (23 June 2005), p. 232301. DOI: 10.1103/PhysRevLett.94.232301. URL: http://link.aps.org/doi/10.1103/PhysRevLett.94.232301.

[7] A. Adare et al. "Suppression of away-side jet fragments with respect to the reaction plane in Au + Au collisions at $\sqrt{s_{NN}} = 200$ GeV". In: *Phys. Rev. C* 84 (2 Aug. 2011), p. 024904. DOI: 10.1103/PhysRevC.84.024904. URL: http://link.aps.org/doi/10.1103/PhysRevC.84.024904.

[8] B. Alver et al. "System Size, Energy, and Centrality Dependence of Pseudorapidity Distributions of Charged Particles in Relativistic Heavy-Ion Collisions". In: *Phys. Rev. Lett.* 102 (14 Apr. 2009), p. 142301. DOI: 10.1103/PhysRevLett.102.142301. URL: http://link.aps.org/doi/10.1103/PhysRevLett.102.142301.

[9] B. B. Back et al. "Significance of the Fragmentation Region in Ultrarelativistic Heavy-Ion Collisions". In: *Phys. Rev. Lett.* 91 (5 Aug. 2003), p. 052303. DOI: 10.1103/PhysRevLett.91.052303. URL: http://link.aps.org/doi/10.1103/PhysRevLett.91.052303.

[10] A. M. Poskanzer and S. A. Voloshin. "Methods for analyzing anisotropic flow in relativistic nuclear collisions". In: *Phys. Rev. C* 58 (3 Sept. 1998), pp. 1671–1678. DOI: 10.1103/PhysRevC.58.1671. URL: http://link.aps.org/doi/10.1103/PhysRevC.58.1671.

[11] A. Adare et al. "Scaling Properties of Azimuthal Anisotropy in Au+Au and Cu+Cu Collisions at $\sqrt{s_{NN}} = 200$ GeV". In: *Phys. Rev. Lett.* 98 (16 Apr. 2007), p. 162301. DOI: 10.1103/PhysRevLett.98.162301. URL: http://link.aps.org/doi/10.1103/PhysRevLett.98.162301.

[12] S. Manly. "System size, energy and pseudorapidity dependence of directed and elliptic flow at RHIC". In: *Nucl. Phys.* A774 (2006), pp. 523–526. DOI: 10.1016/j.nuclphysa.2006.06.079. arXiv: nucl-ex/0510031 [nucl-ex].

[13] L. Adamczyk et al. "Third harmonic flow of charged particles in Au + Au collisions at $\sqrt{s_{NN}} = 200$ GeV". In: *Phys. Rev. C* 88 (1 July 2013), p. 014904. DOI: 10.1103/PhysRevC.88.014904. URL: http://link.aps.org/doi/10.1103/PhysRevC.88.014904.

[14] Burak Han Alver et al. "Triangular flow in hydrodynamics and transport theory". In: *Phys. Rev. C* 82 (3 Sept. 2010), p. 034913. DOI: 10.1103/PhysRevC.82.034913. URL: http://link.aps.org/doi/10.1103/PhysRevC.82.034913.

[15] J. J. Aubert et al. "Experimental Observation of a Heavy Particle J". In: *Phys. Rev. Lett.* 33 (23 Dec. 1974), pp. 1404–1406. DOI: 10.1103/PhysRevLett.33.1404. URL: http://link.aps.org/doi/10.1103/PhysRevLett.33.1404.

[16] J. Beringer et al. "Review of Particle Physics". In: *Phys. Rev. D* 86 (1 July 2012), p. 010001. DOI: 10.1103/PhysRevD.86.010001. URL: http://link.aps.org/doi/10.1103/PhysRevD.86.010001.

[17] K. Adcox et al. "Construction and performance of the PHENIX pad chambers". In: *Nucl.Instrum.Meth.* A497 (2003), pp. 263–293. DOI: 10.1016/S0168-9002(02)01791-6.

[18] Yuji Tsuchimoto. *Introduction to PHENIX Beam Beam Counter (BBC)*. Tech. rep. Hiroshima University, 2004. URL: https://www.phenix.bnl.gov/WWW/run/04/focus/talks/bbc/bbc_talk.ppt.

[19] E. Richardson et al. "A Reaction Plane Detector for PHENIX at RHIC". In: *Nucl.Instrum.Meth.* A636 (2011), pp. 99–107. DOI: 10.1016/j.nima.2011.01.034. arXiv: 1012.0873 [nucl-ex].

[20] Adler et al. "The RHIC zero degree calorimeter". In: *Nucl.Instrum.Meth.* A470 (2001), pp. 488–499. DOI: 10.1016/S0168-9002(01)00627-1. arXiv: nucl-ex/0008005 [nucl-ex].

[21] J.T. Mitchell et al. "Event reconstruction in the PHENIX central arm spectrometers". In: *Nucl.Instrum.Meth.* A482 (2002), pp. 491–512. DOI: 10.1016/S0168-9002(01)01512-1. arXiv: nucl-ex/0201013 [nucl-ex].

[22] K. Adcox et al. "PHENIX central arm tracking detectors". In: *Nucl.Instrum.Meth.* A499 (2003), pp. 489–507. DOI: 10.1016/S0168-9002(02)01952-6.

[23] Hans-Åke Gustafsson. *The Pad Chambers (PC)*. Tech. rep. Lund University, 2002. URL: http://www.phenix.bnl.gov/phenix/WWW/intro/detectors/focus/focus_bbc.pdf.

[24] Y. Akiba et al. "Ring imaging Cherenkov detector of PHENIX experiment at RHIC". In: *Nucl.Instrum.Meth.* A433 (1999), pp. 143–148. DOI: 10.1016/S0168-9002(99)00319-8.

[25] Péter Tarján. *The PHENIX Electromagentic Calorimeter*. Tech. rep. University of Debrecen, Hungary, 2004. URL: https://www.phenix.bnl.gov/WWW/run/04/focus/talks/emc/emc_talk.ppt.

[26] K. Adcox et al. "PHENIX detector overview". In: *Nucl.Instrum.Meth.* A499 (2003), pp. 469–479. DOI: 10.1016/S0168-9002(02)01950-2.

[27] Ed Desmond. *DAQ Operator Training*. Tech. rep. PHENIX Collaboration, 2009. URL: https://www.phenix.bnl.gov/WWW/run/15/subsys_tutorials/daq/Run9RDAQOperatorTraining.ppt.

[28] David Winter. *DAQ Introduction*. Tech. rep. Columbia University, 2004. URL: https://www.phenix.bnl.gov/WWW/run/15/subsys_tutorials/daq/DAQ-Introduction-Run4.pdf.

[29] Jiangyong Jia. "High-p_T Charged Hadron Suppression in Au+Au Collisions at $\sqrt{s_{NN}} = 200$ GeV". PhD thesis. State University of New York at Stony Brook, Aug. 2003.

[30] B. Alver et al. "The PHOBOS Glauber Monte Carlo". In: (2008). arXiv: 0805.4411 [nucl-ex].

[31] H. De Vries, C.W. De Jager, and C. De Vries. "Nuclear charge and magnetization density distribution parameters from elastic electron scattering". In: *Atom.Data Nucl.Data Tabl.* 36 (1987), pp. 495–536. DOI: 10.1016/0092-640X(87)90013-1.

[32] Walter Loveland, David J. Morrisey, and Glenn T. Seaborg. *Modern Nuclear Chemistry*. Wiley, 2006. ISBN: 9780471115328.

[33] B. Alver and G. Roland. "Collision-geometry fluctuations and triangular flow in heavy-ion collisions". In: *Phys. Rev. C* 81 (5 May 2010), p. 054905. DOI: 10.1103/PhysRevC.81.054905. URL: http://link.aps.org/doi/10.1103/PhysRevC.81.054905.

[34] Axel Drees et al. *Centrality determination and p_T centrality dependence in d-Au collisions*. Analysis Note 210. State University of New York, Stony Brook, 2003.

[35] T. Abbott et al. "Multiplicity distributions from central collisions of ^{16}O+Cu at 14.6 A GeV c and intermittency". In: *Phys. Rev. C* 52 (5 Nov. 1995), pp. 2663–2678. DOI: 10.1103/PhysRevC.52.2663. URL: http://link.aps.org/doi/10.1103/PhysRevC.52.2663.

[36] Sasha Milov. *Centrality determination using BBC in Au+Au and Cu+Cu collisions at $\sqrt{s_{NN}} = 200$ GeV*. Analysis Note 461. State University of New York, Stony Brook, 2005.

[37] R.S. Bhalerao, N. Borghini, and J.Y. Ollitrault. "Analysis of anisotropic flow with Lee-Yang zeroes". In: *Nucl.Phys.* A727 (2003), pp. 373–426. DOI: 10.1016/j.nuclphysa.2003.08.007. arXiv: nucl-th/0310016 [nucl-th].

[38] Paul Stankus. *Mathematical Framework for Interpreting Pair Angular Correlations in a Two-Source Model*. Tech. rep. Oak Ridge National Laboratory, 2003. URL: https://www.phenix.bnl.gov/phenix/WWW/publish/stankus/tech_notes/corr_framework_I.

[39] A. Adare et al. "Dihadron azimuthal correlations in Au+Au collisions at $\sqrt{s_{NN}} = 200$ GeV". In: *Phys. Rev. C* 78 (1 July 2008), p. 014901. DOI: 10.1103/PhysRevC.78.014901.

[40] A. Adare et al. "Systematic Study of Azimuthal Anisotropy in Cu+Cu and Au+Au Collisions at $\sqrt{s_{NN}} = 62.4$ and 200 GeV". In: (2014). arXiv: 1412.1043 [nucl-ex].

[41] A. Adare et al. "Measurements of Higher Order Flow Harmonics in Au+Au Collisions at $\sqrt{s_{NN}} = 200$ GeV". In: *Phys. Rev. Lett.* 107 (25 Dec. 2011), p. 252301. DOI: 10.1103/PhysRevLett.107.252301. URL: http://link.aps.org/doi/10.1103/PhysRevLett.107.252301.

[42] A. Adare et al. "Measurement of the higher-order anisotropic flow coefficients for identified hadrons in Au+Au collisions at $\sqrt{s_{NN}} = 200$ GeV". In: (2014). arXiv: 1412.1038 [nucl-ex].

[43] A. Adare et al. "Systematic study of azimuthal anisotropy in Cu + Cu and Au + Au collisions at $\sqrt{s_{NN}} = 62.4$ and 200 GeV". In: *Phys. Rev. C* 92 (3 Sept. 2015), p. 034913. DOI: 10.1103/PhysRevC.92.034913. URL: http://link.aps.org/doi/10.1103/PhysRevC.92.034913.

[44] B. I. Abelev et al. "Charged and strange hadron elliptic flow in Cu+Cu collisions at $\sqrt{s_{NN}} = 62.4$ and 200 GeV". In: *Phys. Rev. C* 81 (4 Apr. 2010), p. 044902. DOI: 10.1103/PhysRevC.81.044902. URL: http://link.aps.org/doi/10.1103/PhysRevC.81.044902.

[45] B. Alver et al. "System Size, Energy, Pseudorapidity, and Centrality Dependence of Elliptic Flow". In: *Phys. Rev. Lett.* 98 (24 June 2007), p. 242302. DOI: 10.1103/PhysRevLett.98.242302. URL: http://link.aps.org/doi/10.1103/PhysRevLett.98.242302.

[46] S. Afanasiev et al. "Charged Kaon Interferometric Probes of Space-Time Evolution in Au+Au Collisions at $\sqrt{s_{\mathrm{NN}}} = 200$ GeV". In: *Phys. Rev. Lett.* 103 (14 Sept. 2009), p. 142301. DOI: 10.1103/PhysRevLett.103.142301. URL: http://link.aps.org/doi/10.1103/PhysRevLett.103.142301.